Title
Efficient Modeling of Plasma Wake Field Acceleration Experiments Using Particle-In-Cell Methods

Author
An, Weiming

Publication Date
2013

Peer reviewed|Thesis/dissertation

University of California
Los Angeles

Efficient Modeling of Plasma Wake Field Acceleration Experiments Using Particle-In-Cell Methods

A dissertation submitted in partial satisfaction
of the requirements for the degree
Doctor of Philosophy in Electrical Engineering

by

Weiming An

2013

Abstract of the Dissertation

Efficient Modeling of Plasma Wake Field Acceleration Experiments Using Particle-In-Cell Methods

by

Weiming An

Doctor of Philosophy in Electrical Engineering

University of California, Los Angeles, 2013

Professor Warren B. Mori, Chair

There is no clear path for building a particle accelerator at the energy frontier beyond the Large Hadron Collider (LHC). One option that is receiving attention is to use plasma wave wakefields driven by intense particle beams. Recent experiments conducted at the Stanford Linear Accelerator Center (SLAC) show that accelerating gradients in such wakefields in excess of 50 GeV/m can be sustained over meter scales. Based on this, a linear collider concept of staging one-meter long plasma cells together has been proposed. A facility at SLAC has been built to study the physics in one stage. In this dissertation we describe improvements and enhancements to a highly efficient simulation model for simulating current experiments at SLAC as well as parameters beyond the reach of current experiments. The model is the quasi-static particle-in-cell (PIC) code QuickPIC. A modified set of quasi-static field equations were developed, which reduced the number of predictor corrector iteration loops and an improved source deposit scheme was developed to reduce the parallel communication. These improvements led to a factor of 5 to 8 (depending on the simulation parameters) speedup compared with the previous set of field equations and deposition scheme. Several new modules

were also added to QuickPIC, including the multiple field ionization and improved beam and plasma particle diagnostics. We also used QuickPIC to study the optimum plasma density for maximizing the acceleration field for fixed electron beam parameters. QuickPIC simulations were also used to study and design two-bunch PWFA experiments at SLAC including methods for mitigating the ionization-induced beam head erosion. The mitigation methods can enhance the energy gain in two-bunch PWFA experiments at SLAC by a factor of 10 for the same beam parameters. For beam parameters beyond SLAC but perhaps necessary for a future collider, QuickPIC was used to study how the ultra high electric fields of a tightly focused second electron bunch could lead to ion motion, which disrupts the focusing fields on the second bunch. The resulting nonlinearity in the transverse focusing force of the plasma wake will lead to emittance growth. We used QuickPIC to carry out the first fully self-consistent high resolution simulation on the effects of ion motion for PWFA linear collider problems. Preliminary results showed that the plasma-ion-motion-induced emittance growth was limited to less than a factor of 2. In addition to the electron beam driven PWFA, we also study how a short proton beam can excite a large plasma wake. Such short proton beams are currently not experimentally available. We therefore also study how long proton beams such as those at Fermi National Laboratory and CERN may drive a large plasma wake through a self-modulation instability. A linear theory for the self-modulation instability is presented under the wide beam limit. QuickPIC simulations show that the self-modulation of a long proton beam in a plasma may lead to the micro-bunching of the beam and excite a large plasma wake.

The dissertation of Weiming An is approved.

George J. Morales

Oscar M. Stafsudd

Chandrashekhar J. Joshi

Warren B. Mori, Committee Chair

University of California, Los Angeles

2013

To my parents and my lovely wife.

Table of Contents

List of Figures

List of Tables

Acknowledgments

First, I would like to thank my advisor professor Warren Mori who gave me the chance to step in the research area of this dissertation. Without his continuous support and patient teaching, it would not be possible for me to conduct the work in this dissertation. I am also grateful to professor Chan Joshi for providing me valuable help and guidance in my research. I would like to thank Dr. Viktor Decyk, professor Thomas Antonsen, professor Wei Lu, Dr. Chengkun Huang and Dr. Miaomiao Zhou for their involvement in my work. I am also thankful to professor Oscar Stafsudd and professor George Morales for reading my dissertation.

I am honored to work with Dr. Frank Tsung, Dr. Michail Tzoufras, Dr. Ben Winjum, Dr. Jay Fahlen, Joshua May, Asher Davidson, Ian Ellis, Peicheng Yu, Adam Tableman in the plasma simulation group at UCLA. I feel lucky to meet all of these wonderful people and to collaborate with them.

Vita

1982	Born, Tianjin, P. R. China.
2000–2004	B. S. Engineering Physics, Tsinghua University, Beijing, P. R. China.
2004–2007	M. S. Nuclear Science and Engineering, Tsinghua University, Beijing, P. R. China.
2007–present	Ph. D. candidate, Department of Electrical Engineering, University of California, Los Angeles, California, U. S. A.

Publications

W. Lu, W. An, C. Huang, C. Joshi, and W. B. Mori, "High Transformer Ratio Plasma Wakeeld Acceleration in the Blowout Regime", in preparation.

W. An, M. Zhou, N. Vafaei-Na jafabadi, K. A. Marsh, C. E. Clayton, C. Joshi, W. B. Mori, W. Lu, E. Adli, S. Corde, M. Litos, S. Li, S. Gessner, J. Frederico, M. J. Hogan, D. Walz, J. England, J. P. Delahaye, and P. Muggli, "Strategies for mitigating the ionization-induced beam head erosion problem in an electron-beam-driven plasma wake field accelerator", Phys. Rev. ST Accel. Beams. 16, 101301 (2013).

W. An, V. K. Decyk, W. B. Mori and T. M. Antonsen Jr., "An improved iteration loop for the three dimensional quasi-static particle-in-cell algorithm: QuickPIC", J. Comp. Phys. 250, 165 (2013).

W. Lu, W. An, M. Zhou, C. Joshi, C. Huang and W. B. Mori, "The optimum plasma density for plasma wakefield excitation in the blowout regime", New Journal of Physics 12, 085002 (2010).

M. J. Hogan, T. O. Raubenheimer, A. Seryi, P. Muggli, T. Katsouleas, C. Huang, W. Lu, W. An, K. A. Marsh, W. B. Mori, C. E. Clayton and C. Joshi, "Plasma wakefield acceleration experiments at FACET", New Journal of Physics 12, 055030 (2010).

CHAPTER 1

Introduction

1.1 The LHC and ILC

The development of particle accelerators can be traced back to the year of 1911 when Rutherford discovered his model of the atom in the famous gold foil experiment. Subsequently, many different kinds of accelerators have been built mainly for studying and discovery new particles, although significant applications for the accelerator such as radiation sources and medical treatment have also been discovered. On September 10th, 2008, almost 100 years after Rutherford's experiments, the large hadron collider (LHC) built by the European organization for nuclear research (CERN) began to operate with proton beams circulating in its main ring [1]. However, the LHC was shut down 9 days later due to a faulty electrical connection and was brought back to full operation 14 months later on November 20th, 2009. The LHC is designed for colliding two opposing particle beams of either protons at an energy up to 7 TeV, or lead nuclei at an energy of 574 TeV. The maximum collision energy per nucleon-pair reaches around 14 TeV, which is seven times larger than its predecessor at Fermi National Laboratory (FNAL). The main ring of LHC lies in a 27 km circular tunnel, which is as deep as 175 m beneath the border of France and Switzerland close to the Switzerland city of Geneva. Building this gigantic machine involved 10,000 scientists and engineers from over 100 countries, as well as hundreds of universities and laboratories. It is the largest and most expensive scientific instrument ever built, with a construction budget alone of 7.5 billion euros.

Even though the LHC is in its early stages of use and has led to new discoveries, the community has already begun to plan for the future and think about the next high energy accelerator. The international linear collider (ILC) is one concept for a future high energy accelerator [2]. The ILC would have a collision energy of 500 GeV initially, with the possibility for a later upgrade to 1000 GeV (1 TeV). It would collide electrons with positrons that are accelerated through a 30 km (or even longer) linear accelerator, which is more than 10 times as long as the longest existing linear accelerator (which had a maximum energy of 50 GeV) at Stanford Linear Accelerator Center (SLAC). Although the ILC has a lower collision energy than the LHC, it is expected to make more precision measurements as the collision between leptons such as electrons and positrons are much easier to analyze and no energy is needed to overcome the strong forces that keep quarks together in a proton. The ILC is designed to discover physics beyond the current standard model. However, the estimated total construction cost for this machine is over 20 billion dollars, which makes it unlikely to be built in the foreseeable future.

The primary reason for the high cost of building high energy accelerators such as the LHC and ILC is that the size of the accelerator is so large. As a circular accelerator, the main ring of the LHC is 27 km in circumstance. Such a long circumference is mainly needed for reducing the energy loss of the particle from synchrotron radiation. The power radiated is proportional to the energy of the particle divided by its rest mass to the 4th power and inversely proportional to the circumference. Specifically during each turn, the particle losses

$$\Delta E[\text{TeV}] \approx 5.5 \frac{(E[100\text{GeV}]/(m_b/m_e))^4}{C[\text{km}]},$$

where E is the particle energy, m_b and m_e are the rest masses for the particle and the electron and C is the circumference of circular accelerator. That is also why the LHC is accelerating protons or lead nuclei instead of electrons and positrons. Although the synchrotron radiation losses can be made relatively small when hadrons are used, the bending magnets used to keep particles moving in

a circle need larger magnetic fields as the particle energy goes up. The power needed to generate these bending fields can become large and this also requires a large circumference for the accelerator. Considering the cost of the LHC, it is very unlikely that a circular collider will be built at higher energy. Even if new accelerator technology is developed, the issues related to synchrotron radiation for Leptons and magnetic field strength for bending Hadrons means that the size of a future circular machine will be prohibitive.

However, the cost of a linear accelerator can be reduced if new accelerator technology is developed. In a linear accelerator (also called a linac) such as the proposed ILC [2], electrons and positrons are accelerated along a straight line in a single pass. This linear geometry implies that the maximum energy gain of the accelerator is equal to the product of the acceleration gradient (which is the energy gain per unit length) and the accelerator length. If the acceleration gradient is 20 MeV/m, the ILC would need two 25 km accelerators (50 km in total) to obtain 500 GeV electron and positron beams. An efficient way to reduce the length as well as the cost of a linac is to increase the acceleration gradient. In the conventional accelerator, the accelerating electric field is usually built up within a cavity having conductive boundaries. The electric breakdown and the heat congregation (which affects the superconductive cavity) will limit the acceleration gradient to less than 100 MeV/m. Thus, to overcome this limit one needs to replace the current radio-frequency (RF) conducting cavities. One way is using a plasma as the acceleration medium. Such an accelerator is called a plasma-based accelerator. Because the fields are formed by the freely moving plasma electrons and ions, the electric breakdown problem does not exist in the plasma. A plasma-based accelerator turns out to be an attractive candidate for a future linear accelerator.

1.2 The development of plasma-based accelerator

In 1979, T. Tajima and J. Dawson [3] proposed a new method for accelerating electrons by exciting a plasma wave using a high power and short pulse length laser. This plasma wave is actually a wake field excited by the pump laser pulse (i.e. the laser drive beam). It is analogous to the water wave wake propagating right after a boat moving faster than the "group" velocity of the wake. This idea was originally called a wake plasmon accelerator, but it is now referred to the laser wake field accelerator (LWFA). In the LWFA, the phase velocity of the plasma wave will be equal to the laser drive beam's group velocity, which can be very close to the speed of light. Its group velocity is essentially zero. Therefore the laser wake field is suitable for accelerating charged particles to high energy. In 1985, it was proposed to use an electron beam to drive the plasma wake field instead of the laser [4]. A second charged particle beam (the trailing beam), which is following the drive beam and sitting in a proper phase inside the plasma wave wake, can be accelerated to a high energy before the drive beam stops due to its energy loss in creating the wake. The prevailing name for this scheme is the plasma wake field accelerator (PWFA). In fact the laser scheme was called the LWFA after the term wake field accelerator was used to describe the particle beam driver scheme.

As a charged particle acceleration method, the most important property of LWFA and PWFA is that the plasma wave can sustain a much higher accelerating gradient than a conventional accelerator. We can estimate the amplitude of this plasma wave by using Gauss's law. For simplicity, we consider the one dimensional Gauss's law and assume the ions in the plasma are fixed,

$$\frac{\partial}{\partial x} E_w = -4\pi e \tilde{n}_e,$$

where $\tilde{n}_e = n_e - n_{e0}$ is the density perturbation of the plasma electrons. We assume the plasma wave has a phase velocity equal to c (this is reasonable because in both PWFA and LWFA the plasma wake has a phase velocity equal to the drive

beam's velocity that is very close to c) and the plasma wave oscillates at the plasma frequency $\omega_p = \sqrt{\frac{4\pi e^2 n_p}{m_e}}$ (where n_p is the initial plasma density). If $|\partial/\partial x| \to |k| = \omega_p/c$, then we have the equation,

$$|E_w| = \frac{m_e \omega_p c}{e} \cdot \frac{\tilde{n}_e}{n_p} \approx 100[\mathrm{GV/m}] \times \sqrt{\frac{n_p}{10^{18}\,[\mathrm{cm}^{-3}]}} \cdot \frac{\tilde{n}_e}{n_p}$$

This means in a plasma with a background density of $10^{18}\,\mathrm{cm}^{-3}$, the amplitude of the plasma wave can reach as high as 100 GV/m when the harmonic perturbation of the plasma electron density is equal to the initial plasma density. That is 1000 times larger than the breakdown limit of a conventional accelerator's accelerating gradient. For large density perturbations, the wake is nonlinear but this simple estimate is still a useful guide.

Driven by the potential for producing high acceleration gradients, research in plasma-based accelerator has been actively conducted for over 30 years. In the early 1990s, an acceleration gradient as high as 100 GeV/m in a laser driven plasma wake field accelerator was reported experimentally [5]. However, this experiment was not carried out in the LWFA regime [3], which requires an ultra short (comparable to the plasma skin depth) and intense laser drive beam. This is because all intense lasers existing at that time were generally not short enough. Therefore, many alternative methods were explored to drive a large amplitude plasma wake field (often in a high density $\sim 10^{18}\,\mathrm{cm}^{-3}$ plasma) using long pulse laser drive beams. One is the plasma beat wave accelerator (PBWA) [6] that uses two long laser pulses that have a frequency difference close to the plasma frequency to resonantly drive a plasma wave. Another is the self-modulated laser wake field accelerator (SM-LWFA) [5] that relies on the long laser pulse to self-modulate through an instability into a series of short laser pulses much like in the PBWA and hence to drive a large wake field in the plasma. The experiment that reached the 100 GeV/m acceleration gradient operated in the SM-LWFA regime. Although the acceleration gradient was very high, the acceleration length was

rather small ($\sim 1\,\mathrm{mm}$) and the energy gain of the accelerated electrons was only tens of MeV in those early SM-LWFA experiments [5, 7]. A similar energy gain of electrons using the PWFA scheme was also reported in the early 1990s [8]. But the acceleration gradient in the experiment is only 30 MeV/m. The relatively low gradient is obtained because the drive beam used in the experiment had a low current.

With the further development of the chirped pulse amplification (CPA) technology for lasers [9, 10, 11], high intensity short pulse lasers for the LWFA experiments became available in the early part of 21st century. In 2004, three different groups published their LWFA experiments results [12, 13, 14]. All of them detected accelerated and self-trapped electron beams coming out of the plasma with energies around 100 MeV as well as with relatively narrow energy spreads ($2 \sim 24\%$), a small divergence angle, a short pulse length ($\sim 10\,\mathrm{fs}$) and a reasonable amount of charge ($\sim 10^9$ electrons). In addition, these experiments all had compact setups (which were referred as "table-top" systems in many publications). These LWFA results led to active research efforts on using plasma-based accelerator not only for a high energy collider but also for driving a compact free electron laser (FEL) [15].

However, the lasers used in the experiments of [12, 13, 14] were still not ideal. They were cigar shaped not spherical. To obtain better results, research has continued on building stable laser systems that operate at higher energy and at higher repetition rate. Such lasers will reliably produce high brightness monoenergetic electron beams. In addition, many theoretical and experimental work has contributed to a better understanding of the plasma wake formation, the self-injection of the plasma electrons and the guiding of the laser. For example, a theoretical model [16, 17] was developed for analyzing a nonlinear plasma wake driven by an intense laser pulse or electron beam (which was called the blow-out regime). Note that most of the current schemes for accelerating electrons in a

plasma wake belong to this regime. A new plasma electron injection scheme that relies on field-ionization of electrons inside the wake [18, 19, 20] was proposed and tested through experiments. This ionization-induced injection is typically easier to control than the self-injection of background plasma electrons in very nonlinear wakes. Simulations have played an invaluable role in the progress.

While the recent LWFA results in the 2000s were impressive, recent PWFA research has also produced transformative results. Beginning in the late 1990s, a series of experiments using the SLAC electron/positron beams were performed [21, 22, 23, 24, 25, 26, 27]. These experiments motivated significant theoretical developments as well. The research culminated in 2007 with the observation of more than 40 GeV energy gain on the tail of an electron beam (with an initial energy of 42 GeV) after it passed through ONLY 85 cm of Li plasma [28]. This demonstrated for the first time an accelerating gradient exceeding 50 GeV/m sustained over almost one meter in a plasma. This distance was nearly the pump depletion length of the drive beam. And the energy gain observed in the experiment remains the highest from any plasma-based accelerator concept. The experiments were carried out at the final focus test beam (FFTB) facility at SLAC, which was able to deliver a 42 GeV beam containing 1.8×10^{10} electrons (or positrons) and with an r.m.s. pulse length as short as $15\,\mu$m (120 J/50 fs pulses or 2.4 PW (10^{15} W)). The electron beam at SLAC is the most intense in the world, and is essential to the success of a PWFA experiments.

The success of the PWFA experiments at FFTB were widely noticed throughout the world and caused accelerator physicist to take plasma-based accelerators seriously. Several new facilities have been proposed and built to explore the LWFA and PWFA. In the area of LWFA, the Berkeley laboratory laser accelerator (BELLA) project at the Lawrence Berkeley national laboratory (LBNL) aims at accelerating electrons as well as positrons to an energy of 10 GeV in one meter using 30 J/30 fs, i.e., PW pulses [29]. The BELLA laser will deliver pulses at 2

Hz repetition rates. The extreme light infrastructure (ELI) project in Europe [30] also includes research plans in LWFA. In the area of PWFA, a new facility for advanced accelerator experimental tests (FACET) [31] was constructed at SLAC mainly for demonstrating high quality accelerated electron (or positron) beam generation through the PWFA. This facility includes 23 GeV, 3.2 nC, 30 μm (70 J/100 fs) electron and positron bunches.

Both CERN and the Fermi national accelerator laboratory (FNAL) are interested in accelerating electrons using high energy and long pulse-length proton beams [32, 33], which generate wakes through the self-modulation of the long drive beam to excite a large plasma wave in the plasma (a similar idea to the SM-LWFA in the early 1990s). These experiments are motivated by the observation in simulations that ultra-short (highly compressed) proton bunches can create nearly ideal plasma wakes for accelerating electrons [34]. A compressed 7 TeV (LHC) proton beam could generate ~ 1 TeV electrons in a single stage.

These facilities (current and proposed) show the intense interest in the possibility of building a compact high energy accelerator in the future. Although there are several unsolved issues including how to efficiently load positron beams into a plasma wake and that tightly focused trailing beams can cause the ions to move leading to emittance growth, these new facilities illustrate that the accelerator community sees possible paths towards colliders based on plasma-based accelerators. In addition, as noted earlier, plasma-based accelerator may be the basis for a compact XFEL in the future.

1.3 The particle-in-cell simulation

The tremendous progress in experiments in the plasma-based accelerator in the past 20 years would not have occurred without tremendous advances in simulation and theory. High fidelity simulations are now an indispensable part of any research

effort in plasma-based acceleration. Even the original papers on LWFA and PWFA relied heavily on simulation. Numerical simulation is now one of the three pillars of the scientific method alongside theory and experiment. Not only can it provide complementary evidence for experimental observations or theoretical predictions, it can also play a leading role in the discovery of new physics and hence guide both theoretical and experimental research. This has been especially true for plasma-based accelerator research.

There are different methods for simulating the plasma. One of them is the particle-in-cell (PIC) method [35, 36]. In the PIC method, the motion of a large number of plasma electrons and ions are tracked while they are self-consistantly interacting with their self-generated electromagnetic fields (and external fields). The electromagnetic fields and the charge and current densities are defined on the discretized spatial grid points while the particles are defined with continuous positions and momenta. At each time step of the PIC code, the electromagnetic fields are first interpolated on the particle's position from the grid points. Then, according to the interpolated electromagnetic fields, each particle is advanced (pushed) to the next time step with a new velocity and position by a finite difference integration of the equations of motion. Next, the charge and current densities from each particle are deposited on the grid points according to the particle's new position and velocity. Lastly, the electromagnetic fields at the next time step are obtained by a finite difference or Fast Fourier transform (FFT) based integration of Maxwell's equation using the new charge and current densities. This is the end of the loop for one time step. The loop is repeated until the desired number of time steps is reached. The concept of a finite size macro particle (particle cloud) with the same charge to mass ratio as a real particle is used when depositing the charge and current density on the grid point, thus allowing the PIC code to use a small number of macro particles to represent the real plasma when quantitative details of thermal fluctuation and Coulomb collisions are not needed.

The PIC code is suitable for simulating a non-equilibrium and very nonlinear problem, especially when the kinetic effects are important and the fluid models cannot be used. Therefore, the PIC code is the best choice for simulating the laser-plasma or beam-plasma interactions in plasma-based accelerators. Although the use of macro particles dramatically reduces the requirement of particle number in the PIC code, the full scale multidimensional simulation of the plasma-based accelerator is still a massive task. The development of parallel computing and its application in the PIC algorithm [37, 38] meet this need. A large amount of research has contributed to enable parallel PIC codes to simulate very large problems in an efficient way. For example, the PIC code OSIRIS [39] has been scaled to more than 1 million cores without losing much efficiency.

OSIRIS and other so-called "full" PIC codes are fully explicit and solve the full set of Maxwell equations using small time steps that resolve the highest frequencies, i.e., waves at the shortest wave lengths that are resolved. These codes make very little approximation. On today's largest computers, they can simulate a variety of problems including plasma-based acceleration. However, in terms of CPU-hours, it is still very expensive to use a full PIC code for multidimensional plasma-based accelerator simulations. Alternative PIC-based methods have therefore been developed to complement the use of full PIC codes. One method is to simulate the problem in a Lorentz-boosted frame instead of the lab frame [40, 41]. This method is based on the fact that either a short laser beam or the particle beam moves almost at the speed of light through long regions of plasma in a plasma-based accelerator. With Lorentz transformations the laser or the particle beam may have a comparable spatial scale to the plasma and hence in this frame the number of cells needed to resolve the laser or particle beam is the same as before. The pulse (and wave length of the laser) are Lorentz expanded. So that each cell and time step are also larger. This combined with the shorter plasma leads to large computational savings. Another method is applying the quasi-static

approximation in the PIC algorithm [42, 43]. It calculates the plasma response to a non-evolving laser or particle beam (which is moving at the speed of light) under the quasi-static approximation. Then the plasma wake fields are used for updating the laser or particle beam. The quasi-static approximation is based on the fact that the laser or particle beam evolves on a much slower time scale than the plasma particles. With the quasi-static approximation, the plasma response is only updated when the laser or particle beam is updated, which could make such a code several orders of magnitude faster than the full PIC code.

QuickPIC [43] is a three dimensional (3D) PIC code, which applies the quasi-static approximation. It is developed based on a PIC framework called UPIC [38] and is able to simulate both laser driven (using the pondermotive guiding center approach [44]) and high energy particle beam driven plasma-based accelerator. In QuickPIC, the plasma response is calculated for a static (fixed) laser/particle beam. Then the nonlinear index of refraction is used to advance the laser and the wake fields are used to advance the particle beam. The code uses the coordinates (x, y, $\xi = ct - z$, $s = z$) instead of the coordinates (x, y, z, t). The laser/particle beam evolves on a slow time scale of s. At each step of s, the plasma response is advanced with a fast time scale of ξ and is not dependent on the variable s. The Figure 1.1 (taken from reference [43]) shows different time scales for the laser/particle drive beam and the plasma evolution in QuickPIC.

Figure 1.2 shows the flow chart of the basic algorithm in QuickPIC, which has a 2D routine embedded in a 3D routine. The 3D routine is used to calculate the evolution of the laser/particle drive beam in respect of s. In each 3D loop, the 2D routine is used to calculate the plasma response to the static laser/particle beam driver in respect of ξ. Both the 3D routine and the 2D routine are parallelized. The use of a pipeline method [45] allows QuickPIC to scale up to 100000 processors.

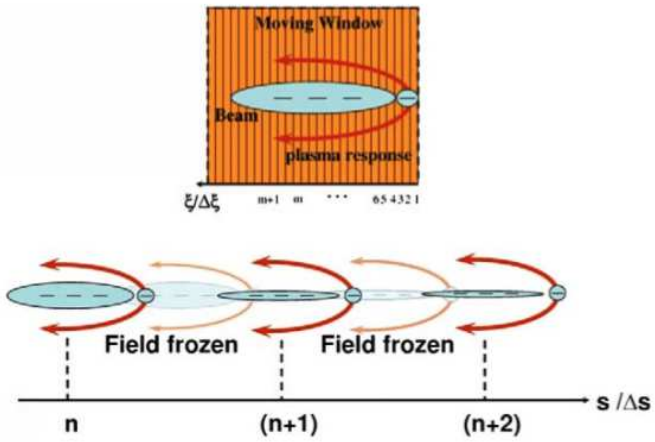

Figure 1.1: The two variables s and ξ for the different time scales for laser/particle drive beam and plasma evolution. Δs is the time step in s while $\Delta\xi$ is the time step in ξ (taken from reference [43]).

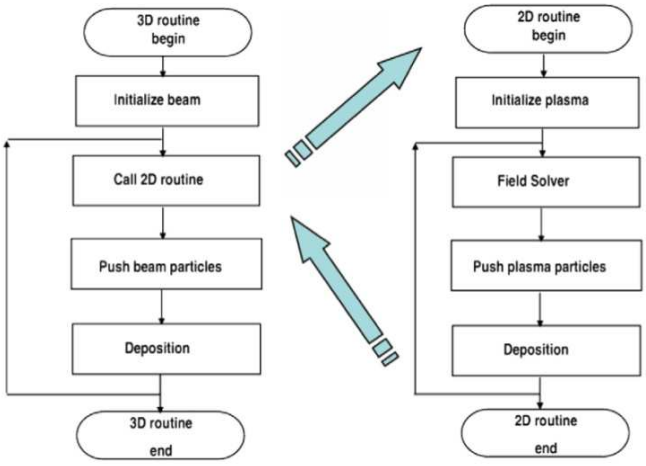

Figure 1.2: Flow chart of the QuickPIC quasi-static algorithm (taken from reference [43]).

1.4 The dissertation outline

Using the 3D quasi-static PIC code QuickPIC [43], several problems associated with PWFA are investigated in the dissertation. We begin by presenting important improvements to QuickPIC in Chapter 2. With these improvements, the new QuickPIC shows better accuracy, performance and parallel scalability, and is able to be used for all the simulation work in this dissertation. In Chapter 3, we discuss the two-bunch PWFA, which is a major experiment ongoing at FACET in SLAC. It aims at demonstrating a high energy gain as well as maintaining a narrow energy spread on a trailing beam. We also discuss two other issues that can be studied at FACET. They are the mitigation of ionization-induced head erosion and the optimum density for a given electron beam driver. For narrow trailing beams needed in some PWFA linear collider designs, the Coulomb force of the beam is large enough to pull plasma ions inwards during the transit time of the beam. This modifies the focusing force on the beam leading to emittance growth. In Chapter 4, we focus on the ion motion problem when accelerating an ultra-intense electron beam in the PWFA. The emittance growth of the accelerated electron beam is simulated with the sufficient resolution for the first time. In Chapter 5, we study the self-modulation of a long drive beam in the PWFA. The growth rate of the self-modulation instability (for electron, positron or proton beams) is theoretically analyzed under the wide-beam assumption. Preliminary simulation results are presented. In Chapter 6, we summarize the results presented in the dissertation and provide thoughts for future work.

CHAPTER 2

Developments in QuickPIC

As discussed in chapter 1, intense and short-pulse laser and particle beam–plasma interactions are now widely studied for a variety of applications most notably being plasma-based accelerators and light sources. In such interactions the radiation pressure of the laser or the electromagnetic forces of the particle beam create a plasma wave wake, which has a phase velocity roughly equal to that of the incoming laser/particle beam. This wake in turn provides an index of refraction modulation to the laser or electromagnetic forces on the particle beam causing its shape and frequency/energy content to change. The evolution of the laser/particle beam is on a much slower time and longer spatial scale than the period and wavelength of the wake. Therefore, the quasi-static description of these interactions was developed. This description is useful both theoretically and computationally. In this description the wake is calculated for a static (fixed) laser/particle beam. Then the nonlinear index of refraction is used to advance the laser and the wake fields are used to advance the particle beam. For quasi-static codes the time step used to advance the laser/particle beam is orders of magnitude larger than the frequency of the wake and this leads to significant speed ups compared to traditional codes. For most current problems of interest, the interactions are nonlinear and relevant particle based descriptions are desired.

Several particle-in-cell codes based on quasi-static assumption have been developed. WAKE [42] and LCODE [46] are two-dimensional (2D) azimuthally symmetric. WAKE can model both laser and particle-beam interactions while

LCODE can only model particle beam-plasma interactions. Whittum [47] developed a 3D quasi-static code for modeling particle beam-plasma interactions but he also applied further assumptions to simplify the algorithm. He assumed that plasma particles are only displaced in the transverse directions which is only appropriate for weakly nonlinear interactions. On the other hand QuickPIC [48] is a nonlinear, fully 3D quasi-static Particle-In-Cell (PIC) code. It was developed based on a fully nonlinear 3D algorithm, which is not just a simple extension from the 2D algorithms. QuickPIC can simulate the interaction of both a laser pulse and relativistic particle beam with a plasma. It can provide computational speed ups of $10^2 \sim 10^4$ with no loss in accuracy compared with a full PIC code (e.g. OSIRIS[39]). The speedup depends on the simulation parameters. QuickPIC has been widely used for investigating three dimensional effects in PWFA studies [49, 50, 51, 52, 53].

QuickPIC was developed using the UPIC framework [38]. It contains similar procedures as in a conventional PIC code, including the four basic modules: pushing the particles, depositing the current (charge) density, updating the fields, and interpolating the fields on each particle for pushing them. Furthermore, it is fully parallelized including a pipeline algorithm [45] allowing it to scale to more than 100,000 processors. The field equations are currently solved in Fourier space. The radiation pressure from the laser is derived from the ponderomotive guiding center approximation and the laser is advanced using an equation for its envelope.

In this chapter, several improvements to the algorithm used in QuickPIC will be presented. In the previous version of QuickPIC henceforth referred to as QuickPIC 1.0, a set of equations for the scalar and vector potential based on the Lorentz gauge were used. The QuickPIC 1.0 algorithm and the field equations in WAKE and LCODE are reviewed in section 2.1. In the newer version henceforth referred to as QuickPIC 2.0, a set of gauge invariant equations are solved. It is found that when using this new set of equations the number of iterations needed to get

accurate results (results that agree with OSIRIS) is significantly reduced (by at least a factor of 2.5) for a wide range of problems. The new algorithm is described in section 2.2. In addition, the predictor corrector loop requires pushing the particles forward to new positions in order to calculate the "time" (ξ) derivative of the current density. In the previous scheme in QuickPIC 1.0, the current density was calculated at a forward "time" (and position) and the derivative was obtained by subtracting the two values. This requires knowledge of the position of the particle at the forward time. Therefore, in parallel computations particles need to be moved to new processors according to their new positions inside the iteration loop. In the new scheme in QuickPIC 2.0, the "time" derivative of the current density is analytically calculated by taking the derivative for a finite size particle. As will be shown, this only requires calculating particle momentum at the forward time and not the particle position, so that no message passing of particle information is needed inside the iteration loop. This new deposition algorithm for the time derivative of the current density is described in section 2.3. In section 2.4, we compare the simulation results from QuickPIC 1.0, 2.0 and OSIRIS. In section 2.5, an improved field ionization module in QuickPIC is introduced. It allows us to simulate gases that have multiple ionization levels. In section 2.6 and 2.7, improvements to the initialization and diagnostic routines for the particle beam and plasma are presented respectively. Possible areas for the future development on QuickPIC are discussed in section 2.8. Lastly, a summary is given in section 2.9

2.1 The fields equations in QuickPIC 1.0

The basic difference between a quasi-static PIC code, e.g. QuickPIC, and a fully explicit PIC code, e.g. OSIRIS, is that the quasi-static code separates the time scale for the evolution (advancing in time) of the plasma from that of a short-pulse

laser or particle beam moving near the speed of light, c. The quasi-static approximation uses the coordinates $(x, y, \xi = ct - z, s = z)$ rather than the coordinates (x, y, z, t). The plasma particle trajectories are parameterized with the variable ξ (i.e., $[x(\xi), y(\xi), s(\xi)]$) while the trajectory of a beam particle is parameterized with the variable s (i.e., $[x(s), y(s), \xi(s)]$). The approximation uses the fact that for short pulses the s value for each plasma particle is essentially the same, so for a given value of s the trajectory is in a 2D (x, y) plane. In addition, the beam evolves very slowly in the variable s compared to the wavelength of the plasma response in the variable ξ. So when solving the field equations, it is assumed that $\partial/\partial s = 0$, which means we can drop all $\partial/\partial s$ and $\partial^2/\partial s^2$ terms in the fields equations that are solved.

In QuickPIC 1.0, we started from the potential equations for the potentials in the Lorentz gauge,

$$(\frac{\partial^2}{\partial t^2} - \nabla^2)\phi = \rho,$$

$$(\frac{\partial^2}{\partial t^2} - \nabla^2)\vec{A} = \vec{J},$$

and

$$\nabla \cdot \vec{A} + \frac{\partial \phi}{\partial t} = 0,$$

where henceforth we use normalized units. The potentials $(\phi, \vec{A})$ are normalized to $m_e c^2/e$, the charge density is normalized to en_0, the current density is normalized to $en_0 c$, the time is normalized to ω_{p0}^{-1} and the distance is normalized to c/ω_{p0}, where $\omega_{p0} = 4\pi e^2 n_0/m_e$ is the plasma frequency for a plasma of density n_0. Upon applying the quasi-static approximation, the wave equations for the potentials in the Lorentz gauge condition reduce to,

$$\nabla_\perp^2 \phi = -\rho,$$

$$\nabla_\perp^2 \vec{A} = -\vec{J},$$

and

$$\nabla_\perp \cdot \vec{A}_\perp = -\frac{\partial \psi}{\partial \xi},$$

where $\nabla_\perp \equiv \partial/\partial x\, \hat{x} + \partial/\partial y\, \hat{y}$, $\vec{A}_\perp = A_x \hat{x} + A_y \hat{y}$ and $\psi = \phi - A_z$ is the pseudo or wake potential. According to the above potential equations, ψ must satisfy,

$$\nabla_\perp^2 \psi = -(\rho - J_z) \tag{2.1}$$

The pseudo potential determines all the forces on a particle moving near c (i.e., a beam particle) along z, and it is needed to obtain the forces on and the current density from the plasma particles in QuickPIC [48]. In addition to ψ, we also need to calculate other fields to obtain the full electromagnetic force on the plasma particles. In terms of potentials, the electric and magnetic fields are given by $\vec{E} = -\nabla\phi - \partial\vec{A}/\partial t$ and $\vec{B} = \nabla \times \vec{A}$. After taking the quasi-static approximation, the various components of the fields are,

$$\vec{E}_\perp = -\nabla_\perp \phi - \frac{\partial \vec{A}_\perp}{\partial \xi}, \tag{2.2}$$

$$E_z = \frac{\partial \psi}{\partial \xi}, \tag{2.3}$$

$$\vec{B}_\perp = (\nabla_\perp A_z + \frac{\partial \vec{A}_\perp}{\partial \xi}) \times \hat{z}, \tag{2.4}$$

and

$$B_z = \nabla_\perp \cdot (\vec{A}_\perp \times \hat{z}). \tag{2.5}$$

In the above equations the electric and magnetic fields are normalized to $m_e c\omega_0/e$.

Besides $\vec{A}_\perp$, we also need $\partial\vec{A}_\perp/\partial\xi$ to calculate the forces. According to the equations in the Lorentz gauge, it satisfies

$$\nabla_\perp^2 \frac{\partial \vec{A}_\perp}{\partial \xi} = -\frac{\partial \vec{J}_\perp}{\partial \xi},$$

which is obtained by taking the derivative with respect to ξ of both sides of the equation $\nabla_\perp^2 \vec{A} = -\vec{J}$.

In the PIC method, the field (force) equations are advanced forward in time together with the particle's momentum and position. In a fully explicit code the equations can be leap frogged forward due to the natural time centering of the quantities. However, in the quasi-static algorithm the equations for ϕ and $\partial\vec{A}_\perp/\partial\xi$ (which are needed to calculate the electromagnetic fields) at a given time step require knowledge of ρ and $\partial\vec{J}_\perp/\partial\xi$, which depend on the electromagnetic fields (and potentials) at the next step. For example, to calculate ρ in the quasi-static variables (at a given ξ) one needs γ while $\partial\vec{J}_\perp/\partial\xi$ is due to the acceleration $\partial\vec{v}_\perp/\partial\xi$ for each particle. Therefore, we handle these implicitly coupled relationships between fields and particle quantities using an iteration predictor corrector scheme by solving the following potential equations instead,

$$\nabla_\perp^2 \phi^{new} - \phi^{new} = -\rho - \phi^{old},$$

and

$$\nabla_\perp^2 \frac{\partial \vec{A}_\perp^{new}}{\partial \xi} - \frac{\partial \vec{A}_\perp^{new}}{\partial \xi} = -\frac{\partial \vec{J}_\perp}{\partial \xi} - \frac{\partial \vec{A}_\perp^{old}}{\partial \xi}.$$

As noted in [48], these equations can be viewed as diffusion equations where the time is the iteration index. In each iteration, we predict the particles' positions and momenta at the advanced time step. These are used to calculate the predicted fields (from predicted potentials), which are then used to update the particle position and momentum to obtain corrected fields and then corrected particle position and momentum. In QuickPIC the field (potential) equations are solved

in $\vec{k}$ space using the Fast Fourier Transforms (FFT) method [48]. This iteration loop can be run an arbitrary number of times. More details can be found in [48] and we reproduce Table 2.1 from the paper [48] to list which quantities are known and which need to be predicted at a given time step.

	$\xi - 1/2\Delta\xi$	ξ	$\xi + 1/2\Delta\xi$	$\xi + \Delta\xi$	$\xi + 3/2\Delta\xi$
(1)	ψ,$\frac{\partial \vec{J}_\perp}{\partial \xi}$	$\vec{p}_\perp$,$\vec{J}_\perp$	$\vec{x}_\perp$		
(2)		$\vec{A}_\perp$,$\nabla_\perp \cdot \vec{A}_\perp$	ψ		
(3)			$\vec{J}_\perp$,$\frac{\partial \vec{J}_\perp}{\partial \xi}$,$\gamma$,$\rho$		
(4)			ϕ,$A_\parallel$,$\frac{\partial \vec{A}_\perp}{\partial \xi}$,$\nabla_\perp \cdot \vec{A}_\perp$, $\vec{B}_\perp$,B_z,$\vec{E}_\perp$	ψ,$\vec{p}_\perp$,p_z,$\vec{J}_\perp$	$\vec{x}_\perp$

Table 2.1: Quantities solved in QuickPIC 1.0:(1) Known quantities;(2)Quantities calculated before the iteration;(3)Quantities predicted (in the first iteration) or corrected (after the first iteration);(4)Quantities known after the iteration.

For many cases, we need to run through the iteration loop at least 4 times to obtain an accurate result (we will show the simulation results later).

There are two 2D quasi-static PIC codes that have been described in detail, WAKE [42] and LCODE [46]. WAKE was the first quasi-static PIC simulation code. It uses 2D cylindrical coordinates and it can model both a laser (using the ponderomotive guiding center method) and a particle beam driver. It assumes azimuthal symmetry and currently does not allow applied fields. Therefore, it only needs two fields to push the particles. They are B_θ and $\partial\psi/\partial r$ (note that $\partial\psi/\partial r = (\nabla_\perp \psi)_r = -E_r + B_\theta$). The field equations used in WAKE are,

$$\nabla_\perp^2 \frac{\partial^2 \psi}{\partial \xi^2} = \frac{1}{r}\frac{\partial}{\partial r}\frac{\partial J_r}{\partial \xi},$$

and

$$\frac{1}{r}\frac{\partial}{\partial r} r B_\theta = \frac{\partial^2 \psi}{\partial \xi^2} + J_z.$$

In WAKE, $\partial^2\psi/\partial\xi^2$ is solved in order to obtain ψ and $\partial\psi/\partial r$. Just as in QuickPIC, WAKE also needs an iteration loop for solving those equations. The equation for $\partial^2\psi/\partial\xi^2$ is therefore modified to,

$$(\nabla_\perp^2 - 1)\frac{\partial^2\psi^{new}}{\partial\xi^2} = \frac{1}{r}\frac{\partial}{\partial r}(\frac{\partial J_r^{old}}{\partial\xi} - rB_\theta^{old}) + J_z^{old}.$$

LCODE also uses 2D cylindrical coordinates and therefore assumes azimuthal symmetry. However, it uses a different set of fields equations,

$$\frac{\partial}{\partial r}\frac{1}{r}\frac{\partial}{\partial r}rE_r = \frac{\partial\rho}{\partial r} - \frac{\partial J_r}{\partial\xi},$$

$$\frac{\partial}{\partial\xi}(E_r - B_\theta) = \frac{\partial E_z}{\partial r} = J_r,$$

and

$$\frac{1}{r}\frac{\partial}{\partial r}rE_r = \rho - \frac{\partial E_z}{\partial\xi}.$$

Note that in LCODE there are additional equations for the field components E_θ, B_r and B_z. It assumes azimuthal symmetry but it allows for including applied fields such as an axial magnetic field. However, without applied fields, E_θ, B_r and B_z are zero (this is the reason that WAKE does not need to solve for these terms), so for simplicity we do not include them here. Just as for QuickPIC and WAKE, the fields equations and particle advances need to be solved iteratively. In LCODE, the equation of E_r is modified into the following form,

$$\frac{\partial}{\partial r}\frac{1}{r}\frac{\partial}{\partial r}rE_r^{new} - E_r^{new} = \frac{\partial\rho}{\partial r} - \frac{\partial J_r}{\partial\xi} - E_r^{old}.$$

Once E_r is known then B_θ and E_z can be obtained from the other two equations. In LCODE the electric and magnetic fields are solved for directly without using the potentials, so the equations are gauge invariant. Although the equations used in WAKE are derived using the transverse Coulomb gauge, the final set of equations is also gauge invariant (note the pseudo potential is gauge invariant).

Unlike in WAKE and LCODE, the equations for ϕ and $\vec{A}_\perp$ used in QuickPIC 1.0 are gauge dependent. In QuickPIC 1.0 we use diffusion like equations in

the iteration loop for two potentials (three scalar quantities) while in WAKE and LCODE only one equation (one scalar) cast in a diffusion like form. In addition, WAKE typically needs only 1 iteration to obtain an accurate result while QuickPIC 1.0 typically requires 4 or more for nonlinear cases. Motivated by these observations we have designed a new field solver using gauge invariant equations and that uses only one diffusion like vector equation (two scalar quantities). This is described next.

2.2 The new EM field solver in QuickPIC: QuickPIC 2.0

Instead of solving the equations for the scalar and vector potential based on the Lorentz gauge, we want to calculate ψ and the electromagnetic fields directly from the current and charge densities. We start from the Eq. (2.1) and the whole set of Maxwell equations under the quasi-static approximation. After transforming Maxwell equations into (x, y, ξ, s) coordinates using $\partial/\partial z = -\partial/\partial\xi + \partial/\partial s$, $\partial/\partial t = \partial/\partial\xi$ and omitting the terms with $\partial/\partial s$ and $\partial^2/\partial s^2$, we are left with,

$$\nabla_\perp \times \vec{E}_\perp = -\frac{\partial}{\partial\xi} B_z \hat{z}, \tag{2.6}$$

$$\nabla_\perp \times E_z \hat{z} = -\frac{\partial}{\partial\xi}(\vec{B}_\perp - \hat{z} \times \vec{E}_\perp), \tag{2.7}$$

$$\nabla_\perp \times \vec{B}_\perp - J_z \hat{z} = \frac{\partial}{\partial\xi} E_z \hat{z}, \tag{2.8}$$

$$\nabla_\perp \times B_z \hat{z} - \vec{J}_\perp = \frac{\partial}{\partial\xi}(\vec{E}_\perp + \hat{z} \times \vec{B}_\perp), \tag{2.9}$$

$$\nabla_\perp \cdot \vec{E}_\perp - \rho = \frac{\partial}{\partial\xi} E_z, \tag{2.10}$$

$$\nabla_\perp \cdot \vec{B}_\perp = \frac{\partial}{\partial\xi} B_z, \tag{2.11}$$

where $\nabla_\perp = \hat{x}\partial/\partial x + \hat{y}\partial/\partial y$. We write the equations for the transverse (x, y) and longitudinal (z) fields separately. In each of these equations, all the $\partial/\partial\xi$ like terms are gathered on the right hand side. That is because, in the part of

QuickPIC in which the plasma response is calculated, ξ acts like the time variable and all the quantities are advanced forward in ξ. In Eqs. (2.7) and (2.9), we see two linear combinations of $\vec{E}_\perp$ and $\vec{B}_\perp$, $\vec{B}_\perp - \hat{z}\times\vec{E}_\perp$ and $\vec{E}_\perp + \hat{z}\times\vec{B}_\perp$. The second one is the transverse force (so called focusing force) on a charge moving near c in the $\hat{z}$ direction (the sign depends on the sign of the charge). In addition, these two linear combinations are related because $\vec{B}_\perp - \hat{z}\times\vec{E}_\perp = (\vec{E}_\perp + \hat{z}\times\vec{B}_\perp)\times\hat{z}$. Furthermore, we can deduce the following equations from Eqs. (2.6), (2.8), (2.10) and (2.11),

$$\nabla_\perp \times (\vec{E}_\perp + \hat{z}\times\vec{B}_\perp) = 0, \tag{2.12}$$

and

$$\nabla_\perp \cdot (\vec{E}_\perp + \hat{z}\times\vec{B}_\perp) = \rho - J_z, \tag{2.13}$$

Those two equations show that focusing force $\vec{E}_\perp + \hat{z}\times\vec{B}_\perp$ can be obtained from a scalar potential and that this potential is the pseudo potential ψ, i.e.,

$$\vec{E}_\perp + \hat{z}\times\vec{B}_\perp = -\nabla_\perp\psi. \tag{2.14}$$

If one solves directly for the focusing force rather than for ψ, we just need to apply the operator $\nabla_\perp\times$ on both sides of equaiton (2.12). Then we will have,

$$\nabla_\perp^2(\vec{E}_\perp + \hat{z}\times\vec{B}_\perp) = \nabla_\perp(\rho - J_z).$$

The self-consistency of these equations and the quasi-static continuity equation can be obtained by taking the divergence of Eq. (2.9),

$$\nabla_\perp \cdot (\nabla_\perp \times B_z\hat{z} - \vec{J}_\perp) = \frac{\partial}{\partial\xi}\nabla_\perp \cdot (\vec{E}_\perp + \hat{z}\times\vec{B}_\perp)$$

After substituting Eq. (2.13) into the above equation, we have the continuity equation under the quasi-static approximation,

$$\frac{\partial}{\partial\xi}(\rho - J_z) + \nabla\cdot\vec{J}_\perp = 0. \tag{2.15}$$

Because the linear combinations of $\vec{E}_\perp$ and $\vec{B}_\perp$ in Eqs. (2.7) and (2.9) are not independent then we cannot advance $\vec{E}_\perp$ and $\vec{B}_\perp$ forward in ξ, so we need to solve for them directly using Poisson like equations. To derive these equations, we start from the wave equations for $\vec{E}$ and $\vec{B}$ that result from Maxwell's equations,

$$\nabla^2\vec{E} - \frac{\partial^2\vec{E}}{\partial t^2} = \nabla\rho + \frac{\partial\vec{J}}{\partial t},$$

and

$$\nabla^2\vec{B} - \frac{\partial^2\vec{B}}{\partial t^2} = -\nabla\times\vec{J}.$$

We then apply the quasi-static approximation to these equations to obtain,

$$\nabla_\perp^2\vec{B}_\perp = \hat{z}\times(\frac{\partial}{\partial\xi}\vec{J}_\perp + \nabla_\perp J_z), \tag{2.16}$$

$$\nabla_\perp^2 B_z = -\nabla_\perp\times\vec{J}_\perp, \tag{2.17}$$

$$\nabla_\perp^2\vec{E}_\perp = \nabla_\perp\rho + \frac{\partial}{\partial\xi}\vec{J}_\perp, \tag{2.18}$$

and

$$\nabla_\perp^2 E_z = \nabla_\perp\cdot\vec{J}_\perp. \tag{2.19}$$

Note that we have used the quasi-static continuity equation (equation (2.15)) to obtain equation (2.19). These equations are all 2D Poisson like equations so the fields all follow from 2D electrostatics.

For the new algorithm of QuickPIC 2.0, we use (2.1), (2.14), (2.16), (2.17) and (2.19) to solve for the electromagnetic fields in QuickPIC. We first solve the 2D like Poisson Eqs. (2.1) and (2.16) to obtain the pseudo potential ψ and $\vec{B}_\perp$. We then obtain $\vec{E}_\perp$ by subtracting $\hat{z}\times\vec{B}_\perp$ from $-\nabla_\perp\psi$ according to Eq. (2.14). While the source term for Eq. (2.1) is known at time centered values of ξ, the source term in Eq. (2.16) depends on the $\partial\vec{J}_\perp/\partial\xi$, which is not known at the appropriate

value of ξ so an iteration method is needed. We therefore change Eq. (2.16) into an iterative equation,

$$\nabla_\perp^2 \vec{B}_\perp^{new} - \vec{B}_\perp^{new} = \hat{z} \times (\frac{\partial}{\partial \xi} \vec{J}_\perp + \nabla_\perp \cdot J_z) - \vec{B}_\perp^{old}. \tag{2.20}$$

In QuickPIC 2.0, the coordinate ξ has a step length $\Delta\xi$ and quantities are advanced in ξ step by step. The particles are initialized with the particle momentum $\vec{p}(\xi)$ at an integer time step. In the code we use the proper velocity $\vec{p}(\xi) = \gamma\vec{v}(\xi)$ instead of the particle momentum, and the particle velocity can be obtained through $\vec{v} = \vec{p}/\gamma = \vec{p}/\sqrt{1+p^2+a^2/2}$, where $\vec{a}$ is the normalized vector potential of the laser drive beam.The particle position $\vec{x}(\xi + \Delta\xi/2)$ is initialized at a half integer time step (Note that the particle position is also known at $\vec{x}(\xi - \Delta\xi/2)$). The position is on the staggered ξ grid because we use the leap frog method to solve the particle motion equation. We now need to advance the particle momentum forward to the next integer step. From Eqs. (21) and (22) in Ref. [48], we know that,

$$\rho - J_z = \frac{1}{Volume} \sum_i \frac{q_i}{1 - v_{iz}} - \frac{1}{Volume} \sum_i \frac{q_i \cdot v_{iz}}{1 - v_{iz}} = \frac{1}{Volume} \sum_i q_i,$$

which means $\rho - J_z$ is independent of the particle velocity. Therefore, $\rho - J_z$ is known at values of ξ for which the position is known (half integer steps). We can thus determine ψ using Eq. (2.1) before we enter the iteration loop. In the iteration loop, we need to predict the current density $\vec{J}(\xi + \Delta\xi/2)$ and the derivative of the current density $\partial\vec{J}_\perp(\xi + \Delta\xi/2)/\partial\xi$ and this is done similarly as in QuickPIC 1.0. We use these predicted source terms in Eq. (2.20) to obtain the predicted value of $\vec{B}_\perp(\xi + \Delta\xi/2)$, where we use $\vec{B}_\perp^{old}(\xi + \Delta\xi/2) = \vec{B}_\perp(\xi - \Delta\xi/2)$. We then solve Eqs. (2.14), (2.17) and (2.19) to obtain all the predicted electromagnetic field components at $\xi + \Delta\xi/2$. We note that in WAKE the fields are predicted from previous values and their derivatives.

We then use the predicted forces to obtain the predicted particle momentum. The new particle momentum will be $\vec{p}(\xi + \Delta\xi)$ and the new particle position

will be $\vec{x}(\xi + 1.5\Delta\xi)$. We can obtain $\vec{x}(\xi + \Delta\xi)$ through $\vec{x}(\xi + \Delta\xi) = (\vec{x}(\xi + \Delta\xi/2) + \vec{x}(\xi + 1.5\Delta\xi))/2$ and then we deposit the current density and its derivative to get the corrected values. Similar to QuickPIC 1.0, this could be done by depositing the new (corrected) current density at the next integer step $\vec{J}(\xi + \Delta\xi)$ and then obtaining $\vec{J}(\xi + \Delta\xi/2)$ by averaging the quantities between ξ and $\xi + \Delta\xi$. The derivative of the current $\partial\vec{J}_\perp(\xi + \Delta\xi/2)/\partial\xi$ can then be obtained from $\partial\vec{J}_\perp(\xi + \Delta\xi/2)/\partial\xi = (\vec{J}_\perp(\xi + \Delta\xi) - \vec{J}_\perp(\xi))/\Delta\xi$. Actually, the calculation of the corrected derivative of the current density $\partial\vec{J}_\perp(\xi + \Delta\xi/2)/\partial\xi$ is done differently in QuickPIC 2.0 in order to reduce the communication between processors in parallel computations, and this will be described in the next section. With the new current density and its time derivative, we finish the iteration loop by recalculating the $\vec{B}_\perp$ and other fields to obtain corrected forces to advance the particles to their corrected momenta and positions. If desired, the iteration can be repeated. At the end, the values for the current density and its derivative are calculated for the next ξ. Table 2.2 describes the quantities we solve in QuickPIC 2.0 and their roles in each iteration loop. In the next section, we will introduce the new method for calculating $\partial\vec{J}_\perp(\xi + \Delta\xi/2)/\partial\xi$.

	$\xi - 1/2\Delta\xi$	ξ	$\xi + 1/2\Delta\xi$	$\xi + \Delta\xi$	$\xi + 3/2\Delta\xi$
(1)	ψ,$\vec{J}$, $\frac{\partial\vec{J}_\perp}{\partial\xi}$	$\vec{p}$, γ	$\vec{x}_\perp$		
(2)			$\rho - J_z$, ψ, $\nabla_\perp\psi$		
(3)			$\vec{J}$, $\frac{\partial\vec{J}_\perp}{\partial\xi}$, γ		
(4)			$\vec{E}$,$\vec{B}$	$\vec{p}$, γ	$\vec{x}_\perp$

Table 2.2: Quantities solved in QuickPIC 2.0:(1) Known quantities;(2)Quantities calculated before the iteration;(3)Quantities predicted (in the first iteration) or corrected (after the first iteration);(4)Quantities known after the iteration.

2.3 Depositing the time derivative of the current density

In the last section, we showed that in the iteration loop we need to calculate $\vec{J}_\perp(\xi+\Delta\xi/2)$ and $\partial\vec{J}_\perp(\xi+\Delta\xi/2)/\partial\xi$. In QuickPIC 1.0 this is done by calculating $\vec{J}_\perp(\xi+\Delta\xi)$ and the average and difference of it with $\vec{J}_\perp(\xi)$. When using domain decomposition, such a scheme requires repartitioning the particles twice within a single pass through the iteration loop. The first particle repartition happens because we need to update the particle position from $\vec{x}(\xi+\Delta\xi/2)$ to $\vec{x}(\xi+\Delta\xi)$ in order to deposit the current density at $\xi+\Delta\xi$. When the particle position changes, the code needs to move some particles among the processors to make sure they stay in the right partition. The other particle repartition happens at the end of the each pass through the iteration loop. Before we correct the particle position and momentum we need to restore the particle position $\vec{x}(\xi+\Delta\xi/2)$ (the code stores the particle positions at $\xi+\Delta\xi/2$ in the extra memory as well as the velocities at ξ) in order to correct the particle push. This requires redistributing the particles among the processors once again.

If we do not change the particle position within the iteration loop, we will not need to repartition the particles during each iteration. This will save the computer memory needed to store the original particle data and more importantly will speed up the loop since particle repartitioning is a parallel procedure which requires message passing among the processors. We accomplish this by depositing $\vec{J}(\xi+\Delta\xi/2)$ and $\partial\vec{J}_\perp(\xi+\Delta\xi/2)/\partial\xi$ directly at $\xi+\Delta\xi/2$. This method was first introduced in developing a PIC code using the Darwin model [54, 55]. Although different, the quasi-static and Darwin algorithms have many similarities including the ability to use this method. In QuickPIC, for calculating $\vec{J}(\xi+\Delta\xi/2)$, we need to know the particle momentum at $\xi+\Delta\xi/2$. It can be easily calculated by using $\vec{p}(\xi+\Delta\xi/2)=(\vec{p}(\xi)+\vec{p}(\xi+\Delta\xi))/2$, where the $\vec{p}(\xi+\Delta\xi)$ is the corrected particle momentum obtained through the particle pushing. To deposit $\partial\vec{J}_\perp(\xi+\Delta\xi/2)/\partial\xi$,

we use a new method to directly deposit it at $\xi + \Delta\xi/2$ without changing the particle position. In QuickPIC, the following equation is used for depositing the current density[48],

$$\begin{aligned}
\vec{J} &= \frac{q}{\text{Volume}} \sum_i \frac{\vec{v}_i}{1 - v_z} S(\vec{x}_\perp - \vec{x}_{i\perp}) \\
&= \frac{q}{\text{Volume}} \sum_i \frac{\gamma \vec{v}_i}{\gamma(1 - v_z)} S(\vec{x}_\perp - \vec{x}_{i\perp}) \\
&= \frac{q}{\text{Volume}} \sum_i \frac{\vec{p}_i}{1 - \frac{q}{m}\psi} S(\vec{x}_\perp - \vec{x}_{i\perp}),
\end{aligned}$$

where $S(\vec{x})$ is the particle shape function. For $S(\vec{x})$ we include the interpolation function (we use linear particle shapes) and any smoothing function (we use Gaussions). In the above equation, we also utilize the constant of motion that exists under the quasi-static approximation[42], $\gamma - p_z = 1 - (q/m)\psi$ (note that this equation is for a plasma particle with an arbitrary charge mass ratio, and the p_z in the equation is the particle proper velocity in the z direction). After taking the ξ derivative of the current density, we obtain

$$\begin{aligned}
\frac{\partial}{\partial \xi}\vec{J}_\perp &= \frac{\partial}{\partial \xi} \frac{q}{\text{Volume}} \sum_i \frac{\vec{p}_{i\perp}}{1 - \frac{q}{m}\psi} S(\vec{x}_\perp - \vec{x}_{i\perp}) \\
&= \frac{q}{\text{Volume}} \left(\sum_i \frac{\frac{\partial}{\partial \xi}\vec{p}_{i\perp}}{1 - \frac{q}{m}\psi} S(\vec{x}_\perp - \vec{x}_{i\perp}) + \sum_i \frac{\vec{p}_{i\perp} \frac{\partial}{\partial \xi}(\frac{q}{m}\psi)}{(1 - \frac{q}{m}\psi)^2} S(\vec{x}_\perp - \vec{x}_{i\perp}) \right. \\
&\quad \left. - \sum_i \frac{\vec{p}_{i\perp}}{1 - \frac{q}{m}\psi} \frac{\partial \vec{x}_{i\perp}}{\partial \xi} \nabla_\perp \cdot S(\vec{x}_\perp - \vec{x}_{i\perp}) \right) \\
&= \frac{q}{\text{Volume}} \left(\sum_i \frac{\frac{\partial}{\partial \xi}\vec{p}_{i\perp}}{1 - \frac{q}{m}\psi} S(\vec{x}_\perp - \vec{x}_{i\perp}) + \sum_i \frac{\vec{p}_{i\perp} \frac{\partial}{\partial \xi}(\frac{q}{m}\psi)}{(1 - \frac{q}{m}\psi)^2} S(\vec{x}_\perp - \vec{x}_{i\perp}) \right. \\
&\quad \left. - \sum_i \frac{\vec{p}_{i\perp}}{1 - \frac{q}{m}\psi} \frac{\vec{p}_{i\perp}}{1 - \frac{q}{m}\psi} \nabla_\perp \cdot S(\vec{x}_\perp - \vec{x}_{i\perp}) \right) \\
&= \frac{q}{\text{Volume}} \left(\sum_i \frac{\frac{\partial}{\partial \xi}\vec{p}_{i\perp}}{1 - \frac{q}{m}\psi} S(\vec{x}_\perp - \vec{x}_{i\perp}) + \sum_i \frac{\vec{p}_{i\perp} \frac{\partial}{\partial \xi}(\frac{q}{m}\psi)}{(1 - \frac{q}{m}\psi)^2} S(\vec{x}_\perp - \vec{x}_{i\perp}) \right. \\
&\quad \left. - \nabla_\perp \cdot \sum_i \frac{\vec{p}_{i\perp}\vec{p}_{i\perp}}{(1 - \frac{q}{m}\psi)^2} S(\vec{x}_\perp - \vec{x}_{i\perp}) \right),
\end{aligned}$$

where $\vec{p}_{i\perp}\vec{p}_{i\perp}$ is a dyadic.

This equation shows that $\partial\vec{J}_\perp/\partial\xi$ can be obtained by depositing three different densities evaluated at the particles position at $\xi+\Delta\xi/2$. In the first term, $\partial\vec{p}_{i\perp}/\partial\xi$ at $\xi+\Delta\xi/2$ is the acceleration of the particle. In the second term, $\vec{p}_{i\perp}(\xi+\Delta\xi/2)$ is calculated from $\vec{p}_{i\perp}(\xi+\Delta\xi/2) = (\vec{p}_{i\perp}(\xi)+\vec{p}_{i\perp}(\xi+\Delta\xi))/2$ and $\partial(q/m\cdot\psi)/\partial\xi$ (note that here ψ is actually $\psi(\vec{x}_{i\perp})$)is calculated by

$$\frac{\partial}{\partial\xi}(\frac{q}{m}\psi) = \frac{q}{m}(\frac{\partial}{\partial\xi}\psi + \nabla_\perp\psi\cdot\frac{\partial\vec{x}_{i\perp}}{\partial\xi}) = \frac{q}{m}(E_z + \nabla_\perp\psi\cdot\frac{\vec{p}_{i\perp}}{1-\frac{q}{m}\psi})$$

Finally, in the third term, after depositing the density dyadic, $\vec{p}_{i\perp}\vec{p}_{i\perp}$, we calculate its divergence in Fourier space. None of these three parts requires updating the particle position, which ensures that we can calculate the $\partial\vec{J}_\perp(\xi+\Delta\xi/2)/\partial\xi$ locally within each processor and no particle relocation is required.

2.4 Simulation result comparison between QuickPIC 1.0 and 2.0

In this section, we compare the results from QuickPIC 1.0, 2.0 and OSIRIS when simulating physics of relevance to the PWFA. The PWFA uses a high energy particle beam to excite a large plasma wave wakefield inside the plasma. A second beam properly phased inside the wakefield can be focused and accelerated to high energy. QuickPIC is a very important tool for modeling PWFA and is used extensively in the later chapters of this dissertation.

We begin by simulating two PWFA cases in the linear regime. In the linear regime the density of the drive beam n_b is much smaller than the plasma density n_p. In one case, the drive beam has a spot size which is much smaller than the plasma skin depth, $c/\omega_p \equiv k_p^{-1}$. In the other case, the spot size is much larger than the plasma skin depth. In each case the drive beam has a Gaussian profile $n_b\exp(-r^2/2\sigma_r^2)\exp(-z^2/2\sigma_z^2)$ and a 20 GeV initial energy. The narrow drive

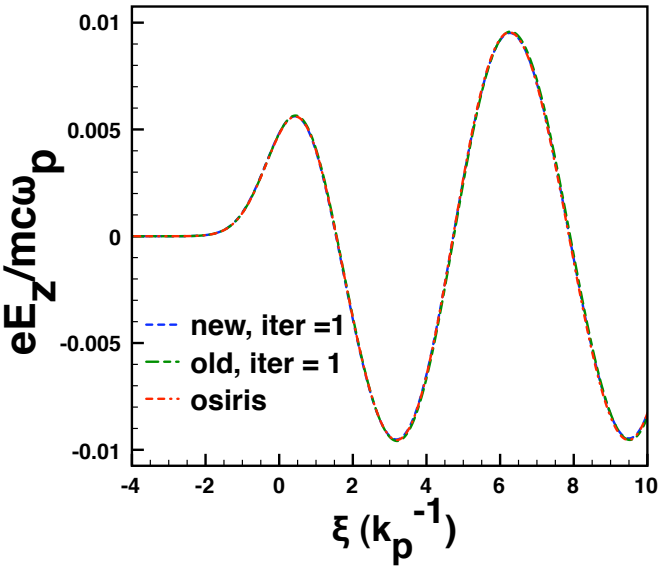

(a)

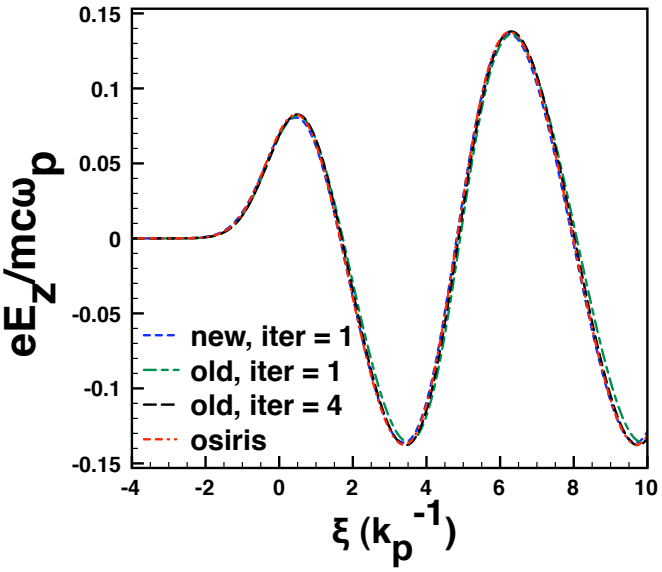

(b)

Figure 2.1: The longitudinal electric field lineouts on the axis from the electron-beam-driven PWFA simulations in the linear regime: (a) Results for the narrow beam case with QuickPIC 1.0 and 2.0 using 1 iteration and OSIRIS result; (b) Results for the wide beam case with QuickPIC 1.0 using 1 and 4 iterations, and QuickPIC 2.0 using 1 iteration and from OSIRIS.

beam has $k_p\sigma_r = 0.2$, $k_p\sigma_z = 0.75$ and $n_b/n_p = 0.1$ and the wide drive beam has $k_p\sigma_r = 5.64$, $k_p\sigma_z = 0.75$ and $n_b/n_p = 0.1$.

The simulation results are shown in the Fig. 2.1. In these plots, $\xi = 0$ is the beam center and the beam is moving to the left. In the linear regime, the drive beam excites a sinusoidal wave wakefield as shown in Fig. 2.1. In the narrow beam case, results from QuickPIC 1.0 and 2.0 both agree with OSIRIS [39] (red dashed line) after only 1 iteration. In the wide beam case, there is a slight difference between QuickPIC 1.0 with only 1 iteration and OSIRIS, while the results from QuickPIC 2.0 with only 1 iteration are still in excellent agreement with OSIRIS. By increasing the iteration number to 4, QuickPIC 1.0 agrees with the OSIRIS result as well as with the QuickPIC 2.0 result with only 1 iteration in this "wide" beam case.

Modeling nonlinear wakes is more challenging. The drive beam will excite a nonlinear plasma wave wakefield if the beam density is much larger than the plasma density (i.e., $n_b/n_p \gg 1$) or its normalized charge per unit length is larger than 1 (i.e., $\Lambda = (n_b/n_p)k_p^2\sigma_r^2 > 1$) [49]. We next present results from two nonlinear PWFA examples. In one the drive beam is narrow and in the other drive beam is wide. In the narrow drive beam case, the beam parameters are $k_p\sigma_r = 0.2$, $k_p\sigma_z = 0.75$ and $n_b/n_p = 20$. In the wide drive beam case, the beam parameters are $k_p\sigma_r = 5.64$, $k_p\sigma_z = 0.75$ and $n_b/n_p = 0.5$. For the wide beam case, the drive beam has a normalized charge per unit length equal to $\Lambda = (n_b/n_p)k_p^2\sigma_r^2 = 1.6$, which is in the nonlinear regime even though the beam density $n_b/n_p = 0.5$ is not very large. The simulation results are shown in Fig. 2.2 for the narrow beam case and Fig. 2.3 for the wide beam case.

In the narrow beam case, the E_z field increases along the ξ axis at the front and reaches its maximum value near the beam center. It then drops down almost linearly until it forms a deep spike at the rear of an ion bubble after which it rapidly rises. The positive E_z field around $\xi = 0$ (where is the center of the drive

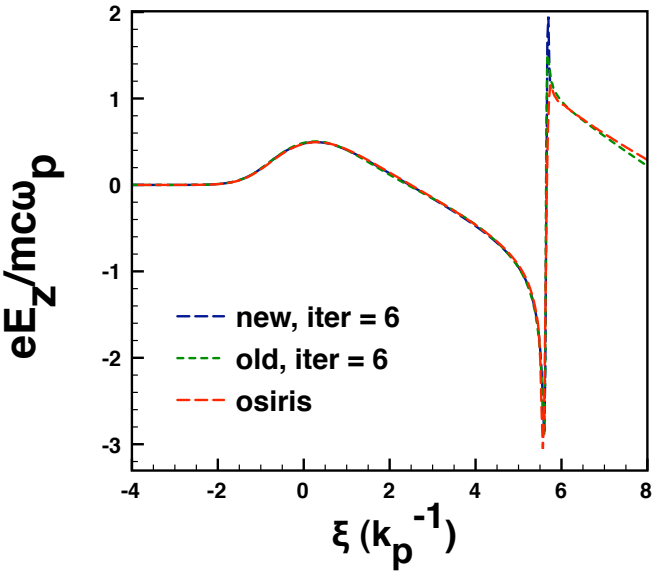

(a)

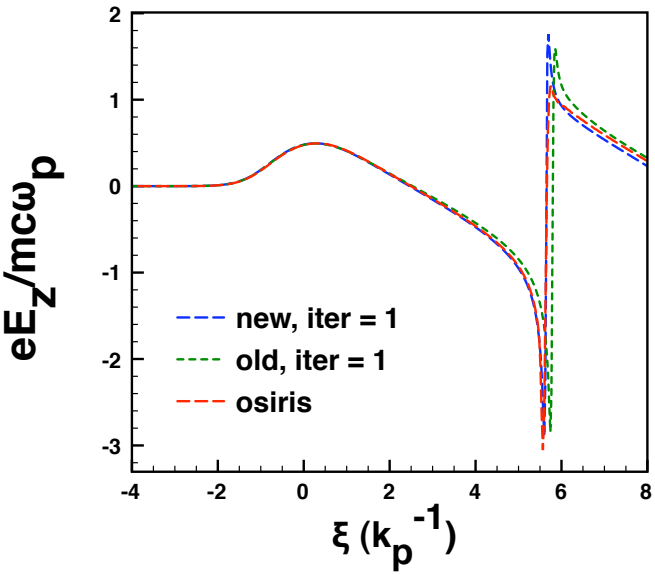

(b)

Figure 2.2: The longitudinal electric field lineouts on the axis from narrow electron-beam-driven PWFA simulations in the nonlinear regime: (a)Results from QuickPIC 1.0 and 2.0 simulations using 6 iterations and from OSIRIS; (b) Results from QuickPIC 1.0 and 2.0 simulation using 1 iteration and from OSIRIS.

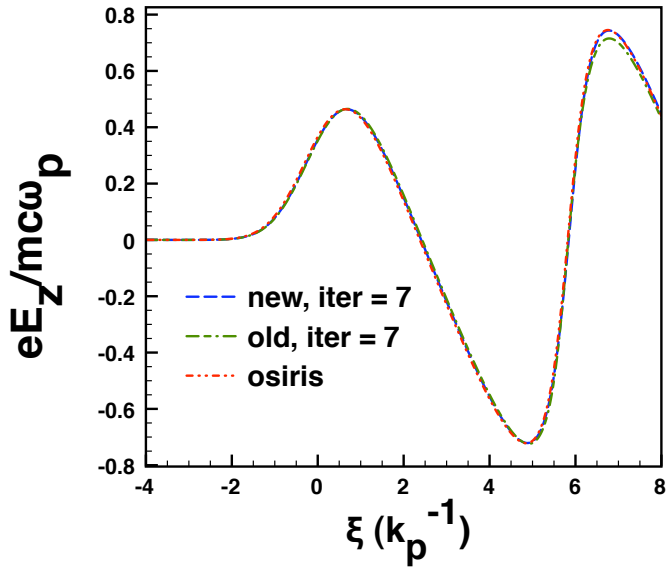

(a)

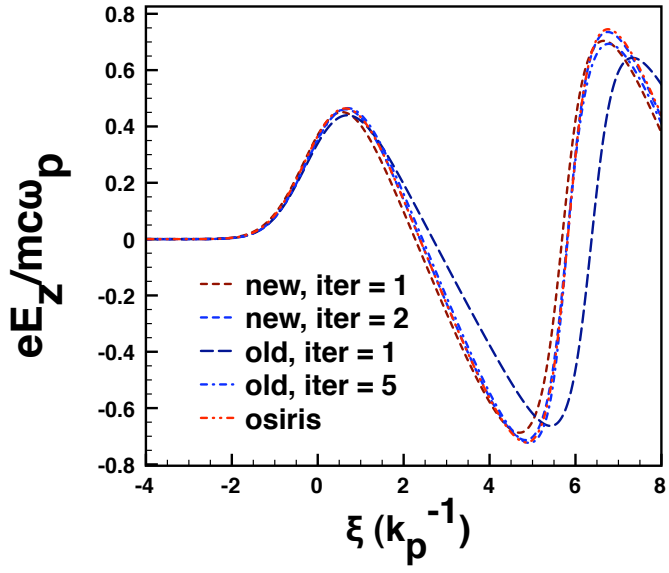

(b)

Figure 2.3: The longitudinal electric field lineouts on the axis from wide electron-beam-driven PWFA simulations in the nonlinear regime: (a) Results from QuickPIC 1.0 and 2.0 simulations using 7 iterations and from OSIRIS; (b) Results from QuickPIC 1.0 and 2.0 simulations with fewer iterations and from OSIRIS.

beam) will decelerate the drive beam, while the negative E_z can accelerate another electron beam. In Fig. 2.2(a), we can see that the solver in QuickPIC 1.0 and in QuickPIC 2.0 give the same results and agree with OSIRIS after 6 iterations. When only one iteration is used in each case (Fig. 2.2(b)), the results from the 2.0 version already overlap and are in excellent agreement with the OSIRIS result. However, results from the 1.0 version deviate from the OSIRIS result and require 4 or more iterations to obtain an accurate answer. In the wide beam case, wakes obtained from both versions of QuickPIC with 7 iterations agree well with OSIRIS. However, QuickPIC 2.0 converges much faster to the OSIRIS result. From Fig. 2.3(b), we can see that QuickPIC 2.0 needs only 2 iterations while QuickPIC 1.0 needs at least 5 iterations to converge.

The nonlinear plasma wake field driven by an electron beam is perfect for accelerating another electron beam. When a second trailing electron beam is properly loaded and shaped inside the wake field, the accelerating field can be flattened due to beam loading. The flattened accelerating field will result in a narrow energy spread of the accelerated beam. The Fig. 2.4 shows the simulation results from such a beam loading scenario. In this case, the drive beam's parameters are $k_p\sigma_r = 0.06$, $k_p\sigma_z = 1.78$ and $n_b/n_p = 634.9$ and the trailing beam's parameters are $k_p\sigma_r = 0.06$, $k_p\sigma_z = 0.59$ and $n_b/n_p = 634.9$. The distance between two beam centers is $k_pL = 6.83$. QuickPIC 2.0 requires only 1 iteration to obtain excellent result with OSIRIS.

In addition to an electron beam, a short positron or proton beam can also excite a "bubble" like wake field [34] that can be used for accelerating an electron trailing beam. Figure 2.5 shows the simulation results for such a case. The positron (proton) drive beam's parameters are $k_p\sigma_r = 0.93$, $k_p\sigma_z = 0.46$ and $n_b/n_p = 3.15$.

In this case, results from QuickPIC 2.0 are in excellent agreement with OSIRIS after 1 iteration. On the other hand QuickPIC 1.0 still does not converge to the

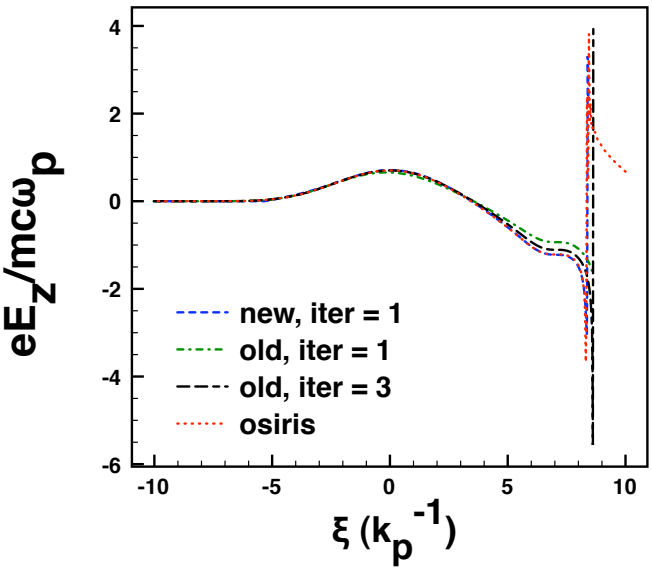

Figure 2.4: Lineouts of the longitudinal electric field on the axis from electron-beam-driven PWFA simulations in the nonlinear regime with a beam load. The lineouts include QuickPIC 2.0 simulation results with 1 iteration, QuickPIC 1.0 simulation results with 1 and 3 iterations and OSIRIS simulation results.

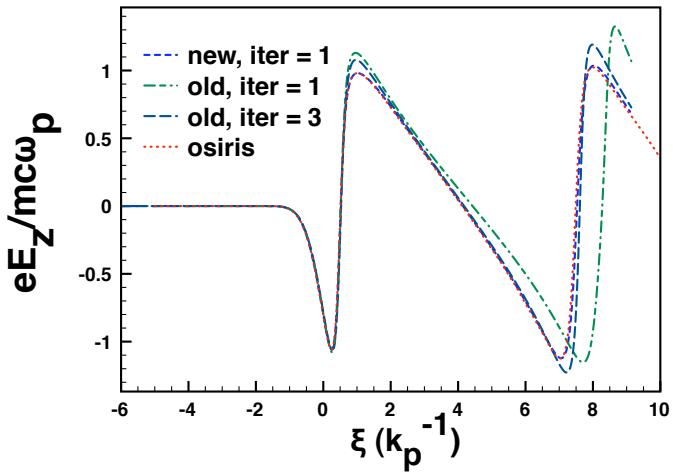

Figure 2.5: Lineouts of the longitudinal electric field on the axis from short positron-beam-driven PWFA simulations. The lineouts include QuickPIC 2.0 simulation results with 1 iteration, QuickPIC 1.0 simulation results with 1 and 3 iterations and OSIRIS simulation results.

correct result even after 3 iterations.

From all the simulations shown above, the results obtained from the algorithm in QuickPIC 2.0 converges more rapidly to the "correct", OSIRIS, result than the results from QuickPIC 1.0 do. In most of the cases, the QuickPIC 2.0 only needs 1 iteration to provide a correct result while QuickPIC 1.0 needs at least 4 iterations to reach the correct result. Note that by 1 iteration we mean that the field solve and particle push has been done twice and by 4 iterations we mean that they have been run for 5 times. Because the iteration loop contains all the particle pushing, current deposition, fields solving and field interpolation procedures, it takes most of the computing time in QuickPIC. The charge and current density deposition and particle update for the drive beam is typically less. Therefore, QuickPIC 2.0 is generally at least 5/2=2.5 times faster.

In addition, the new scheme for depositing $\partial\vec{J}_\perp/\partial\xi$ can also save much computing time on parallel computations. Figure 2.6 shows the QuickPIC 2.0 speedup compared with QuickPIC 1.0 for a test simulation. The test simulation is a nonlinear PWFA case with $512\times512\times512$ cells. Each simulation is run on 64 processors. We use double precision fro both the new and old versions of QuickPIC. For this test case, QuickPIC 1.0 used 4 iterations (the field solve and particle push loop is run 5 times) and QuickPIC 2.0 used only 1 iteration (the loop is run twice). From Fig. 2.6, we can see that the new code is 5 times faster than the old code when we use 4 particles per cell in the test simulation. And the speedup increases to 8.5 times when there are 25 particles per cell (i.e., more particles on each processor). This additional speed up and the increasing speed up with increasing particle number (5 or 8.5 rather than 2.5) is because of the reduced amount of parallel communication in the new deposition scheme in QuickPIC 2.0.

It is also worth commenting on the relative speed of the new version of QuickPIC and a full PIC code, e.g., OSIRIS. In the original QuickPIC paper [48], the number of particle updates needed to calculate the wake (a single 3D quasi-static

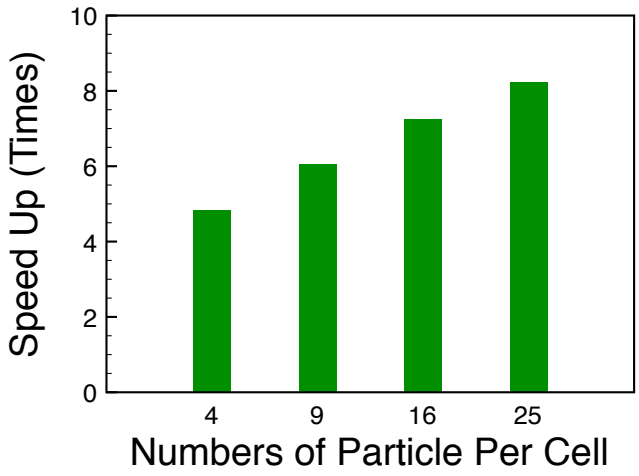

Figure 2.6: Total speed up of QuickPIC 2.0

time step for QuickPIC) or to propagate a beam a betatron wavelength for both a quasi-static and fully explicit PIC code was given. To translate this into the how long a simulation would take requires the speed of a particle update. The time it takes to update each particle (including the charge/current deposit and field solves) differs between QuickPIC and full PIC codes such as OSIRIS. The quasi-static code uses a 2D push not a 3D push, but it requires an iteration loop and a more complicated field solve. In addition, QuickPIC is spectral based and OSIRIS is FDTD based. Providing general estimates of the speeds is further complicated by the fact that the code timing depends on many factors, including numbers of processors (parallel scalability and load balancing), interpolation order, the use of SIMD units on each core, the problem (nonlinear or weakly nonlinear), and the number of particles per cell (in QuickPIC the field solve can dominate for a low number of particles per cell). Therefore, we simply provide timings for a 2D step in QuickPIC for one full iteration as well as some timing for OSIRIS for a thermal plasma test case.

The QuickPIC simulations used domains with $512\times512\times512$ cells and a typical beam driver. We used 64 processors for QuickPIC which is a typical number for

each 2D copy when using the pipelining method [45] for parallelization. We use double precision and linear interpolation. On Blue Waters, each 2D step (with 1 iteration) in QuickPIC takes 2500 ns/particle when using 4 particles per cell and 770 ns/particle when using 25 particles per cell for a weakly nonlinear PWFA case. And for a strongly nonlinear PWFA case the timings are very similar. On thermal plasma test cases, when applying the SSE vector units on Blue Waters, each 3D step in OSIRIS has achieved timings of ∼150 ns per particle using linear interpolation and ∼300 ns/particle using quadratic interpolation. On the new Intel E5-2680 (@2.7GHz), each 3D step in OSIRIS achieves 59.5 ns/particle with linear interpolation and 108.7 ns/particle with quadratic interpolation. Without the SSEs, OSIRIS is ∼2-3 times slower on most systems. In addition, for a nonlinear PWFA case the effective speed of OSIRIS can be ∼5 times slower due to load imbalance when running on a large number of processors. As mentioned earlier, the timings for QuickPIC do not differ that much between a nonlinear case and a linear as load balancing is not a significant problem. While it is not straightforward to compare these timings for the reasons stated, it is generally true that each 2D step in QuickPIC 2.0 including the iteration and field solve is comparable to a 3D step using OSIRIS.

2.5 The Field Ionization Module

In PWFA experiments, if the plasma is produced by ionizing the neutral gas using the particle beam's self Coulomb field, this so-called field-ionized plasma will have a nonuniform distribution in the space (we will show this later) since the beam's self Coulomb field is not uniform (which is zero on axis and falls off as $1/r$ for large r). The nonuniform field-ionized plasma will affect the particle beam evolution and can lead to a significant differences on wake excitation compared to a preformed uniform plasma conditions. Therefore we must include field ionization

into the PIC code to accurately study ongoing (and future) experiments. Here we describe the field ionization module, and recent improvements to it. Dr. Zhou first implemented the ionization module in QuickPIC [56, 57] based on the Ammosov-Deloine-Krainov (ADK) model [58, 59]. But that ionization module only included one ionization level for each neutral species and it was developed on the QuickPIC 1.0 without the pipeline algorithm. Therefore, we have updated the ionization module in order to make it work under the QuickPIC 2.0 with multiple ionization as well as the pipeline algorithm.

The ADK model can calculate the tunneling ionization rate of the neutral atoms or atomic ions in an external electric field whose amplitude is smaller than the critical value $E_{crit} = (\sqrt{2}-1)|\xi_i|^{3/2}$ [59]. The ADK model is very suitable to be implemented in the PIC code for modeling the PWFA and LWFA because for many cases of interest the Keldysh parameter $\gamma \ll 1$ indicating the external electric field has a low frequency [60] (rather than the multi-photon ionization $\gamma \gg 1$ indicating the external electric field has a high frequency and where multi-photo ionization [60]). For $\gamma \ll 1$ the ionization rate in the ADK model only depends on the local electric field and the ionization rate is given by [59]

$$w[\mathrm{s}^{-1}] \approx 1.52\times 10^{15}\frac{4^{n^*}\xi_i[\mathrm{eV}]}{n^*\Gamma(2n^*)}\left(20.5\frac{\xi_i^{3/2}[\mathrm{eV}]}{E[\mathrm{GV/m}]}\right)^{2n^*-1}\times\exp\left(-6.83\frac{\xi_i^{3/2}[\mathrm{eV}]}{E[\mathrm{GV/m}]}\right),$$

where ξ_i is the ionization energy of the atom or the atomic ion, $n^* \approx 3.69Z/\xi_i^{1/2}[\mathrm{eV}]$ is the effective principle quantum number, Z is the charge number of the ion after ionization, Γ is the standard gamma function and E is the magnitude of the local electric field. The density of the atoms being ionized n_0 satisfies,

$$\frac{dn_0(\vec{x},t)}{dt} = -w_0(E(\vec{x},t))n_0(\vec{x},t), \tag{2.21}$$

where w_0 is the ionization rate of the neutral atom. QuickPIC uses the coordinates ($\vec{x}_\perp$, $\xi = t - z$, $s = z$) rather than ($\vec{x}_\perp$, z, t). The density is considered at fixed $s = s_0$ but different t (i.e., different ξ). Therefore $d\xi = dt(1 - v_z)$ and the above

rate equation becomes

$$\frac{dn_0(\vec{x}_\perp, \xi)}{d\xi} = -\frac{w_0(E(\vec{x}_\perp, \xi))}{1 - v_z} n_0(\vec{x}_\perp, \xi).$$

However, for neutral (and ionized ions) $v_z \sim 0$, so one can simply replace t with ξ in the rate equation (2.21). To solve this equation along the ξ with a step length $\Delta\xi$, we can discretize the above equation into

$$n_0(\xi_0 + \Delta\xi) = n_0(\xi_0)(1 - w_0(\xi_0)\Delta\xi),$$

where $w_0(\xi_0) \equiv w_0(E(\vec{x}_\perp, \xi_0))$ for simplicity. Thus, when we know the quantities n_0 and w_0 on ξ_0, we can calculate the n_0 on the next step $\xi_0 + \Delta\xi$. But this is a first order method and $w_0(\xi_0)\Delta\xi$ need to be less than 1. To solve this equation more accurately, we can assume the ionization rate does not change between ξ_0 and $\xi_0 + \Delta\xi$. By integrating the rate equation for n_0, we have

$$n_0(\xi_0 + \Delta\xi) = n_0(\xi_0) e^{-w_0(\xi_0)\Delta\xi}.$$

This solution is more accurate and does not need $w_0(\xi_0)\Delta\xi$ to be less than 1. If the second (or more) ionization is allowed, we need to calculate the density of the singly charged ion species n_1. The equation for n_1 is

$$\frac{dn_1(\xi)}{d\xi} = w_0(\xi)n_0(\xi) - w_1(\xi)n_1(\xi),$$

where w_1 is the ionization rate of the singly charged ion. Assuming w_1 also does not change during the interval of $\Delta\xi$, we can solve the above equation by substituting the solution of $n_0 = n_0(\xi_0)\exp(-w_0(\xi_0)\xi)$. Then we can have

$$n_1(\xi_0 + \Delta\xi) = \left(n_1(\xi_0) - \frac{w_0(\xi_0)n_0(\xi_0)}{w_1(\xi_0) - w_0(\xi_0)} \right) e^{-w_1(\xi_0)\Delta\xi} + \frac{w_0(\xi_0)n_0(\xi_0)}{w_1(\xi_0) - w_0(\xi_0)} e^{-w_0(\xi_0)\Delta\xi}.$$

These can be straight forwardly generalized for more ionization steps. The rate equation for the ion density $n_m + 1$ is,

$$\frac{dn_{m+1}(\xi)}{d\xi} = w_m(\xi)n_m(\xi) - w_{m+1}(\xi)n_{m+1}(\xi).$$

Note that the other ion densities $n_0, \ldots n_{m-1}$do not appear in the above equation because the ADK model can only calculate the single ionization rate for an atom or an atomic ion but not the rate of the spontaneous multiple ionization. Suppose we know the ion density n_m,

$$n_m(\xi) = \sum_{i=0}^{m} C_i^m e^{-w_i \xi},$$

where $w_i = w_i(\xi_0)$ $(i = 0, \ldots, m)$ is the ionization rate for the neutral atom $(i = 0)$ or the i-valent ion $(i > 0)$ and C_i^m $(i = 0, \ldots, m)$ is the coefficient in front of each term of $e^{-w_i \xi}$. Upon substituting n_m into the rate equation for n_{m+1}, we can solve it to get

$$n_{m+1}(\xi_0 + \Delta\xi) = \left(n_{m+1}(\xi_0) - \sum_{i=0}^{m} \frac{C_i^m}{w_{m+1} - w_i} \right) e^{-w_{m+1}\Delta\xi} + \sum_{i=0}^{m} \frac{C_i^m}{w_{m+1} - w_i} e^{-w_i \Delta\xi}.$$

Then we know the coefficient C_i^{m+1}, $(i = 0, \ldots, m+1)$ for the ion density n_{m+1},

$$C_{m+1}^{m+1} = n_{m+1}(\xi_0) - \sum_{i=0}^{m} \frac{C_i^m}{w_{m+1} - w_i}, \quad C_i^{m+1} = \frac{C_i^m}{w_{m+1} - w_i}, \ (i = 0, \ldots, m).$$

These coefficients can be used to calculate C_i^{m+2} for the next ionization level and so on.

After all ion densities $n_m(\xi_0 + \Delta\xi)$ are calculated, we can inject the macro particles at the $\xi_0 + \Delta\xi$ according to the sum of ion density increments,

$$\sum_{m=1}^{M} \Delta n_m = \sum_{m=1}^{M} (n_m(\xi_0 + \Delta\xi) - n_m(\xi_0)),$$

where M is the maximum ionization level in the simulation. To enable the pipeline algorithm, we need to send the ion densities at the last slice (i.e., the last ξ step) of the current stage to the next stage as its initial value for the first ξ step.

Figures 2.7 and 2.8 show the results from a QuickPIC 2.0 simulation for a PWFA case with a field ionization produced plasma. The electron drive beam's parameters are $k_p\sigma_r = 0.42$, $k_p\sigma_z = 1.43$ and $n_b/n_p = 3.56$. The neutral gas used in the simulation is Cesium. Excellent agreement between OSIRIS and QuickPIC 2.0 is obtained after 1 iteration.

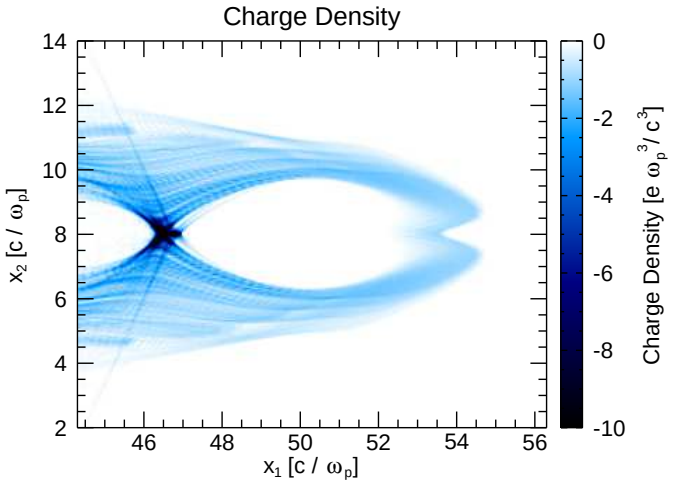

(a)

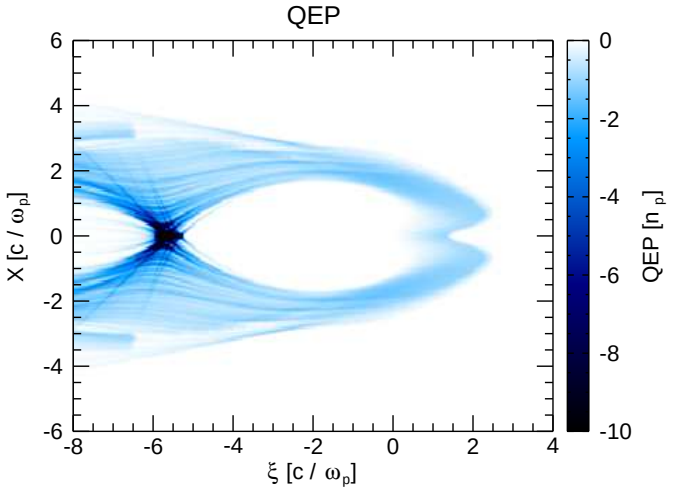

(b)

Figure 2.7: The field-ionized plasma density: (a) OSIRIS result; (b) QuickPIC 2.0 result.

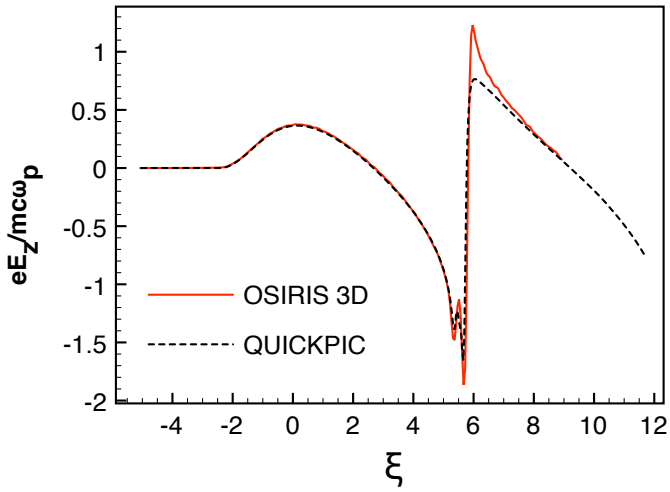

(a)

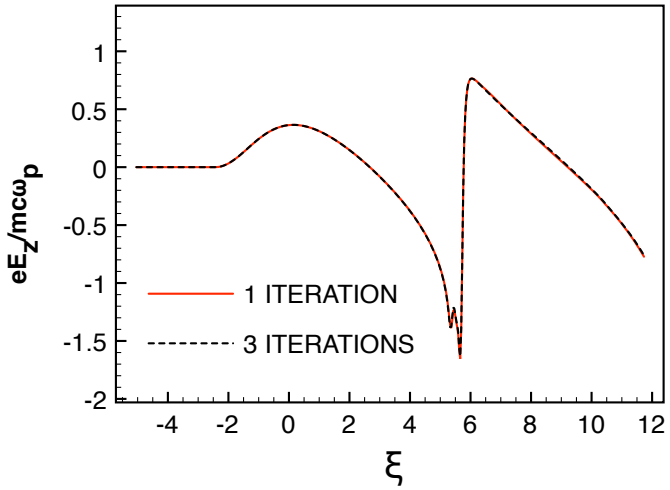

(b)

Figure 2.8: Lineouts of the longitudinal electric field on the axis: (a) OSIRIS result and QuickPIC 2.0 result with 1 iteration; (b) QuickPIC 2.0 result with 1 and 3 iterations

2.6 Improvements to beam initialization and particle diagnostics

In QuickPIC, we normally initialize the beam particles' positions and velocities according to a given distribution profile (e.g. the Gaussian profile). But in the real PWFA experiments, the particle beam usually does not have a distribution given by a known function in the six dimensional phase space. The distribution can be obtained from accelerator simulations using codes (such as the Elegant [61]). Furthermore, the distribution is generally not separate $f(x, y, z, p_x, p_y, p_z) \neq X(x)Y(y)Z(z)P_x(p_x)P_y(p_y)P_z(p_z)$. We have developed the ability to initialize a particle beam in QuickPIC using the raw data from an accelerator code. Previously, we developed the ability to take raw data from an accelerator code and use it to generate a distribution of the form $f_x(x, p_x)f_y(y, p_y)f_z(z, p_z)$ and then use this to initialize a beam in QuickPIC [62]. This method cannot reconstruct the correlation between all six dimensional phase space coordinates. In order to do that, we need to directly import the beam particles' raw data into QuickPIC. This was implemented into the current version of QuickPIC. When QuickPIC is initialized, all the computing processors will read the same external file that contains all the beam particles' raw data, which is obtained through the accelerator simulation code. Each processor then checks through all the beam particles and only keeps those belonging to its partition. This method requires that the number of the beam particles imported into QuickPIC should be large enough in order to reduce the numerical noise when depositing the beam charge density on the grid point. Normally, the particle number we need is $N = 6^3(\sigma_x/\Delta_x)(\sigma_y/\Delta_y)(\sigma_z/\Delta_z)$, where $\sigma_{x,y,z}$ is the r.m.s. beam length in each direction and $\Delta_{x,y,z}$ is the cell size in each direction. In Figure 2.9 we show an example of an external beam initialized in QuickPIC from an Elegant simulation. The raw particle data comes from a simulation of a SLAC electron beam. The peak energy of the beam is around

23 GeV. The beam has 45.1 μm and 9.8 μm r.m.s. spot sizes (calculated from the raw data) in two transverse directions. There is also a little bump at the beam tail if we look at the projections in the plot. But this bump tail is dispersed in a complicated manner in the transverse directions.

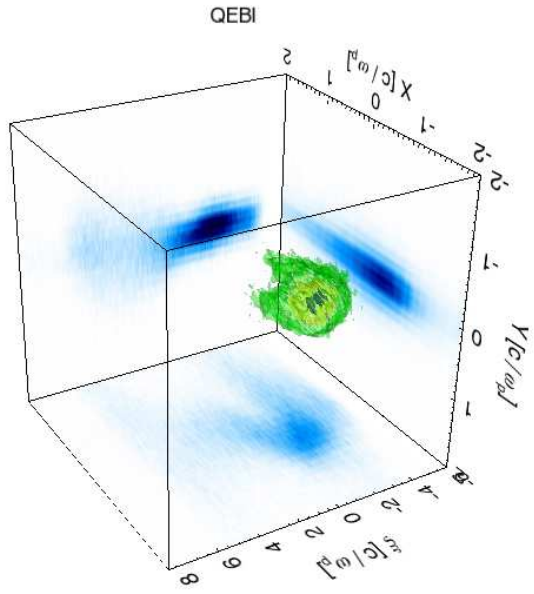

Figure 2.9: Density isosurface plots of an electron beam initially imported from the raw data of a SLAC beam. The plots (in blue) on the walls are projected density plots in three directions. The beam is moving to the right.

When studying the beam evolution in the PWFA, we are not only interested in the beam density but also the beam's phase space distribution. We directly dump the beam particles' raw data during the simulation and analyze then post-process the data. We use the parallel I/O libraries from the HDF5 package [63] in QuickPIC. When QuickPIC is running with multiple pipeline stages, only the beam particles belonging to the same stage are synchronized to the same time step. The beam particles belonging to different stages may be at different s steps. Therefore, when dumping the particles' raw data at a given s step, the first stage to reach that step will create a new file and all processors within that stage will

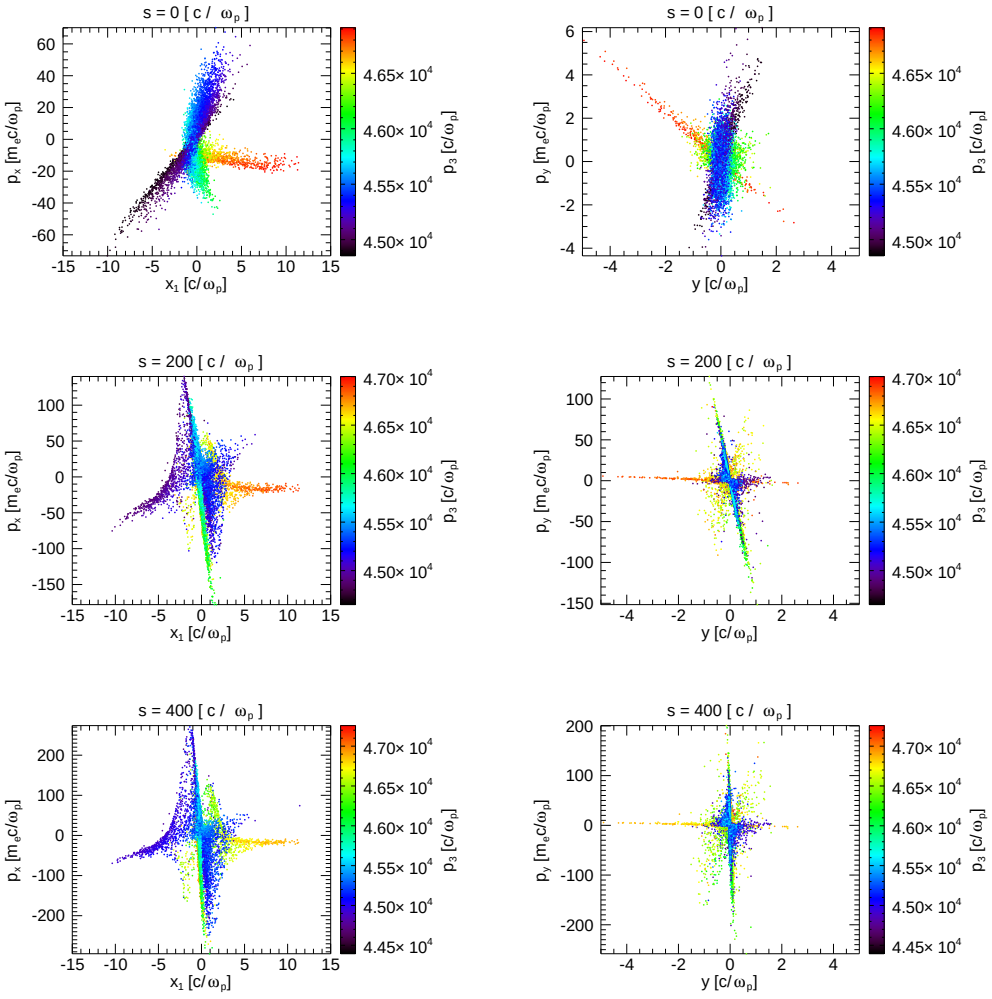

$x - p_x$ $y - p_y$

Figure 2.10: Snapshots of an electron drive beam phase space from a PWFA simulation.

dump the data (if there are any particles in this stage) into this file using parallel I/O. After the first stage in the pipeline finish writing the data, the next stage will open the file created by the first stage and all processors within the second stage write data into that file. If there are more stages, this process is repeated until the last stagehas written out data. As an example, Fig. 2.10 shows an electron beam phase space snapshots at different values of s as a beam propagates in a $5.0 \times 10^{16}\,\mathrm{cm}^{-3}$ plasma. The electron beam is the same as shown in the Fig. 2.9.

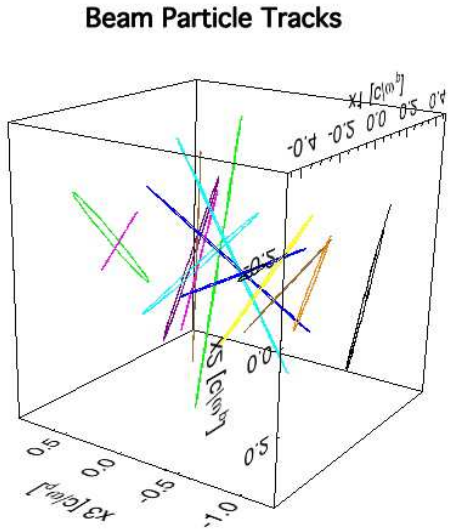

Figure 2.11: Illustration plot of the drive beam particles' trajectories in a PWFA.

Beam particle tracking is another useful diagnostic. This diagnostic allows us to obtain the trajectories $(x(s),\, y(s),\, \xi(s))$ of interested beam particles. It requires adding a tag on each beam particle. The tag is stored as an additional particle coordinate and is passed together with particle's position and velocity when the particle moves from one processor to another. Figure 2.11 shows the beam particle trajectories using the tracking diagnostic. The simulated case is an electron-beam-driven PWFA in the nonlinear regime. The beam parameters are $k_p\sigma_r = 0.2$, $k_p\sigma_z = 0.75$ and $n_b/n_p = 20$. Each line in Fig. 2.11 represents one beam particle's trajectory $(x_1(s),\, x_2(s),\, x_3(s))$, where $x_1 = x$, $x_2 = y$ and $x_3 = \xi$.

It shows that all the selected particles circulate in a closed elliptical orbits in the (x, y, ξ) space. Therefore these beam particles are doing simple harmonic oscillation in two transverse directions, which indicates that they all feel linear focusing force from the plasma wake field.

2.7 The plasma particle diagnostic and initialization

Similarly, we have implemented particle diagnostics for the plasma particles in QuickPIC. For a given s time step (i.e., the 3D step), the plasma raw data is stored at each ξ step allowing (x, y, p_x, p_y, p_z) phase space plots to be generated at each value of ξ. Figure 2.12 shows snapshots of the plasma electrons' phase space at different ξ positions. The simulated case is an electron-beam-driven PWFA in the nonlinear regime. The beam parameters are $k_p\sigma_r = 0.36$, $k_p\sigma_z = 1.08$ and $n_b/n_p = 6.86$. On top of the Fig. 2.12, there is a plasma and beam density plot showing a bubble-like nonlinear plasma wake driven by the intense electron beam with given parameters. Each snapshot of the plasma phase space is taken at different location of ξ ($\xi = 0, -1, -2, -3, -4, -5$). The snapshots show the process of the plasma electrons being first expelled by the drive beam and most of them finally being pulled back by the ion column.

In addition, the plasma particles can also be tagged so that the trajectories ($x(\xi)$, $y(\xi)$, $p_x(\xi)$, $p_y(\xi)$, $p_z(\xi)$) of interested plasma particles can be generated. We can also include the values of the wake fields the particles feel in the particle trackes. Figure 2.13 shows some plasma electron tracks (together with the drive beam isosurface) from the same simulation shown in Fig. 2.12. The selected plasma electrons initially stay in a line in the middle of the simulation box. The color of the track represents the energy (the Lorentz factor γ) of the plasma electron at different locations. We can see that the plasma electrons far away from the drive beam have small perturbations, which can be considered as linear

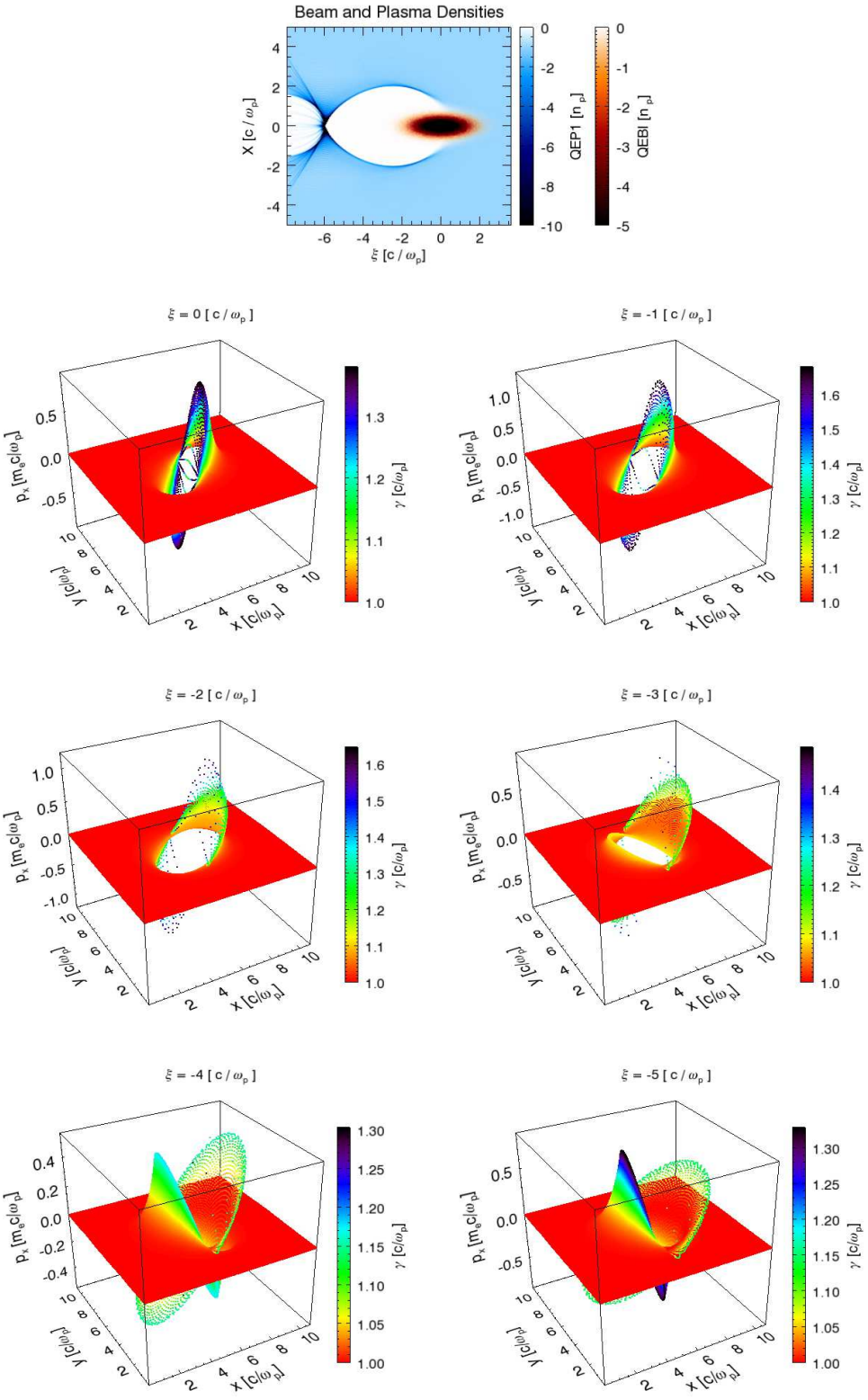

Figure 2.12: Snapshots of the plasma electrons' phase space from an electron-beam-driven PWFA simulation.

response, while the plasma electrons close to the drive beam feel large Coulomb field and are expelled to a large radius. Trajectory crossing happens for these electrons.

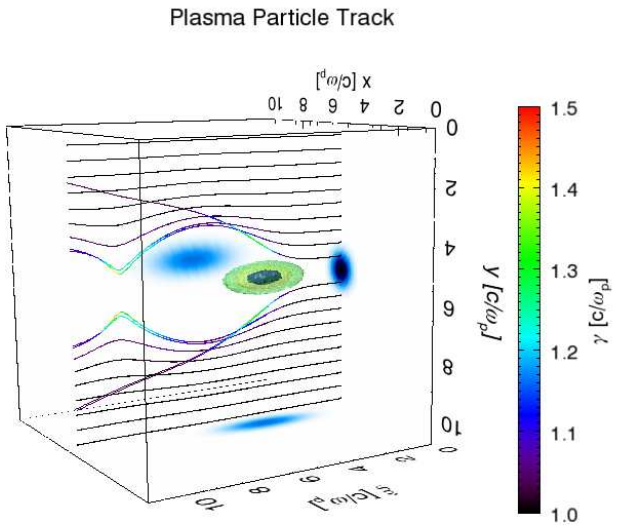

Figure 2.13: The trajectories of plasma electrons from an electron-beam-driven PWFA simulation.

Another important new feathur in QuickPIC 2.0 is the ability to initialize the plasma particles including the wake fields at a given ξ. In QuickPIC, the plasma particles are all stay in a two dimensional slice (with the same coordinate of ξ). They are advanced step by step along the ξ. After this plasma slice sweep over all the ξ steps in the simulation box, the drive beam will be pushed one step forward in s according to the fields obtained from the plasma response. Then all the procedures will start over with a re-initialized plasma slice at the very beginning position of ξ. At each s step, the plasma slice usually starts from the rest with a given transverse distribution profile (e.g. a uniform distribution) in front of the drive beam.

However, in some beam loading scenarios the trailing beam might evolve more

rapidly than the drive beam. If the drive beam is not evolving, we can initialize the plasma particles at a value of ξ behind it. The new plasma initialization allows us to start the plasma calculation from a certain ξ in the middle of the original simulation box. In order to do that, we need to first calculate the plasma response from the first $\xi = \xi_0$ position (where the plasma particles are in rest) and store the plasma particles information as well as the fields at the ξ position we want to start later. Then we can launch a new simulation, for which at each s step of we initialize the plasma particles and the fields with the same values at ξ_0. By using this plasma initialization method, we assume that everything does not evolve in s before the ξ we start from. This method can help us save much computing time on the non-evolving part and focus on what we really interested in. In chapter 4, this method is introduced in more details and used for studying the ion motion problem in a two-bunch PWFA.

2.8 Directions for future work

There are still several areas for developing numerical algorithms within QuickPIC in the future. One area is to compare and explore different options of using conservation laws for the motion of plasma particles. Within the quasi-static approximation, the quantity $\gamma - p_z = 1 - (q/m)\psi$ is a constant of the motion. This can be used in a variety of ways including comparing how well it is conserved between different choices in algorithms. It is necessary to obtain p_z and γ for both predicting the currents and fields and calculating the final momentum and position at the end of the iteration loop. One choice is to use the following equation

$$p_z = \frac{1 + p_\perp^2 - (1 - (q/m)\psi)^2 + a^2/2}{2(1 - (q/m)\psi)},$$

which is derived by combining the constant motion with the quasi-static definition for γ, which is $\gamma^2 = 1 + p_\perp^2 + p_z^2 + a^2/2$. This equation is used in both WAKE and QuickPIC. It involves the pseudo potential ψ, the particle position $\vec{x}_\perp$ (for

interpolating ψ) and the particle momentum $\vec{p}_\perp$, which all should be known at the same ξ. The second choice is to calculate p_z using the constant of the motion within the iteration loop to obtain J_z at the half step (using a predicted $\vec{p}_\perp$) but to calculate p_z at the next full step using the equation of motion,

$$\frac{dp_z}{d\xi} = \frac{q/m}{1-(q/m)\psi}\left[\gamma E_z + \vec{p}_\perp \times \vec{B}_\perp\right],$$

at the end of the iteration loop. Note that we have used the constant of motion in the above equation. This is what is currently done in QuickPIC 2.0. Another choice would be to use the equation of motion for both a half step to predict p_z within the iteration loop and a full step at the end of the iteration loop. We have experimented with all of these choices but have not carefully compared the results to see which ultimately maintains the constant of the motion best within or after the iteration loop. So this will be an area for our future work.

There are also two choices for updating the particle's position. One choice is to use the following equation as was done in QuickPIC 1.0 [48]

$$\frac{d\vec{x}_\perp}{d\xi} = \frac{\vec{p}_\perp}{1-(q/m)\psi}.$$

In order for this equation to be time centered, ψ and $\vec{p}_\perp$ need to be defined at the same ξ . This means we need to calculate the ψ at both full and half integer time steps (see Table 2.1). This requires calculating ψ and interpolating ψ at each particle position at least twice during each iteration loop which also leads to additional parallel communication between each processors.

The other choice, which we use in QuickPIC 2.0, is to use the equation

$$\frac{d\vec{x}_\perp}{d\xi} = \frac{\vec{p}_\perp}{\gamma - p_z}.$$

This requires that we know p_z at the same ξ as $\vec{p}_\perp$ (and hence know γ at the same ξ). The correct time centering is kept if we calculate p_z using the equation of motion at the end of the iteration loop and we do not need to update the particle

position within the iteration loop. This method does not rely on the constant of the motion directly. Exploring how well the constant of the motion as maintained between these two choices is also an area for our future work.

Other areas for the future work include incorporating the laser solver and ponderomotive guiding center force into QuickPIC 2.0 with its new algorithm for the iteration loop, developing a recipe for determining when a plasma particle is trapped and become a beam-like particle, implementing adaptive 2D and 3D time steps, experimenting with load balancing in the 2D part of the code, porting the code to GPUs, mesh refinement, and experimenting with using a $\vec{k}_\perp$ dependent coefficient in front of the $\vec{B}_\perp^{new}$ and $\vec{B}_\perp^{old}$ terms in equation (2.20).

2.9 Summary

In this chapter, we have described a new field solver for a fully three-dimensional quasi-static PIC code. This solver is used in QuickPIC. Instead of calculating the scalar and vector potentials using the Lorentz gauge to obtain the electromagnetic fields, we solve for the electromagnetic field directly (these equations are therefore gauge invariant) using the appropriate charge and current densities. In addition, a new deposition scheme for the time derivative of the current density is implemented in QuickPIC. The new method can locally deposit the $\partial\vec{J}_\perp/\partial\xi$ without updating and repartitioning the particles two times during each iteration loop. By simulating many different scenarios of beam driven PWFA, we show that results from the new QuickPIC, QuickPIC 2.0, are in excellent agreement from the full PIC code OSIRIS after only 1 iteration in the most cases, while the old QuickPIC, QuickPIC 1.0, typically requires at least 4 iterations to obtain the same results. For a typical nonlinear PWFA simulation used for timing results, QuickPIC 2.0 is 5 to 8.5 times faster than QuickPIC 1.0 version depending on the number of particles per cell. A new field ionization module in QuickPIC 2.0 is

introduced, which allows us to simulate gas species with multiple ionization levels. Other improvements to QuickPIC 2.0 are also presented, including the beam and plasma initialization and diagnostic routines.

CHAPTER 3

Two-Bunch PWFA

Earlier experiments at the final focus test beam (FFTB) facility at the Stanford Linear Accelerator Center (SLAC) [28] have shown that a PWFA can sustain an accelerating gradient exceeding 50 GeV/m over almost a meter long distance. The large-amplitude plasma wave or wake was excited by a high energy electron beam operating in the so-called "blow-out" regime [64, 16], where the electron beam density n_b is much larger than the plasma density n_p or the beam current exceeds a few 10's of kA. The plasma was formed in these experiments by ionizing a column of lithium (Li) using the transverse electric field E_r of the 42 GeV electron bunch [65]. When the high energy electron bunch (the drive beam) travels through the neutral gas, the E_r field of the beam ionizes the neutral gas into the plasma state. If $n_b > n_p$ (or if the beam current exceeds 10's of kAs), it expels all the plasma electrons within a certain radius of the bunch thereby creating an ion cavity (resembling a bubble) around the beam. The expelled plasma electrons form a sheath around this ion cavity and are pulled back to the axis at the rear part of the bubble by the restoring force exerted by the plasma ions, thereby forming a classic wake field configuration. This highly-nonlinear plasma wake contains both a transverse focusing field (which increases linearly away from the axis with the transverse distance r) and a longitudinal accelerating field (which is uniform in the transverse direction), which are ideal conditions for accelerating an electron beam. The amplitude of the longitudinal electric field in such a nonlinear plasma wake can be on the order of $m_e c\omega_p/e \approx 10[\mathrm{GV/m}]\sqrt{n_p/10^{16}[\mathrm{cm}^{-3}]}$, where n_p is

the plasma density and ω_p is the plasma frequency [66]. In the experiments at the FFTB, only a single electron bunch was used. Electrons in the head of the beam created the plasma and excited the wake. Electrons in the tail of the beam were accelerated. Since they resided in all phases of the wave, there was a large energy spread ($\sim$100%) on the accelerated electrons. Furthermore, in this experiment the acceleration distance was limited by ionization-induced beam head erosion. The very head of the beam is not guided by any plasma focusing fields. Therefore, it expands as in vacuum, and the self-fields of the beam head get smaller causing the ionization front to slip backwards and leading to more electrons in the bunch to expand.

At FACET, a primary focus will be demonstrating that good beam quality can be maintained if a second electron bunch is properly placed in the wake created by a first bunch (drive beam). While the drive beam transfers its energy to the wake, a second electron bunch (the trailing beam) can be placed at an appropriate distance behind the drive beam, i.e., in the accelerating field of the wake, to gains energy. If the trailing beam contains a sufficient number of electrons it can load the wake and flatten the accelerating field [67] so that all the electrons gain energy at nearly the same rate, thus minimizing the energy spread of the beam and increasing the energy extraction efficiency. Such a "two-bunch" PWFA scenario will be tested on the newly completed facility FACET at SLAC [31].

In this chapter, several important issues related to the two-bunch PWFA will be discussed. In section 3.1, we will review the electron-beam-driven plasma wake in the nonlinear regime. In section 3.2, we will discuss the decelerating field in an electron-beam-driven nonlinear plasma wake. In section 3.3, we discuss how to find the optimal plasma density to excite largest accelerating field for a given beam parameters. Simulations of two-bunch PWFA experiments at FACET are shown in 3.4. In section 3.5, the drive beam head erosion in the two-bunch experiments and the methods for mitigating head erosion in the field ionized plasma will be

discussed. Lastly, we summarize the chapter in section 3.6.

3.1 The electron-beam-driven nonlinear plasma wake field

A high energy electron beam (the drive beam) can excite a nonlinear plasma wake when the space charge forces of this beam are strong enough to expel all the plasma electrons within a radius greater than or equal to the plasma skin depth. This results in a bubble-like cavity around the drive beam filled with only ions. The expelled plasma electrons flow backwards in a thin sheath around the ion cavity which are eventually pulled back to the axis by the ions (Fig. 3.1).

A theory based on the quasi-static approximation (this was described in the last chapter) was developed to analytically describe the wake field in this blow-out regime [16, 17]. The theory assumes the drive beam has an axisymmetric profile and does not evolve as it propagates through the plasma. It is shown in references [16] and [17] that inside the bubble, the pseudo potential (recall this is $\psi \equiv \phi - A_z$) has a solution

$$\psi(r,\xi) = \frac{r_b^2(\xi)}{4}(1+\beta(\xi)) - \frac{r^2}{4}, \tag{3.1}$$

where $r_b(\xi)$ is the bubble radius at ξ and $\beta(\xi)$ is a parameter related to the width of the sheath Δ around the bubble. The formula for $\beta(\xi)$ is

$$\beta(\xi) = \frac{(1+\alpha)^2 \ln(1+\alpha)^2}{(1+\alpha)^2 - 1} - 1,$$

where $\alpha \equiv \dfrac{\Delta}{r_b(\xi)}$. The solution of ψ is derived by solving the equation (2.1) directly. It also assumes that $\rho - J_z$ (which is conserved at each slice of ξ, i.e., $\displaystyle\int_0^\infty dr\, r(\rho - J_z) = 0$) is equal to 1 for $r < r_b$ and is a constant within the sheath around the bubble (where $r_b < r < r_b + \Delta$, Δ is the sheath width) and is equal to 0 outside the sheath. This assumption gives a very good agreement with the simulation. Note that the existence of the high energy beam inside the bubble will not change the profile of $\rho - J_z$ and hence not change the form of the solution of ψ,

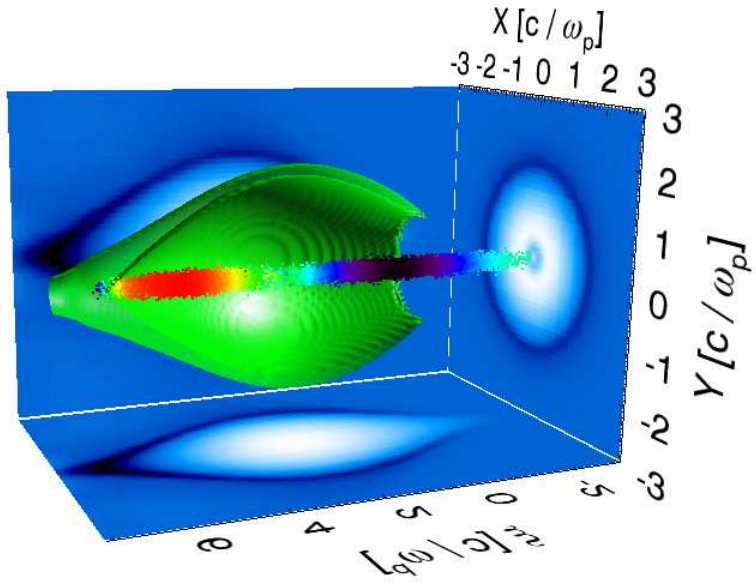

Figure 3.1: Plot from a QuickPIC simulation of a two-bunch PWFA in the "Blow-Out" regime. This plot is a combination of (a) A projection of the plasma electron density (three blue plots on the walls) along the x, y and ξ axes, (b) three dimensional isosurface of the plasma electron density (green surfaces which stand for the inside and outside surfaces of the plasma electron sheath around the bubble) and (c) the beam particles (plotted as colored dots: blue represents low energy and red represents high energy). The two bunches are moving from the left to the right.

because for any beam moving at the speed close to c, the beam's $\rho - J_z$ equals to $\sim$zero. But the beam will influence the bubble radius $r_b(\xi)$ and therefore influence ψ indirectly. In references [16] and [17], it is shown that $r_b(\xi)$ obeys the equation,

$$A(r_b)\frac{d^2 r_b}{d\xi^2} + B(r_b) r_b (\frac{dr_b}{d\xi})^2 + C(r_b) r_b = \frac{\lambda(\xi)}{r_b}, \tag{3.2}$$

where

$$\begin{aligned} A(r_b) &= 1 + [\frac{1}{4} + \frac{\beta}{2} + \frac{1}{8} r_b \frac{d\beta}{dr_b}] r_b^2, \\ B(r_b) &= \frac{1}{2} + \frac{3\beta}{4} + \frac{3}{4} r_b \frac{d\beta}{dr_b} + \frac{1}{8} r_b^2 \frac{d^2\beta}{dr_b^2}, \\ C(r_b) &= \frac{1}{4}[1 + \frac{1}{(1 + \frac{\beta}{4} r_b^2)^2}], \end{aligned}$$

and $\lambda(\xi) = \int_0^{r \gg \sigma_r} r n_b dr$ is the total beam charge per unit length. This equation together with the equation for ψ constitutes a complete analytical model for the nonlinear plasma wake driven by an electron beam.

By assuming the beam particles move at the speed of light, we can separate the transverse motion and the longitudinal motion of the beam. In the transverse direction, the particle's equation of motion is

$$\frac{d\vec{p}_\perp}{dt} = \frac{q}{m}(\vec{E}_\perp + \vec{v}_\perp \times B_z \hat{z} + v_z \hat{z} \times \vec{B}_\perp).$$

Because $|\vec{v}_\perp| \ll v_z = 1$, the above equation becomes

$$\frac{d\vec{p}_\perp}{dt} = \frac{q}{m}(\vec{E}_\perp + \hat{z} \times \vec{B}_\perp).$$

In the longitudinal direction,

$$\frac{dp_z}{dt} = \frac{q}{m}(E_z + \vec{v}_\perp \times \vec{B}_\perp) \approx \frac{q}{m} E_z.$$

Therefore, both the transverse and longitudinal motion of a beam particle behaves like a particle moving in the pseudo potential field. In the transverse direction, $\vec{E}_\perp + \hat{z} \times \vec{B}_\perp = -\nabla_\perp \psi$ (which is equation (2.14)) while in the longitudinal direction

$E_z = \partial\psi/\partial\xi$ (which is equation (2.3)). If we take the derivative of ξ on the transverse field, we can get

$$\frac{\partial}{\partial\xi}\left(\vec{E}_\perp + \hat{z}\times\vec{B}_\perp\right) = -\frac{\partial}{\partial\xi}\nabla_\perp\psi = -\nabla_\perp\left(\frac{\partial}{\partial\xi}\psi\right) = -\nabla_\perp E_z. \tag{3.3}$$

Therefore the dependency between the transverse field and the longitudinal field is shown in the following equation

$$\frac{\partial}{\partial\xi}\left(\vec{E}_\perp + \hat{z}\times\vec{B}_\perp\right) = -\nabla_\perp E_z, \tag{3.4}$$

which is called the Panofsky-Wenzel theorem [68].

Note that in the azimuthal symmetric system, the transverse field becomes $E_r - B_\theta = -\partial\psi/\partial r$. By combining this with equation (3.1), we can find that the transverse field (inside the bubble) felt by the beam particle is

$$E_r - B_\theta = -\partial\psi(r,\xi)/\partial r = r/2,$$

and the longitudinal field felt by the beam particle is

$$E_z = \partial\psi(r,\xi)/\partial\xi = \partial\psi(0,\xi)/\partial\xi,$$

where $\psi(0,\xi) = \frac{r_b^2(\xi)}{4}(1+\beta(\xi))$. These fields are favorable for accelerating electron beams, since the transverse field is a focusing force for electrons and it is longitudinally uniform (does not depend on ξ) and radially linear, which means that when the electron beam is accelerated inside the bubble the transverse emittance of the beam at every slice along ξ can be conserved. On the other hand, the longitudinal field is transversely uniform (does not depend on r), which means the transverse motion of beam particles will not lead to any energy spread. However, an energy spread can still arise due to the non-uniformity of E_z along the longitudinal direction. A locally uniform accelerating field can nevertheless be obtained if we load a second electron beam (which has a proper beam current) appropriately inside the plasma wake of the first beam (which is the beam loading effect and will be discussed in the next section). Figures 3.2 and 3.3 show QuickPIC simulation

results of a PWFA case in the bubble regime, which illustrates the properties of the fields within the bubble wake. In the simulation, the drive beam contains $N = 3.0 \times 10^{10}$ electrons. It has a Gaussian profile and the r.m.s. spot size of the beam is $\sigma_r = 10\,\mu$m. The r.m.s. pulse length of the beam is $\sigma_z = 30.0\,\mu$m. There is also a trailing beam that contains $N = 1.0 \times 10^{10}$ electrons. The r.m.s. spot size of this beam is $\sigma_r = 10\,\mu$m. The r.m.s. pulse length of the beam is $\sigma_z = 10.0\,\mu$m. The distance between two beams' centers is $115\,\mu$m. Both two beams have an initial energy of 23 GeV.

Both Fig. 3.2(b) and 3.3(a) show that E_z is uniform in the transverse direction within the bubble (where $r < r_b$) and this property is not affected when the wake is loaded. Therefore, by knowing the on-axis lineout of E_z (the red line in Fig. 3.2(b)), we knowl the E_z everywhere within the bubble. Note that due to the beam loading effect mentioned before, there is a flat region of E_z where the trailing beam is located. Figure 3.2(c) shows that $E_r - B_\theta$ is uniform along ξ within the bubble and it is still true when the wake is loaded by a second beam. Figure 3.3(b) shows that $E_r - B_\theta$ is equal to $r/2$ inside the bubble, which is a perfect focusing force for electron beams to maintain their normailzed emittance. For an axisymmetric drive beam, $E_r - B_\theta$ does not change within the bubble plasma wake unless the ion motion occurs under extreme beam conditions. This will be discussed in the next chapter.

3.2 The decelerating field in a nonlinear electron-beam-driven PWFA

When the plasma ions are fixed (which is a reasonable assumption when the duration of the interaction between the plasma ion and the particle beam is very short and/or the Coulomb field around the particle beam is not very strong) and the drive beam is axisymmetric, the focusing force $E_r - B_\theta$ on the drive beam

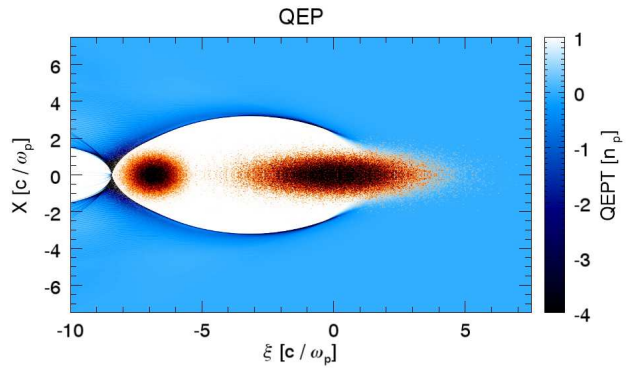

(a)

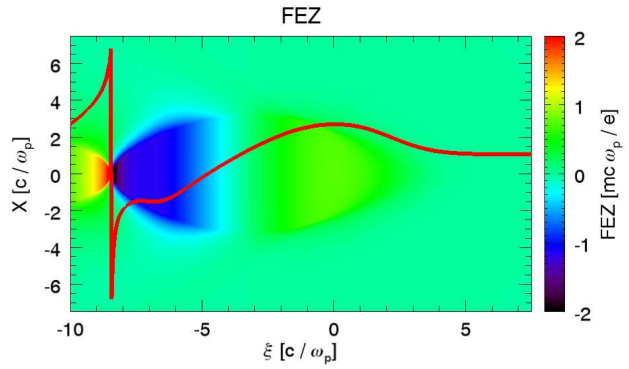

(b)

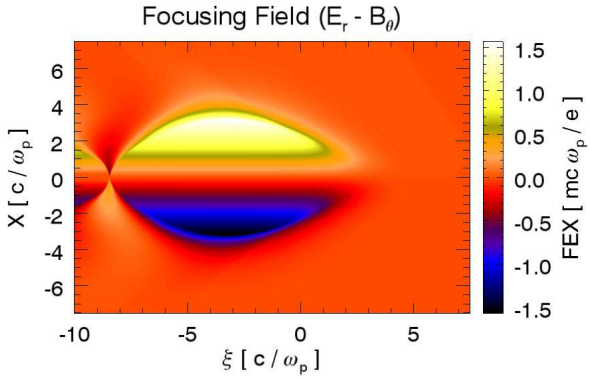

(c)

Figure 3.2: Nonlinear plasma wakefields with two electron beams. (a) Plasma density (in blue) and beams densities (in brown); (b) E_z slice plot across the center of the simulation box. The red line is the on-axis lineout of E_z. (c) Focusing field ($E_r - B_\theta$) slice plot across the center of the simulation box. The two bunches are moving from left to the right.

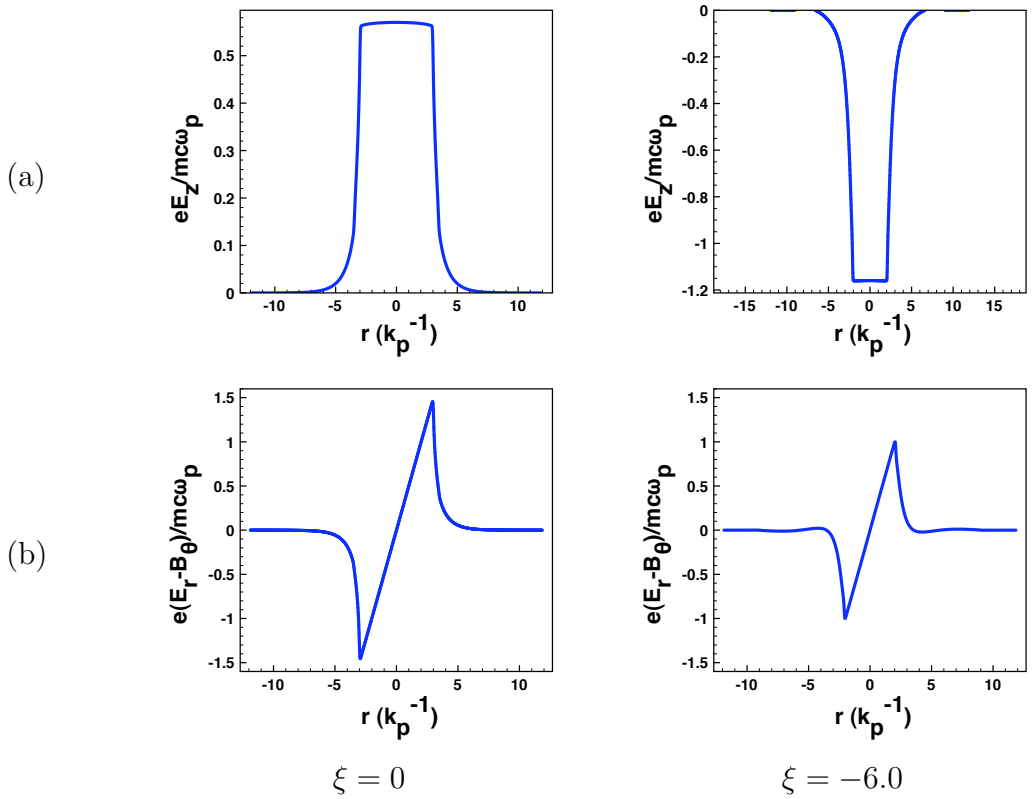

Figure 3.3: Lineouts of the fields shown in Fig. 3.2: (a) The lineout of E_z at two different ξ slices;(b) The The lineout of $E_r - B_\theta$ at two different ξ slices.

is equal to $r/2$ inside the bubble. The electrons of the drive beam will oscillate laterally (i.e., execute betatron oscillation). However, the E_z field of the plasma wake will change the drive beam's energy. From energy conservation, if the drive beam is creating a wake then it must be losing energy. As seen in the Fig. 3.2(b), E_z does indeed provide a decelerating field (positive value) for the electron drive beam as well as an accelerating field (negative value) for a trailing beam that is properly placed. And we can manipulate E_z on the trailing beam by changing the beam(s) density profile(s) $\lambda(\xi)$. In this section, we use QuickPIC simulations to show how the decelerating field in a nonlinear plasma wake changes as the drive beam (with a Gaussian profile) parameters are changed.

We begin by discussing the beam's spot size influence on the nonlinear plasma

wake. Equation (3.2) indicates that the bubble radius $r_b(\xi)$ only depends on $\lambda(\xi)$, which does not depend on the beam spot size σ_r. Therefore, $E_z = \partial\psi(0,\xi)/\partial\xi$ (where $\psi(0,\xi) = \frac{r_b^2(\xi)}{4}(1+\beta(\xi))$) does not depend on σ_r either. This is based on the assumption that σ_r is much smaller than r_b. However, the plasma wake may either have a r_b smaller than σ_r or not have a totally blow-out region at the front part of the beam's rising edge, in which case the assumptions used to obtain $\psi(0,\xi)$ are not valid. This may result in different $r_b(\xi)$ solutions to equation (3.2) since the initial evolution of $r_b(\xi)$ and $dr_b(\xi)/d\xi$ will depend on the σ_r of the drive beam. Figure 3.4 shows QuickPIC simulation results of E_z on-axis lineouts in the nonlinear plasma wakes driven by the electron beams with the same $\lambda(\xi)$ but different spot sizes. The plasma density is $1.0 \times 10^{17}\,\mathrm{cm}^{-3}$. The drive beam has $N = 1.8 \times 10^{10}$ electrons. It has a Gaussian profile and the r.m.s. pulse length of the beam is $\sigma_z = 30.0\,\mu\mathrm{m}$ ($k_p\sigma_z$=1.78).

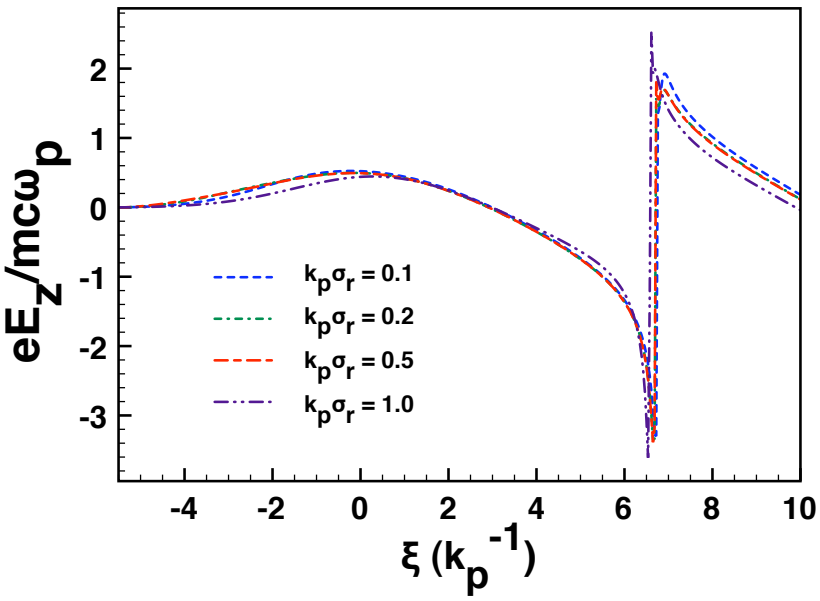

Figure 3.4: E_z on-axis lineouts of the nonlinear plasma wake driven by the electron beams with different spot sizes.

From Fig. 3.4, we can see that E_z does not change much when $k_p\sigma_r < 0.5$.

Note that in obtaining the simulation results of Fig. 3.4 we used a non-evolving drive beam. Normally when the initial normalized beam spot size $k_p\sigma_r > 1.0$, the transverse profile of beam's rising edge (i.e., the beam head) will change and finally converge to a new profile during the beam propagating in the plasma because the focusing force at the beam head is not linear in r, i.e., proportional to $r/2$. The beam head's modification inside the plasma will lead to a perturbation of the plasma wake, which we usually want to avoid. This perturbation can be negligible when the initial beam spot size is small (or the initial beam emittance is very small). For practical reasons, we will look at the E_z field of the plasma wake exited by a non-evolving electron drive beam, which has a fixed normalized beam spot size $k_p\sigma_r = 0.1$ but different normalized charge per unit length Λ ($\Lambda = (n_b/n_p)k_p^2\sigma_r^2$ is the peak value of $\lambda(\xi)$) and different $k_p\sigma_z$. Note that although Λ is a dimensionless quantity in which n_b is normalized to n_p, it does not depend on n_p due to the k_p^{-2} term, i.e., $\Lambda = (n_b/n_p)k_p^2\sigma_r^2 = 2.242\times10^{-13}N/\sigma_z[\text{cm}]$ for a Gaussian profile beam, where N is the beam particle number. So for fixed beam parameters, Λ does not change if the beam propagates in plasma with different plasma densities, while $k_p\sigma_r$ and $k_p\sigma_z$ will change when the plasma density changes.

Figure 3.5 shows QuickPIC simulation results of the normalized peak decelerating field for an electron-beam-driven nonlinear plasma wake versus the normalized beam pulse length. In each case, the drive beam has a Gaussian density profile. As mentioned before, the drive beam has a fixed normalized spot size $k_p\sigma_r = 0.1$, and its normalized pulse length $k_p\sigma_z$ varies from 1 to 6. Each line in the plot has the same Λ for the drive beam, and the Λ varies from 1 to 5. Note that the scales of $k_p\sigma_z$ and Λ in this plot can cover almost all of the current and future electron beams that can be used in PWFA experiments. From Fig. 3.5 we can see that with the same beam Λ, the peak normalized decelerating field E_z gets smaller when the drive beam's pulse length increases while with the same beam

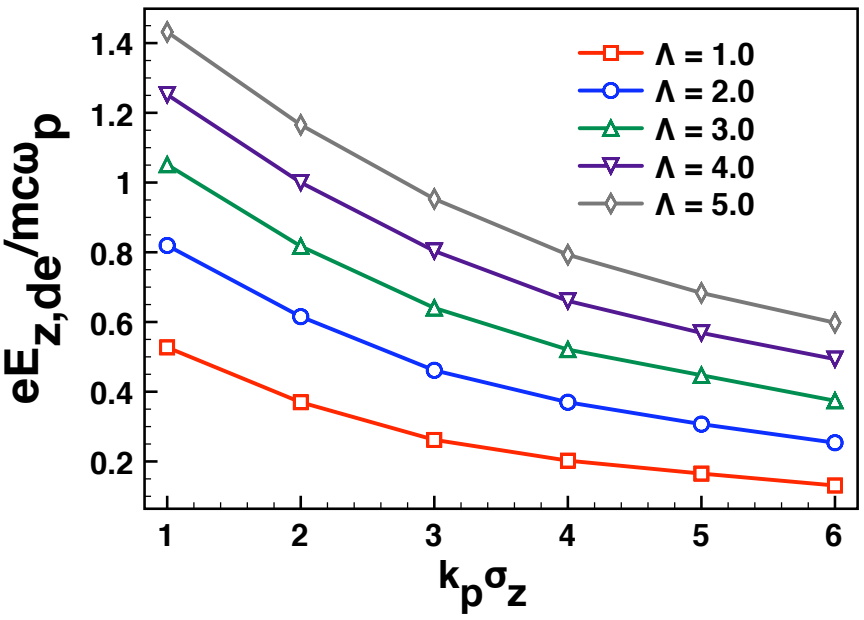

Figure 3.5: Peak decelerating field in the electron-beam-driven nonlinear plasma wake with different beam normalized pulse length and Λ.

pulse length, the peak decelerating field will increase as the beam's Λ increases. The peak decelerating field can be used to calculate the beam's pump depletion length L_d in the plasma, which is $k_p L_d = \gamma / E_{z,de}$ for the electron drive beam, where γ is the initial Lorentz factor of the electron beam. For example, for a 20 GeV electron beam ($\gamma = 40,000$) with $\Lambda = 2$ and $k_p \sigma_z = 1$, the normalized peak decelerating field is around 0.82. The normalized pump depletion length of this beam is therefore $k_p L_d = 40000/0.82 = 4.88 \times 10^4$, which is around 82 cm in a $1.0 \times 10^{17}\,\mathrm{cm}^{-3}$ plasma. For an arbitrary beam pulse length and beam Λ, we can estimate the peak decelerating field through simple linear interpolation according to the data shown in Fig. 3.5.

We can also make a rough estimation of the peak decelerating field by using the equation $E_{z,de} = \Lambda / \sqrt{e} k_p \sigma_z$ [69]. To obtain this result, we should first look at the plasma wake field driven by an electron beam with a linear ramped profile, $\lambda(\xi) = \dfrac{\Lambda_0}{L_0}\xi$, $0 < \xi < L_0$. In the relativistic blow-out regime, where the maximum

blow-out radius $k_p r_{b,max} \gg 1$, the pseudo-potential of the plasma wake becomes

$$\psi(r,\xi) = \frac{r_b^2(\xi)}{4} - \frac{r^2}{4}, \tag{3.5}$$

where we neglect the term $\beta(\xi)$ in equation (3.1) because it becomes much less than 1 in this case. The longitudinal electric field will then be,

$$E_z = \partial\psi(r,\xi)/\partial\xi = \partial\psi(0,\xi)/\partial\xi = \frac{1}{2} r_b \frac{dr_b}{d\xi}. \tag{3.6}$$

The equation of the blow-out radius r_b, equation (3.2), will then reduce to

$$r_b \frac{d^2 r_b}{d\xi^2} + 2(\frac{dr_b}{d\xi})^2 + 1 = \frac{4\lambda(\xi)}{r_b^2}. \tag{3.7}$$

For a linear ramped beam profile, $\lambda(\xi) = \frac{\Lambda_0}{L_0}\xi$, $0 < \xi < L_0$, equation (3.7) has an exact solution,

$$r_b(\xi) = 2\sqrt{\frac{\Lambda_0}{L_0}(\xi - \frac{\Lambda_0}{L_0})},$$

when $\xi > \frac{\Lambda_0}{L_0}$. By substituting this solution into the equation for E_z (equation (3.6)), we then have

$$E_z = \Lambda_0/L_0, \; \frac{\Lambda_0}{L_0} < \xi < L_0,$$

which is the decelerating field felt by the linear ramped beam. For a Gaussian beam profile, the rising edge of the beam can be approximated as a linear ramp with $L_0 = \sqrt{e} k_p \sigma_z$. If we assume the decelerating field reaches its maximum value at the center of the beam, then the peak decelerating field for a Gaussian beam is $E_{z,de} \approx \Lambda/\sqrt{e} k_p \sigma_z$, where Λ is the peak value of the Gaussian beam. To validate this approximation, we multiply the $E_{z,de}$ in Fig. 3.5 by $\sqrt{e} k_p \sigma_z$ at each point and plot them in Fig. 3.6. If the approximation is reasonable then $\sqrt{e} k_p \sigma_z E_{z,de}$ will be constant for each value of Λ. We can see that for a range $k_p \sigma_z$ (between the two yellow dashed lines) the equation $E_{z,de} = \Lambda/\sqrt{e} k_p \sigma_z$ is satisfied. The range of $k_p \sigma_z$ between the yellow lines gets smaller as Λ increases.

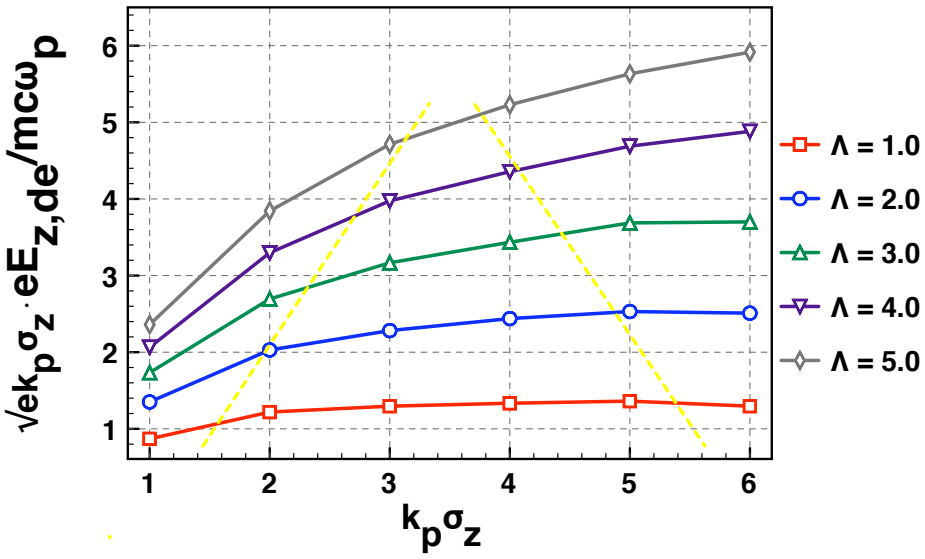

Figure 3.6: Product of peak decelerating field and $\sqrt{e}k_p\sigma_z$ with different beam normalized pulse length and Λ.

3.3 The optimum plasma density for achieving the largest accelerating field in a nonlinear PWFA

As shown in Fig. 3.2(b), E_z of the plasma wake field can also provide an accelerating field (negative value) for electrons in the rear of the bubble. It can be used to accelerate either a trailing beam or the tail of the drive beam. In figure 3.5, we showed how the normalized field varied with Λ and $k_p\sigma_z$ (two other normalized quantities). A simple but fundamental question regarding the accelerating field is: For a given absolute (not normalized) electron beam parameters (e.g. the total number of beam particles N , the beam spot size σ_r, the pulse length σ_z, the beam energy γ and the normalized beam emittance ϵ_N), what is the optimum plasma density that provides the largest absolute accelerating field? We start from the linear theory for determining the optimum density. In linear theory, the density compressions and rarefactions of the wave are assumed to be small compared to the background plasma density n_p and a rough condition for this is that the beam

density is small $n_b \ll n_p$. The limitations and usefulness of the linear theory can be found in the reference [70]. We begin with the expression of the absolute wakefield amplitude E_{z0} (not normalized) for a Gaussian drive beam

$$E_{z0} = \sqrt{2\pi}\frac{m_e c^2}{e}\frac{n_{b0}}{n_p}k_p^2\sigma_z \exp(-k_p^2\sigma_z^2/2)R(0), \tag{3.8}$$

where $R(0) = (k_p^2\sigma_r^2/2)\exp(k_p^2\sigma_z^2/2)\Gamma(k_p^2\sigma_z^2/2), \Gamma(y) = \int_y^\infty t^{-1}e^{-t}dt$ and the drive beam density is $n_b = n_{b0}\exp[-(z^2/2\sigma_z^2) - (r^2/2\sigma_r^2)]$.

Next, we find the plasma density that maximizes the absolute wakefield amplitude. At this point, it is important to be clear about what is being held fixed. For example, in the one dimensional (1D) or the wide beam limit ($k_p\sigma_r \gg 1$), if we assume that n_{b0}/n_p and σ_z are fixed, the absolute wakefield E_{z0} is maximized for $k_p\sigma_z = \sqrt{2}$ or $n_o\,[\mathrm{cm}^{-3}] = 5.6\times10^{19}/\sigma_z^2[\mu\mathrm{m}]$. On the other hand (as shown below), if we assume that the beam particle number N as well as σ_r and σ_z remain fixed, then for $\sigma_r \gg \sigma_z$ the absolute wakefield is instead maximized for $k_p\sqrt{\sigma_r\sigma_z} = \sqrt{2}$ or equivalently $k_p\sigma_z = \sqrt{2\sigma_z/\sigma_r} \ll \sqrt{2}$.

Next, we will assume the beam parameters are fixed and only the plasma density varies. This is usually the situation of relevance when designing an accelerator. For this situation it is useful to explicitly write out n_{b0} as $n_{b0} = N/[(2\pi)^{3/2}\sigma_r^2\sigma_z]$. Equation (3.8) now becomes

$$E_{z0} = ek_p^2 N \exp -(k_p^2/2)[\sigma_z^2 - \sigma_r^2]\Gamma(k_p^2\sigma_r^2/2). \tag{3.9}$$

In the reference [70], it was shown that when optimizing E_{z0} as a function of k_p^2, i.e., n_p, the optimized wakefield amplitude E_{zM} can be written as

$$E_{zM} = \frac{eN}{\sigma_r\sigma_z}\Theta\left(\frac{\sigma_r}{\sigma_z}\right), \tag{3.10}$$

and the universal function Θ was plotted in figure 2 of [70]. It is straightforward to obtain asymptotic expressions for k_p that optimizes E_{z0} in the $\sigma_r/\sigma_z \ll 1$ and $\sigma_r/\sigma_z \gg 1$ limits. When $\sigma_r/\sigma_z \ll 1$, we call the bunch shape a cigar. In

the opposite limit where $\sigma_r/\sigma_z \gg 1$ we call the bunch shape a pancake. In the cigar limit, one can obtain $k_p\sigma_z \approx \sqrt{2}[1-(1/\ln(2/k_p^2\sigma_r^2))]^{1/2}$ which is essentially $k_p\sigma_z = \sqrt{2}$ for $k_p\sigma_r \ll 1$. Interestingly although the limits are very different, for both the 1D limit ($k_p\sigma_r \gg 1$) when n_{b0}/n_p and σ_z are held fixed and the narrow ($\sigma_r \ll \sigma_z$) 3D limit where N, σ_r and σ_z are held fixed, the optimum density is $n_o\,[\mathrm{cm}^{-3}] = 5.6\times 10^{17}/\sigma_z^2[10\,\mu\mathrm{m}]$. In the pancake limit, where $k_p^2\sigma_r^2 \gg 1$ and $\Gamma(y) \sim ((1/y)+(1/y^2)+\cdots)e^{-y}$, one can easily show that the density which optimizes E_{z0} corresponds to $k_p = \sqrt{2/(\sigma_r\sigma_z)}$ or $k_p\sigma_z = \sqrt{2\sigma_z\sigma_r)} \ll \sqrt{2}$. To determine the optimum density for beams with $\sigma_r \approx \sigma_z$, one can refer to figure 2 in [70], where for a round beam $k_p\sigma_z \approx 0.9$.

While linear theory provides a useful starting point, its assumptions fail for most current and planned PWFA experiments, such as those at FACET. As shown in the reference [70], even if the assumptions fail the expressions for the wake amplitude can still be useful. The figure of merit to determine if the results from linear theory are valid is the normalized charge per unit length of the beam $\Lambda = 2I_p/I_A$, where I_p is the peak current of the beam and $I_A \approx 17\,kA$ is the Alfven current. For $k_p\sigma_r < \sqrt{\Lambda}$, i.e., $n_{b0}/n_p > 1$, the wakes are excited in a highly nonlinear multi-dimensional regime (the blowout regime) for which linear theory is invalid.

To illustrate the usefulness and the limitation of the linear prediction, we show two examples based on the parameters of PWFA experiments done on FFTB at SLAC, and on the parameters available at FACET. In one of the examples, although $n_b/n_p \gg 1$ (so linear theory should not apply), the quantity $\Lambda \ll 1$ and the prediction from linear theory remains useful. For the other example, $\Lambda \geq 1$ and the prediction for the optimum density from linear theory is actually off by a factor of ten.

At SLAC, the electron bunches typically have a total number of electrons $N \approx 2\times 10^{10}$, which is around 3 nC of charge. The beams can be focused

down to a few tens of microns by beam focusing optics. The pulse duration can be varied from ps down to 50 fs through a three-stage bunch compression method. The first example corresponds to the E157 experiment on FFTB at SLAC, where $N = 1.9 \times 10^{10}$, $\sigma_z = 700\mu$m and $n_{b0} = 1.9 \times 10^{15}\text{cm}^{-3}$. For these parameters, $\Lambda \approx 0.06$ and the linear theory predicts the optimum plasma density is $n_o \approx 1.15 \times 10^{14}\,\text{cm}^{-3}$. For this density, the peak beam density n_{b0} is about 17 times higher than the plasma density, which suggests that the nonlinear blowout regime is indeed reached. This can be easily seen in Figure 3.7(a), where the beam and plasma densities are plotted for $n_p = 1.15 \times 10^{14}\,\text{cm}^{-3}$.

The second example is from the E164 experiment at FFTB and for experiments at FACET, where the bunch length was significantly reduced through compression. For typical E164 parameters, $N = 1.8 \times 10^{10}$, $\sigma_z = 32\mu$m, $\sigma_r = 10\mu$m and $n_{b0} = 3.6 \times 10^{17}\text{cm}^{-3}$. For these parameters, $\Lambda \approx 1.27$ and the linear theory predicts the optimum plasma density $n_p \approx 3.5 \times 10^{16}\,\text{cm}^{-3}$. We note that for these parameters the asymptotic expression for the optimum density for $\sigma_r/\sigma_z \ll 1$ is no longer applicable since $\sigma_r/\sigma_z \sim 0.3$. Therefore, we use a value from figure 2 in [70], where one sees that $k_p\sigma_z \approx 1.13$ is less than $k_p\sigma_z = \sqrt{2}$ consistent with the asymptotic formula.

To find out how well the linear theory predictions work, we performed simulations with QuickPIC by scanning the plasma density for the above two examples. The results are shown in Figures 3.7(b) and 3.8(b), where we plot both the absolute (in units of GV/m) and the normalized (by $m_e c\omega_p/e$) useful accelerating field amplitude against the plasma density. For the first example (the Fig. 3.7), the density range scanned is from $10^{13}\,\text{cm}^{-3}$ to $10^{15}\,\text{cm}^{-3}$. One can see clearly for this weakly nonlinear case the plasma density that maximizes the absolute accelerating field amplitude is very close to the linear theory prediction, $n_o = 1.15 \times 10^{14}\,\text{cm}^{-3}$.

For the second example (the Fig. 3.8), the density range scanned is from $10^{16}\,\text{cm}^{-3}$ to $10^{18}\,\text{cm}^{-3}$. For this more strongly nonlinear example, the absolute

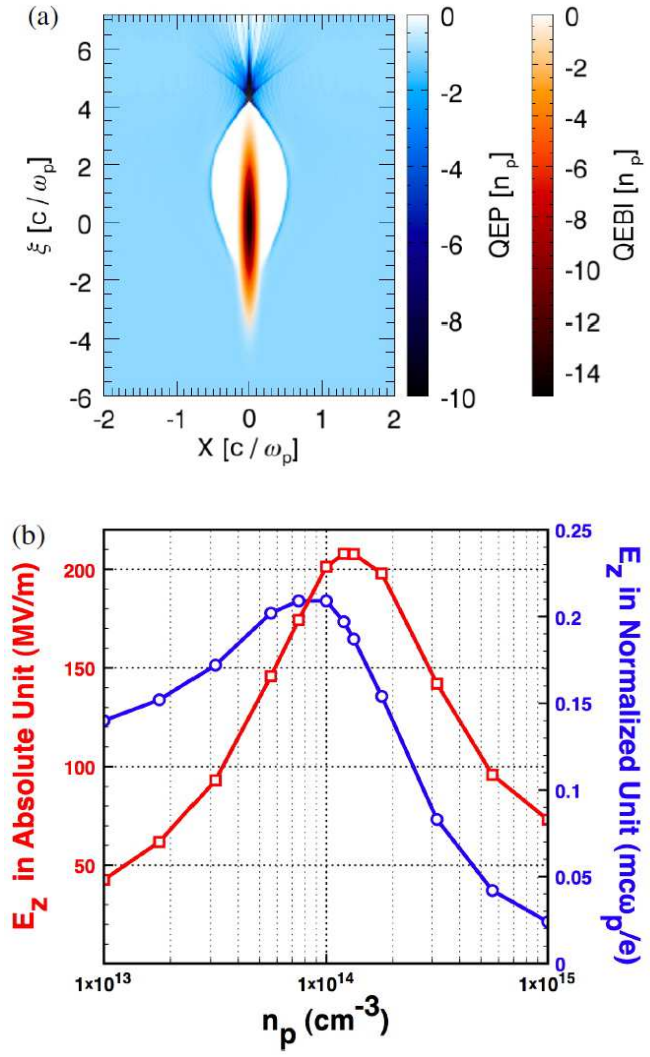

Figure 3.7: (a) The beam and plasma density distributions at the optimum density $n_o = 1.15 \times 10^{14}\,\mathrm{cm}^{-3}$ for a Gaussian electron beam with $N = 1.9 \times 10^{10}$, $\sigma_z = 700\mu$m and $\sigma_r = 30\mu$m. (b) The normalized and absolute useful accelerating field of the plasma wake.

maximum amplitude occurs at a density near $4.0\times10^{17}\,\mathrm{cm}^{-3}$, which is surprisingly more than ten times larger than the linear theory prediction $3.5\times10^{16}\,\mathrm{cm}^{-3}$.

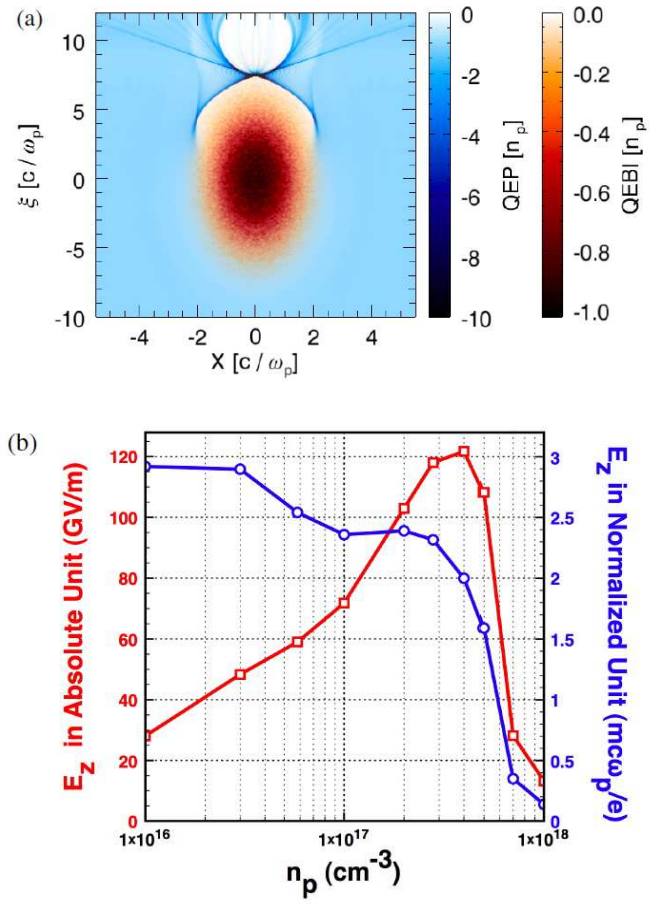

Figure 3.8: (a) The beam and plasma density distributions at the optimum density $n_o = 4.0\times10^{17}\,\mathrm{cm}^{-3}$ for a Gaussian electron beam with $N = 1.8\times10^{10}$, $\sigma_z = 32\,\mu$m and $\sigma_r = 10\,\mu$m. (b) The normalized and absolute useful accelerating field of the plasma wake.

The above two examples clearly demonstrate the usefulness and limitation of the linear theory predictions regarding to the optimum plasma density for wakefield amplitude. The question then is how can we understand these results? It turns out that a clear understanding and a simple estimation can be obtained based on physical intuition from the nonlinear wake field theory in [16, 17] (which is summarized in section 3.1).

In the nonlinear framework of the blowout regime [16, 17], the plasma response to the electron beam driver can be divided into three distinct regions, namely the ion channel, the narrow electron sheath and the linear response region beyond the sheath. The key parameter for identifying the different regimes is the maximum normalized blowout radius k_pR_b. In the non-relativistic blowout regime where $k_pR_b \ll 1$, the contribution from the linear response region dominates the wake-field structure; therefore, a formula similar to the linear theory expression can be used even though blowout occurs. In the regime where $k_pR_b \sim 1$, the contribution from both the ion channel and the linear response region is important. In the relativistic blowout regime where $k_pR_b \geq 2$, the ion channel dominates the contribution. The maximum normalized blowout radius k_pR_b is mainly determined by the peak beam current I_p (slightly dependent on the beam pulse length) and an approximate formula for a narrow drive beam ($\sigma_r < R_b$) is [17]

$$k_pR_b = 2\sqrt{\Lambda} = 2\sqrt{2I_p/I_A}, \tag{3.11}$$

This formula has been verified in self-consistent simulations, and it can be approximately obtained by equating the wake field forces on an electron moving backward in the sheath with the peak charge force of the beam [17]. As shown in [17], the normalized accelerating field amplitude scales as $\Lambda\ln(1/\Lambda)$ in the non-relativistic blowout regime ($\Lambda \ll 1$), which is similar to the prediction of linear theory. While in the relativistic blowout regime ($\Lambda \geq 1$) the normalized accelerating field amplitude scales as $\sqrt{\Lambda}$. For the given total beam particle number N, Λ is independent of the plasma density n_p and the beam spot size σ_r and only depends on the pulse length σ_z. However, for equation 3.11 to be meaningful in the blowout regime, there are indeed two implicit conditions: the first one is that the beam should not be much shorter than a plasma skin depth k_p^{-1}, otherwise the plasma blowout will not occur within the bunch and the plasma electrons simply receive an impulse from the beam, in which case the blowout radius will be determined by the total charge in the beam rather than the peak current of the beam

[17]; the other condition is that the beam density n_{b0} should be comparable or larger than the ambient plasma density n_p, such that the condition for trajectory crossing and blowout is satisfied. The first condition implies a lower limit on the plasma density, e.g. $k_p\sigma_z \geq 0.2$ and the second implies an upper limit on the plasma density, e.g. $n_p \leq n_{b0}$ or $k_p\sigma_r \leq \sqrt{\Lambda}$.

We are now in a position to determine the optimum density in the blowout regime for either the non-relativisitic ($\Lambda \ll 1$) or relativistic ($\Lambda \geq 1$) regimes for cigar-shaped beams ($\sigma_r \ll \sigma_z$). We fix the beam parameters (N, σ_r, σ_z) and then gradually increase the density. We start at a sufficiently low density, such that the first condition in the previous paragraph is not met (e.g. $k_p\sigma_z \leq 0.2$). In this regime, the meaningful parameter for determining the blowout radius and wakefield amplitude is the normalized total charge $Q \equiv \Lambda k_p\sigma_z$, because only the total impulse from the beam matters ($k_pR_b \propto \sqrt{Q}$) [17]. Q increases as the plasma density increases from zero to the lower limit; therefore, for both the non-relativistic and relativistic blowout regimes in this density range, both the normalized and the absolute wakefield amplitudes increase as the density increases.

As the density is increased further into an intermediate range (where $k_p\sigma_z \geq 0.2$ and $k_p\sigma_r \leq \sqrt{\Lambda}$, assuming $\sigma_r < \sigma_z$), we need to treat the non-relativistic and relativistic blowout regimes differently. In the non-relativistic blowout regime, the wake amplitude is roughly determined from the linear theory so the optimum density is about $k_p\sigma_z = \sqrt{2}$. On the other hand, for the relativistic blowout regime, the normalized wakefield amplitude is determined by the normalized blowout radius k_pR_b , which for this density range is approximately given by $k_pR_b \approx 2\sqrt{\Lambda}$. Since Λ does not depend on the plasma density, the normalized wakefield amplitude is insensitive to the density. Therefore, the absolute wake field amplitude will increase with the plasma density in this density range, implying we should continue to increase the density.

For the relativistic blowout regime ($\Lambda \geq 1$), as the density is increased further

it eventually exceeds the upper limit (e.g. $n_p \geq n_{b0}$ or $k_p\sigma_r \geq \sqrt{\Lambda}$). At this point the wake is now marginally excited in the blowout regime and the linear expression becomes valid again. Therefore, if $k_p\sigma_z < \sqrt{2}$, then the density can be increased further to increase the amplitude until $k_p\sigma_z = \sqrt{2}$. However, for cigar-shaped beams if $k_p\sigma_r \geq \sqrt{\Lambda}$, then $k_p\sigma_z \gg \sqrt{2}$. As a result the wake amplitude will decrease as the density is increased further. We therefore conclude that the maximum wakefield amplitude is reached near $n_{b0}/n_p \sim 1$. For $\Lambda \geq 1$ and $n_{b0} \sim n_p$, the normalized beam spot size is $k_p\sigma_r = \sqrt{\Lambda} \sim k_pR_b/2$. Therefore, the absolute accelerating field is maximized when the spot size is roughly matched to the blowout radius (for example, one can see this from the beam and plasma density plot in figure 3.8(a)).

We note that for the above analysis to be valid, an additional condition, $\sigma_z \leq 5R_b \approx 10\sigma_r$, should be imposed. Otherwise the beam plasma interaction will be in the adiabatic blowout regime where the ion channel is balanced by the electric and magnetic force of the beam and the wake amplitude scales as $\sim \sqrt{\Lambda}/k_p\sigma_z$ [70].

To see the validity of the above analysis and reasoning, we revisit the two examples given earlier in this section. In the first example, the electron pulse is relatively long ($\sigma_z = 700\,\mu$m) and it has $\Lambda = 0.06$; therefore, it is within the non-relativistic blowout regime and the optimum plasma density should be close to the linear theory prediction. This was confirmed in Figure 3.7(b) as mentioned earlier. For the second example, the pulse length is much shorter ($\sigma_z = 32\,\mu$m) and it has $\Lambda = 1.27$ and $n_{b0} = 3.6 \times 10^{17}\,\mathrm{cm}^{-3}$. Therefore, it is in the relativistic blowout regime and an optimum plasma density close to the beam peak density n_{b0} should be expected. The QuickPIC simulation results shown in Figure 3.8(b) confirmed this: the trend of the absolute accelerating field amplitude increasing with density and the optimum density, $n_o \approx 4{\times}10^{17}\,\mathrm{cm}^{-3}$, is close to the prediction of $3.6 \times 10^{17}\,\mathrm{cm}^{-3}$. In light of the factor of ten difference of the plasma density

between the linear and nonlinear predictions, this agreement clearly shows the usefulness of the above reasoning.

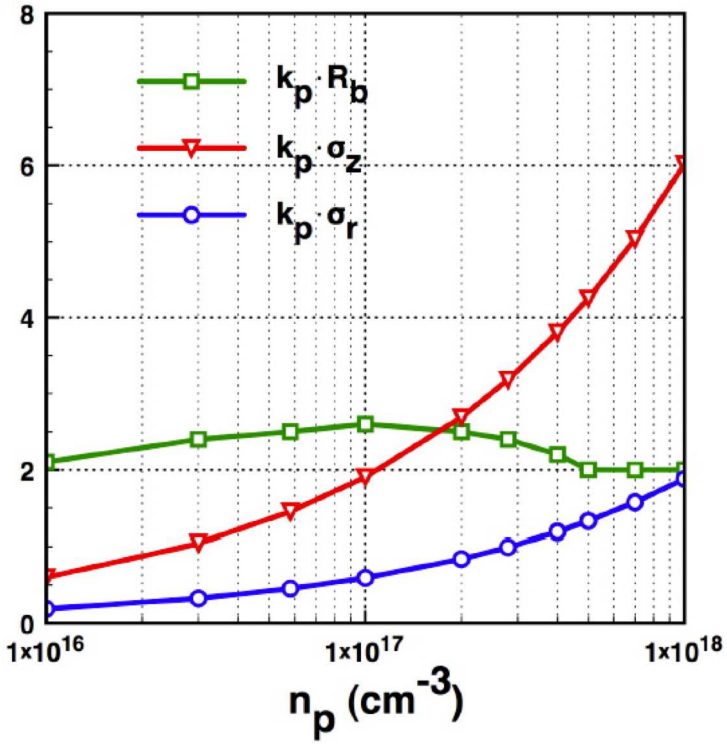

Figure 3.9: The normalized beam parameters $k_p\sigma_r$, $k_p\sigma_z$ and the maximum normalized blow-out radius k_pR_b for a Gaussian beam with $N = 1.8 \times 10^{10}$, $\sigma_z = 32\,\mu$m and $\sigma_r = 10\,\mu$m.

In the above we argued that k_pR_b is very insensitive to the density for fixed Λ. To show this we also plot the normalized blowout radius against plasma density for the simulations in Figure 3.8(b). In Figure 3.9, it is evident that the maximum normalized blowout radius k_pR_b changes very little for plasma densities spanning two order of magnitude. The average k_pR_b is around 2.2 and is close to the theoretical estimate of $2\sqrt{\Lambda} \approx 2.25$. We note that for $n_p > n_{b0}$ in Figure 3.9, the maximum blow-out radius is not clearly defined and it is roughly deduced from the density perturbation in the simulations.

3.4 Two-bunch PWFA at FACET

Recent experiments on FFTB at SLAC [51] demonstrated that a PWFA could be produced with an accelerating gradient of $\sim 52\,\mathrm{GeV/m}$ over a meter-long scale. However, as shown in Ref.[51], electrons accelerated in the beam tail have an almost 100% energy spread, which is surely not what one wants for a high energy particle accelerator. Nevertheless, a locally uniform accelerating field can be obtained if we load a second electron beam (which has a proper beam current) appropriately inside the plasma wake of the first beam (Fig. 3.11). As shown in reference [67], even a trailing beam with a Gaussian current profile can flatten the wake in the nonlinear regime. This second bunch needs to have a high initial energy so that the phase slippage between the accelerated beam and the wakefield of the first beam can be ignored during the acceleration process in the plasma. In this manner the energy spread of the second bunch will be significantly decreased.

This two-bunch PWFA scheme is an important part of upcoming experiments at FACET (Facilities for Accelerator Science and Experimental Test Beams) at SLAC [52] for demonstrating a high energy gain while maintaining a narrow energy spread. The two bunches are produced from a single bunch by placing a mask in the middle of the last chicane (for compressing the bunch) on the beamline. Before the last chicane, the single bunch has already been given an energy spread that is correlated to its longitudinal (or temporal) position within the bunch. In the middle of the chicane the dispersion of the bunch will be correlated to its energy spread as well as the longitudinal distribution of the bunch. When the bunch passes through the mask the dispersion space of the bunch will be modified resulting in a modulation of the longitudinal distribution of the bunch after it gets out of the chicane. In this way a single bunch will finally turn into two bunches with a separation between them.

Extensive QuickPIC simulations were carried out to motivate the construction

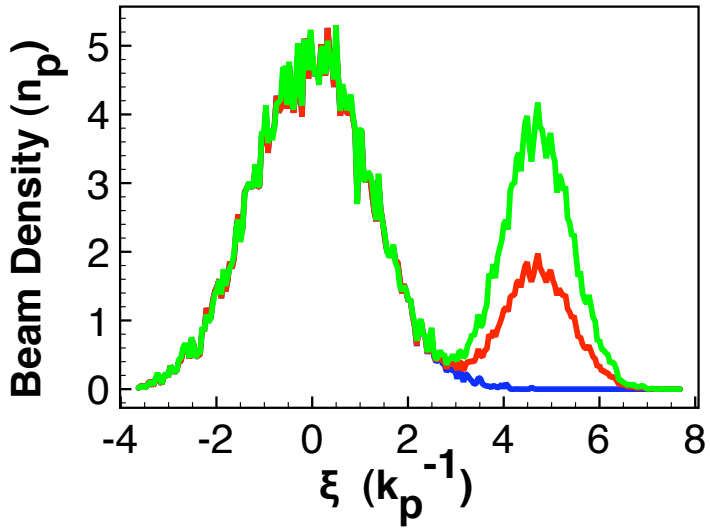

(a)

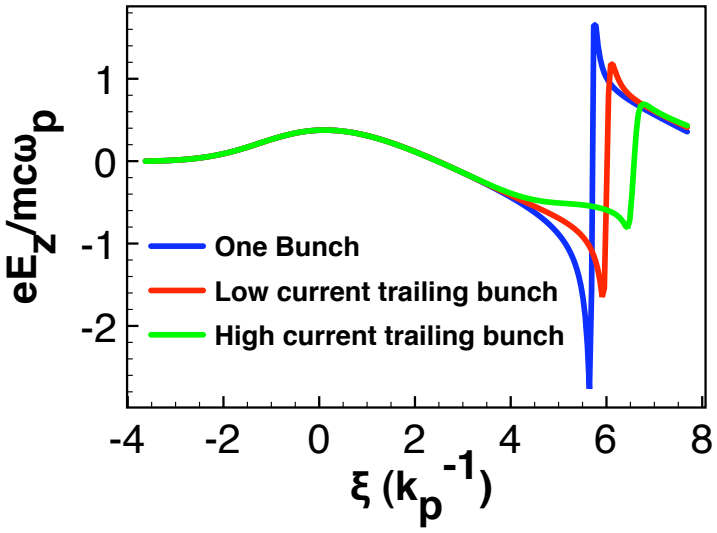

(b)

Figure 3.10: Plasma wakefields with different beam loads. (a) Lineouts of different longitudinal beam profiles; (b) Lineouts of E_z along the axis. The two bunches are moving from right to the left.

of FACET and to help design the two-bunch experiments. Two cases of these simulations are presented in this section. The initial electron beam parameters of these two cases are both based on the overall simulation of the entire FACET system. QuickPIC is used to model the process of the two electron bunches traveling through the neutral gas (Lithium and Cesium). For each case we are using a plasma density which is optimized to minimize the energy spread of the accelerated bunch.

3.4.1 Case I

In case I the r.m.s. spot size of each electron beam is $\sigma_{r1} = \sigma_{r2} = 10\,\mu$m (1 stands for the drive beam, 2 stands for the trailing beam); the r.m.s. beam length of each beam is $\sigma_{z1} = 18\,\mu$m, $\sigma_{z2} = 25\,\mu$m; the transverse r.m.s. normalized emittance of each beam is $\epsilon_{x1,2} = \epsilon_{y1,2} = 50\,\text{mm}\cdot\text{mrad}$; the particle number of each beam is $N_1 = 6.7\times10^9$, $N_2 = 2.3\times10^9$; the distance between two beam centers is $115\,\mu$m and the initial energy of each beam is $E_{01} = E_{02} = 23\,\text{GeV}$.

Figure 3.11 shows the difference between using Li and using Cs. The initial gas density is $5.0\times10^{16}\,\text{cm}^{-3}$ in both cases. For the Li gas the ionized plasma column is wide enough to maintain a large plasma wake over long distances. The drive beam intensity drops significantly after traveling 64.18 cm in Li while in Cs the drive beam remains intense at the same distance, which means the drive beam can propagate longer in Cs. Therefore, the acceleration length and final energy gain of the second electron bunch will be increased when using Cs instead of Li.

However, even though the acceleration length can be increased with Cs, for the beam parameters of Case I there does not appear to be an ideal plasma density which can be used to generate a narrow energy spread of the accelerated beam. This is because the second bunch does not have a strong enough beam current (similar as the second case shown in Fig. 3.10) to flatten (load) the wake. Figure

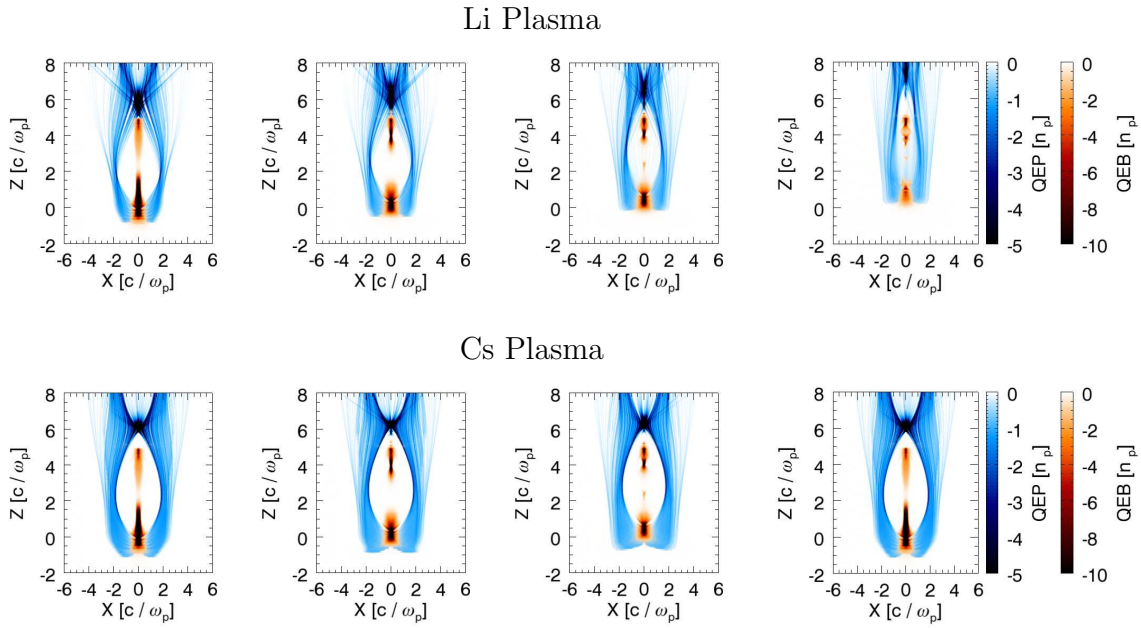

(a) $s = 14.3\,\text{cm}$ (b) $s = 30.9\,\text{cm}$ (c) $s = 47.5\,\text{cm}$ (d) $s = 64.2\,\text{cm}$

Figure 3.11: Snapshots of plasma electron charge density (in blue) and the beam charge densities (in brown) at different propagation distances. The plots of the first row are simulation results using Li and the second row are results using Cs. The beams are moving downwards.

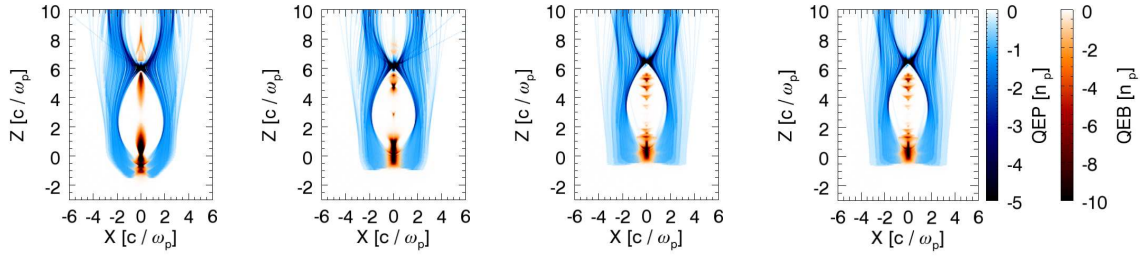

(a) $s = 5.0\,\text{cm}$ (b) $s = 35.2\,\text{cm}$ (c) $s = 65.3\,\text{cm}$ (d) $s = 95.6\,\text{cm}$

Figure 3.12: Snapshots of plasma electron charge density (blue) and the beam charge densities (brown) at different propagation distances when using Cs with the density of $7 \times 10^{16}\,\text{cm}^{-3}$. The beams are moving downwards.

3.12 shows snapshots of plasma and electron beam densities when the Cs density is increased to $7 \times 10^{16}\,\mathrm{cm}^{-3}$. The drive beam can travel almost one meter inside the plasma before the plasma wake terminates. Figure 3.13 shows the energy spectrum of the trailing beam at the final point. Since the rear part of the trailing beam is located outside the first bucket, this part will feel a decelerating field. As a result one peak with an energy loss appears in the spectrum. The accelerated part of the trailing beam has a peak energy of 37 GeV and the maximum energy gain is around 20 GeV. The energy spread is around 35% (FWHM value) which is rather large. If the plasma density is increased further, fewer particles in the trailing beam will get accelerated and the energy spread of these beam particles will approach 100%.

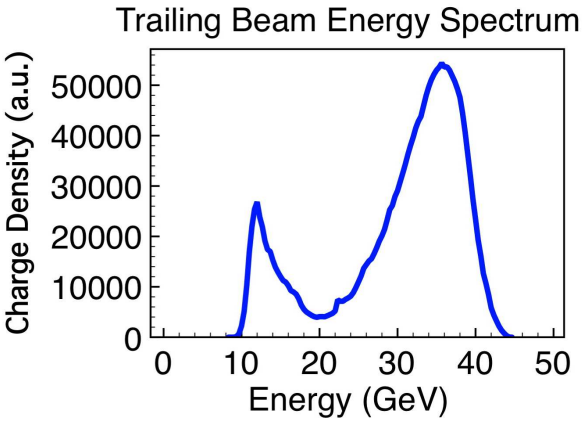

Figure 3.13: The energy spectrum of the trailing beam at $s = 95.6\,\mathrm{cm}$. The numbers on the y axis are reference values with arbitrary units.

3.4.2 Case II

In case II the r.m.s. spot size of each electron beam is still $\sigma_{r1} = \sigma_{r2} = 10\,\mu\mathrm{m}$; the r.m.s. beam length of each beam is now $\sigma_{z1} = 34.1\,\mu\mathrm{m}$, $\sigma_{z2} = 19.3\,\mu\mathrm{m}$; the transverse r.m.s. normalized emittance of each beam is now $\epsilon_{x1,2} = \epsilon_{y1,2} = 100\,\mathrm{mm} \cdot \mathrm{mrad}$; the particle number of each beam is now $N_1 = 9.57 \times 10^9$,

$N_2 = 4.33 \times 10^9$; the distance between two beam centers is now 130 μm and the initial energy of each beam is still $E_{01} = E_{02} = 23$ GeV. Note that for Case II although N is larger, the peak current of the drive beam ($\propto \frac{N_1}{\sigma_{z1}}$) is 0.75 times less than that for Case I.

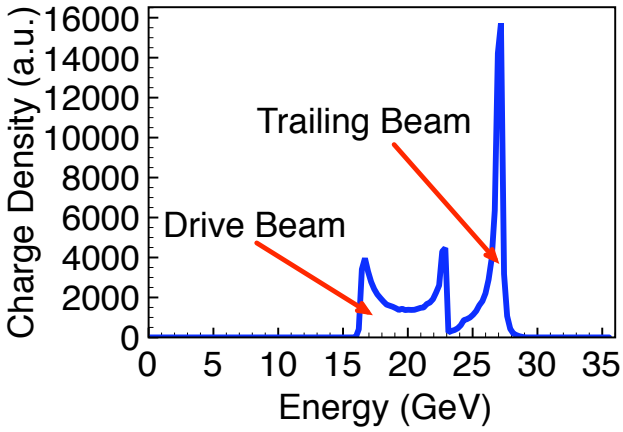

(a)

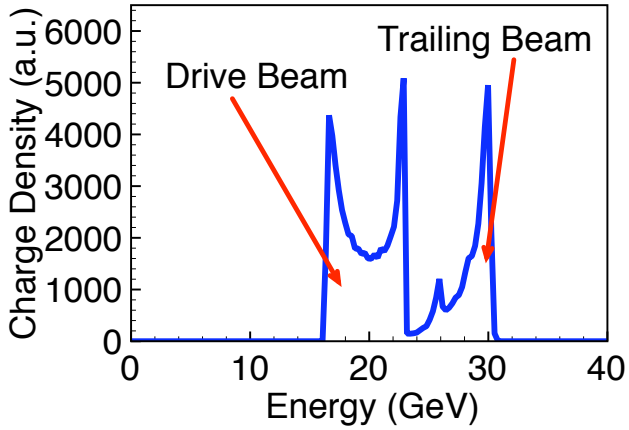

(b)

Figure 3.14: The energy spectra of both beams at (a) $s = 88.6$ cm for a plasma density of 3.7×10^{16} cm^{-3} and (b) $s = 76.2$ cm for a plasma density of 5.0×10^{16} cm^{-3}. The numbers on the y axis are reference values with arbitrary units.

For this case we only consider Cs and find two optimal plasma densities, 3.7×10^{16} cm^{-3} and 5.0×10^{16} cm^{-3}. For the lower initial plasma density, the trailing

beam is almost located inside the first bubble of the plasma wake while for the higher initial plasma density, a part of the trailing beam is in the second bucket resulting in a broader energy spread. Nevertheless, both of these cases still have very small energy spreads, which are less than 3% (FWHM value). But the energy gain (5 GeV for low plasma density and 7 GeV for high plasma density) are less than that in Case I. The final energy spectrum (Fig. 3.14) also shows that the drive beam still has a lot of energy when the plasma wake terminates. This is mainly caused by the ionization-induced drive beam head erosion, which will be discussed in the next section.

3.5 Mitigating the ionization-induced beam head erosion in an electron-beam-driven PWFA

Beam head erosion can occur in a preformed plasma because of a lack of focusing force from the wake at the rising edge (head) of the beam due to the finite inertia of the electrons. When the plasma is produced by field ionization from the space charge field of the beam, the head erosion is significantly exacerbated due to the gradual recession (in the beam frame) of the 100% ionization contour [62]. Beam particles in front of the ionization front cannot be focused (guided) causing them to expand as in vacuum. When they expand, the location of the ionization front recedes such that even more beam particles are completely unguided. Eventually this process terminates the wake formation prematurely, i.e., well before the beam is depleted of its energy. Ionization-induced head erosion can be mitigated by controlling the beam parameters (emittance, charge and energy) and/or the plasma conditions. In this section we explore how the latter can be optimized so as to extend the beam propagation distance and thereby increase the energy gain. In particular we show that, by using a combination of the alkali atoms (Cs) of the lowest practical ionization potential for plasma formation and a precursor laser

pulse to generate a narrow plasma filament in front of the beam, the head erosion rate can be dramatically reduced. Simulation results show that in the upcoming "two-bunch PWFA experiments" on the FACET facility at SLAC national accelerator laboratory the energy gain of the trailing beam can be 10 times larger for the given parameters when employing these techniques.

In the two-bunch PWFA scenario described earlier, it is imperative that the drive beam transfer most of its energy to the plasma wake in order to efficiently transfer energy to the trailing beam. Since both the drive and the trailing beams are usually highly relativistic there is no significant relative motion between the two until the drive beam has lost most of its energy. This allows high efficiency in principle. But because of the excessive beam head erosion, the acceleration distance and hence energy gain can be terminated if the drive beam is no longer able to create the plasma (and therefore the wake) through the field ionization process. In this case the energy gain of the particles in the trailing bunch is not limited by the energy depletion of the drive beam (pump depletion) but by head erosion. When the plasma is produced by E_r of the drive beam that has a temporally rising charge distribution, then the front of the beam (before the ionization threshold has been reached) expands as if it were in vacuum. Once the ionization threshold is exceeded then the beam begins to ionize the gas and expel the plasma electrons. However, due to the finite inertia of the electrons, the ion channel is not formed immediately after the ionization front and the focusing force of the ions is thus not strong enough to confine electrons behind the ionization front until enough plasma electrons have been blown out. This leads to different longitudinal slices of the beam expanding laterally at different rates because of their finite emittance, albeit at a rate smaller than they would if they were propagating in vacuum. This reduces the E_r from the beam near the ionization front causing the front to recede backward in the beam frame and leading to an even smaller portion of the beam to be confined. As more of the beam is not confined and the

ionization front recedes, a portion of the wake becomes smaller until eventually the wake can no longer be excited.

Figure 3.15 illustrates the phenomenon of beam head erosion by comparing the propagation of otherwise identical drive beams through either a neutral Lithium gas (where it produces plasma via field ionization) or through a preformed plasma with a transverse radius much larger than the electron blowout radius R_b caused by the drive beam. The preformed plasma density and the neutral Li gas density are both 5×10^{16} cm^{-3}. The drive beam contains $N = 9.6 \times 10^9$ electrons. It has a Gaussian profile and the r.m.s. spot size of the beam is $\sigma_r = 10\,\mu$m $(0.42\,c/\omega_p)$. The r.m.s. pulse length of the beam is $\sigma_z = 34.1\,\mu$m $(1.43\,c/\omega_p)$. The initial energy of the beam is 22.5 GeV. The 3D parallel quasi-static PIC code QuickPIC [43, 71] is used for the simulations. The simulation box uses the coordinate $\xi = ct - z$ instead of z in the longitudinal direction, which is equivalent to following the beam in the speed of light frame. The initial drive beam center is at $\xi = 0$, and the beam is moving downwards in the simulation box.

In contrast to the case of the fully pre-formed plasma which is initially uniform (see Fig. 3.15(b)), the field-ionized plasma has a "W" shape contour at the beam head because the beam's Coulomb field is not strong enough to ionize the neutral gas near the axis, i.e., recall that for a cylindrically symmetric, transversely Gaussian beam the E_r is zero on axis. Nevertheless in both cases a region of complete electron blowout does exist and the position where the expelled plasma electrons return to and cross the axis (also the position where the accelerating field is at its maximum) is at almost the same location, whereas in the preformed plasma case the expelled electrons form a very thin sheath around the ions, in the self ionized case this sheath is somewhat diffused. As time progresses, and as the beam propagates further into the gas, the ionization front recedes further and further (in the beam frame) and eventually limits the distance over which the beam can form the wake as discussed earlier.

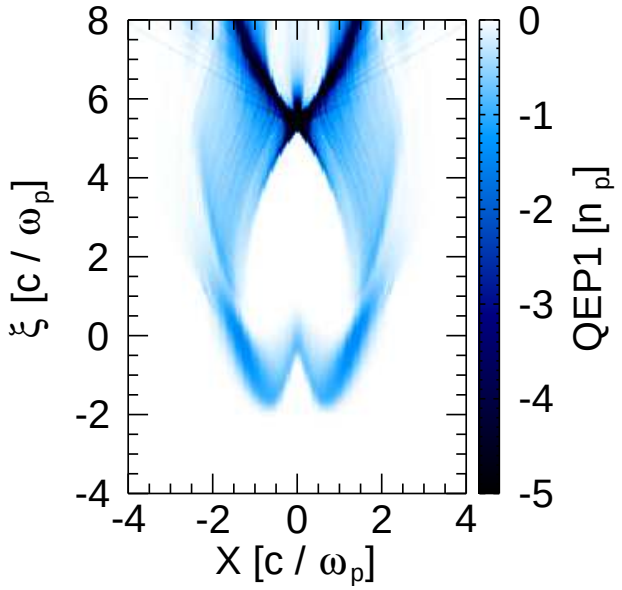

(a)

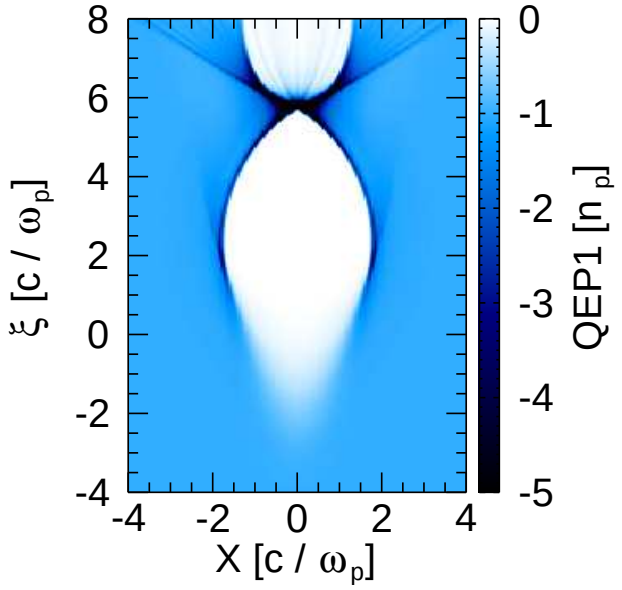

(b)

Figure 3.15: Snapshot of the plasma electron density from the wake exited by an electron beam in (a) a field ionized plasma and (b) a pre-formed plasma. The plots are 2D cross sections at the center of the 3D simulation box. The drive beam is moving downwards.

The rate at which the ionization front recedes, i.e., the "etching speed", can be used as a figure of merit to quantify the beam head erosion. The slower the etching speed , the longer is the distance over which a plasma wake can be sustained. In reference [62], the etching speed was found to be a constant for a drive beam with a flat top longitudinal profile, being proportional to $\epsilon_N/\gamma N^{1.5}$, where ϵ_N is the normalized emittance of the beam, γ is the beam Lorentz factor and N is the beam particle number. Thus we can mitigate the head erosion by reducing the emittance ϵ_N or increasing the beam particle number (N) or energy of the beam γ. For fixed beam parameters the only other way to mitigate the beam head erosion is to manipulate the plasma source. Next, we explore two techniques for doing this. The first is to use a neutral gas with as low an ionization potential as possible so that the onset of ionization will occur sooner during the rise-time of the beam. The second is to use a precursor laser pulse to form a very narrow plasma filament. We have found that both techniques (particularly when used together) dramatically reduce the beam etching speed and thereby increase the distance over which the beam can form the wake.

3.5.1 Dependence of the etching speed on the ionization potential

Different neutral atoms have different electron ionization potentials. For PWFA experiments a long column of neutral gas that typically has a low ionization potential is used. Using the ADK model [72], we can calculate each gas's ionization threshold E_{th}, defined as the external DC electric field at which the neutral gas can be fully ionized during a given time duration. This model has been shown to give reasonable agreement in experiments where the peak electric field of a 23.5 GeV electron beam necessary for the ionization of different simple and complex gases (noble, diatomic homopolar, polyatomic and monoatomic metal vapor) was determined [73]. In this work we consider different Group 1 alkali metal atoms because they have a very low threshold, E_{th}, for the outermost electron to be

ionized and a relatively larger difference between the ionization potentials of the first and the second electron (see Fig. 3.16).

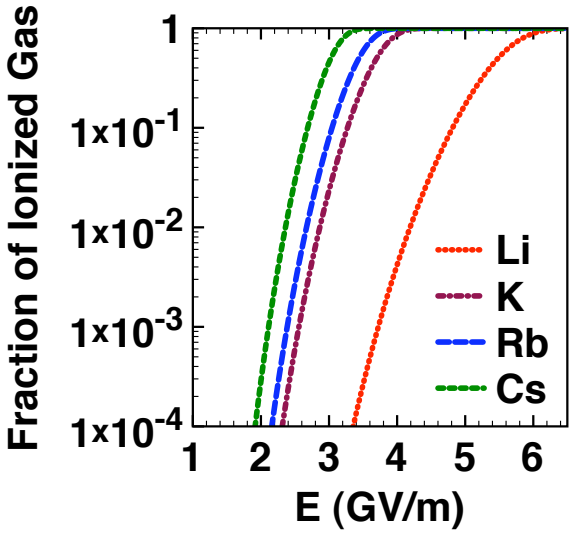

(a) 1st Ionization

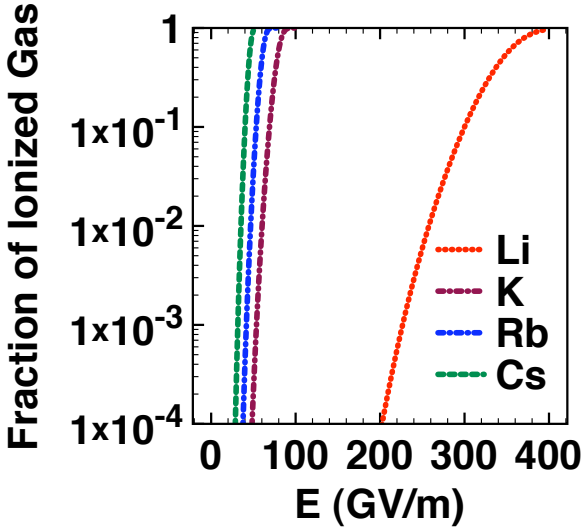

(b) 2nd Ionization

Figure 3.16: Fraction of Ionized Gas vs. the amplitude of the electric field.

Figure 3.16 shows the fractional ionization of different Group 1 alkali metal atoms as the magnitude of E field is increased. The ionization time duration is chosen to be 50 fs (which is the risetime of a typical electron beam pulse-length in

PWFA experiments). From this plot, we can see that for fully ionizing ($> 99\%$) the first electron (Fig. 3.16(a)) the threshold electric field E_{th} is 6.4 GV/m for Li, 4.3 GV/m for K, 4.0 GV/m for Rb and 3.5 GV/m for Cs and for fully ionizing ($> 99\%$) the second electron E_{th} is 409.2 GV/m for Li, 90.8 GV/m for K, 69.5 GV/m for Rb and 51.8 GV/m for Cs. This large gap of E_{th} between the first and the second ionization is one reason why it is possible to generate 100%, singly-ionized metal-vapor plasmas using the self-field of a short, dense electron beam. Nevertheless under certain conditions, the combined accelerating field of the wake E_z and the E_r of the beam can cause ionization of the second electron which can inject dark current into the plasma accelerator structure [74]. One therefore has to choose the right beam and plasma parameters so that $\sqrt{E_r^2 + E_z^2}$ should be smaller than E_{th} for the second electron.

The first generation of PWFA experiments used Li vapor to generate field-ionized plasmas. However the ionization potential of the heavier alkali metal atoms becomes progressively smaller (5.4 eV for Li vs. 3.9 eV for Cs for the outermost electron) with a corresponding decrease in the electric field needed to fully ionize them as stated earlier. This in turn means that as the drive beam propagates through a column of say Cs vapor compared to Li vapor, ionization will occur sooner during the risetime of the pulse and the rate at which the ionization front recedes as the beam propagates further into the vapor will be smaller.

To quantify this ionization potential dependence on the head erosion speed, we have carried out several QuickPIC simulations with the same electron beam parameters but with the beam propagating through different alkali vapor columns. The electron beam has a flat top longitudinal profile and a Gaussian transverse profile. The beam contains $N = 9.6 \times 10^9$ electrons, its r.m.s. spot size is $\sigma_r = 10\,\mu\text{m}\ (0.42\,c/\omega_p)$, and its pulse length is $L = 85.5\,\mu\text{m}\ (3.59\,c/\omega_p)$. The normalized emittance of the beam is $\epsilon_N = 150\,\text{mm} \cdot \text{mrad}$ and the initial energy of the beam is 22.5 GeV (the energy of the beam particle is fixed during the simulation in

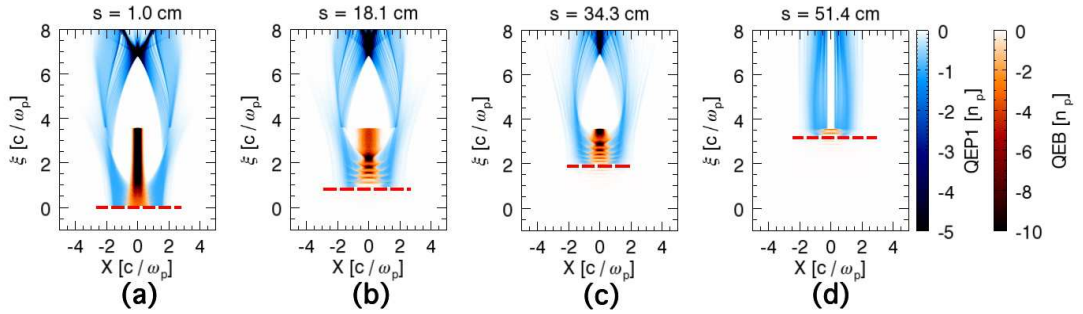

Figure 3.17: Beam head erosion in the field-ionized Lithium plasma. The plasma electron density is shown in blue and the beam density is in brown. $\xi = ct - z$ is the distance in the speed of light frame and $s = z$ is the propagation distance in the lab frame. Dotted lines in (a) - (d) show the position of the ionization front.

order to eliminate the dependence of the etching speed on the beam energy). The initial neutral gas density is $5 \times 10^{16}\,\mathrm{cm}^{-3}$. Figure 3.17 shows the beam evolution in neutral Li.

We can see that the ionization front moves backwards in the frame of the beam during its propagation due to continuous expansion of the front slices of the beam. After around 50 cm of propagation, the remainder of the beam is no longer able to form the wake and as a consequence, an on axis hole in the plasma (due to the on axis E_r being below the ionization threshold) is evident. We can visualize the recession of the ionization front by plotting the on-axis amplitude of the accelerating electric field E_z of the plasma wake field at different propagation distances, $E_z(r = 0, \xi, s)$ as shown in Figure 3.18 for the alkali metals Li, K, Rb and Cs.

In these plots, the red dashed line shows the trajectory of the onset of the wake field (a contour for $E_z = 0.1$). The line has a positive slope indicating that the ionization front is receding as the beam propagates in the plasma. In the Li gas, the plasma wake is gone at around s = 50 cm, which is the same distance as that shown in the Fig. 3.17. But in other neutral gases with lower ionization

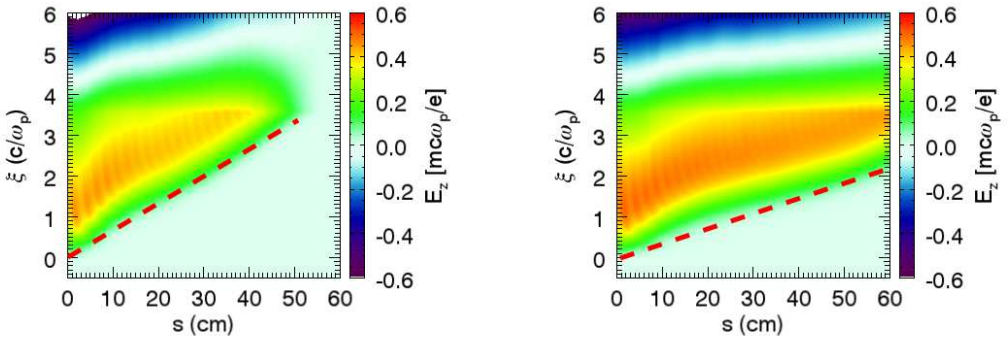

(a) Li

(b) K

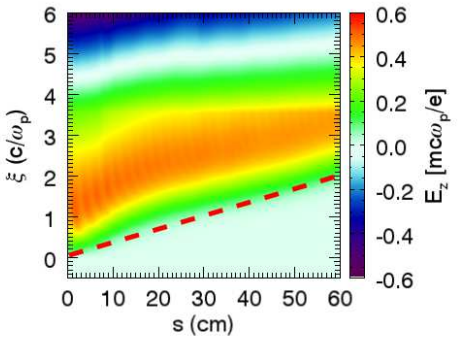

(c) Rb

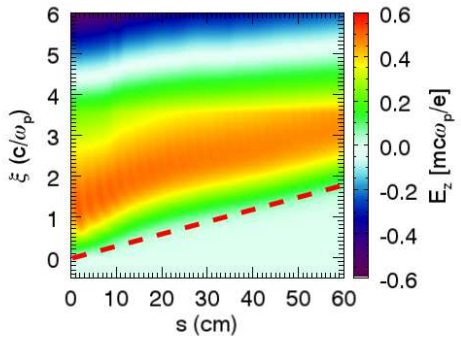

(d) Cs

Figure 3.18: E_z evolution during the beam propagating in different Alkaline metal gases. The beam is moving downwards.

potential than Li, the slopes are progressively smaller indicating that the plasma wakes can be sustained over a longer distance. We define the etching speed for the different gases to be the slope of the dashed red lines. In Fig. 3.19 we plot the etching speed for the various gasses.

Figure 3.19(b) shows that the etching velocity is linearly proportional to the ionization threshold [62] indicating that as expected it is better to use a neutral gas with as low an ionization threshold as possible like Rb or Cs to slow down the speed at which head erosion occurs if field ionization is employed to both produce the plasma and excite the wake.

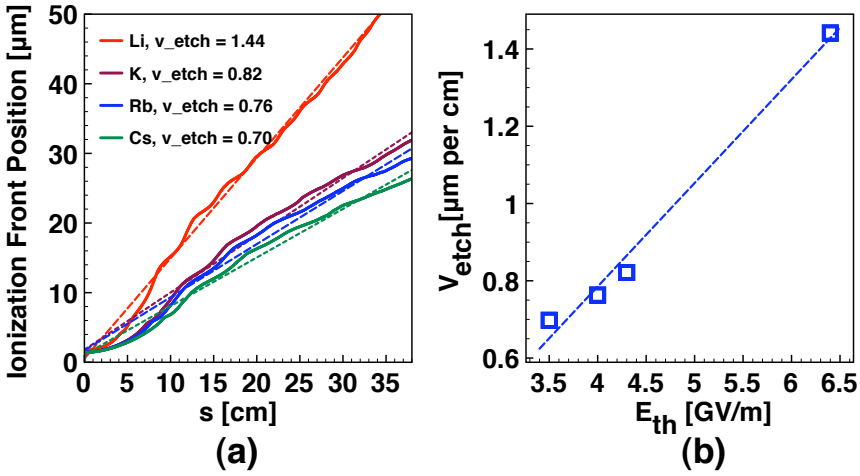

Figure 3.19: Ionization front etching in different gases: (a)Receding of the ionization front in different Alkaline metal gases; (b) The etching velocity verses the neutral gas ionization threshold.

3.5.2 Further mitigation of the head erosion rate using a laser-produced plasma filament

As already shown by the comparison of the snapshot of Fig. 3.15(a) with that of Fig. 3.15(b), in a pre-formed plasma the phenomenon of beam head erosion is significantly less and relatively unimportant. Using the E_z time-evolution format

of Fig. 3.18, the effects of additional pre-formation of a plasma in Li is shown in Fig. 3.20 for various pre-plasma conditions. These range from the extremes of the fully pre-formed plasma of Fig. 3.20(a), to that of field ionization only with no pre-formed plasma as in Fig. 3.20(c), together with the interesting intermediate case of Fig. 3.20(b), where the plasma is pre-formed over a much smaller volume, i.e., only along a narrow filament. The electron beam used in the simulation has the same parameters as those in the last section except it now has a Gaussian (rather than flat top) longitudinal profile with a pulse length $\sigma_z = 34.1\mu$m ($1.43\, c/\omega_p$).

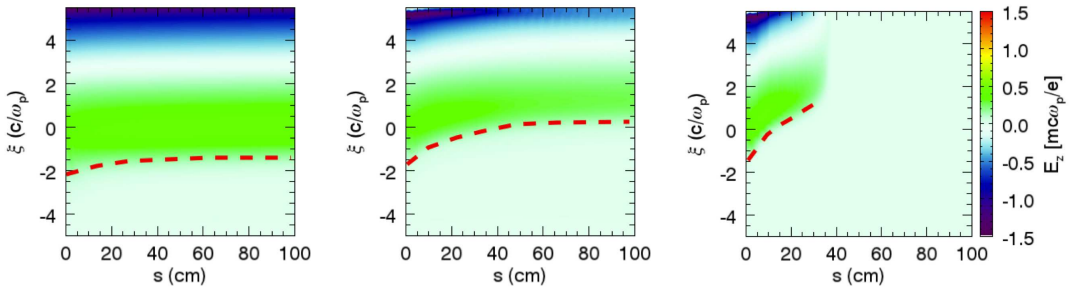

(a) (b) (c)

Figure 3.20: E_z evolution during the beam propagating in (a) a fully pre-formed plasma;(b) a field ionized Li plasma;(c) a field ionized Li plasma with the narrow plasma filament. The beam is moving downwards.

One can immediately see from Fig. 3.20(a) that in contrast to the self-ionized plasma case depicted in Fig. 3.20(c), there is almost no head erosion in the pre-formed Li plasma (Note that the slope of the red dashed line in this figure is not constant because the beam now has a Gaussian current profile).

Unfortunately it is not easy to produce large diameter, uniform density plasmas in the $1.0 \times 10^{16} \sim 5.0 \times 10^{17}\text{cm}^{-3}$ range. To fully ionize the gas in front of the drive beam, a laser pulse that tunnel or multi-photon ionizes the gas ahead of the drive beam can be used. The drive beam can then excite the plasma wake in this pre-formed plasma. The radius of the pre-formed plasma column should be larger than several times the blow out radius of the wake. This in turn implies that

the laser pulse should have enough energy to maintain the intensity above the ionization threshold over the entire volume of the gas that needs to be converted into plasma. This can require rather expensive laser infrastructure particularly if plasma columns that are several meters in length are needed.

We therefore explored whether a laser precursor pulse that generates only a narrow filament of Li plasma in front of the drive beam is sufficient to drastically reduce the beam head erosion. In this case the laser beam ionizes a plasma column that is only σ_r (the beam spot size) in radius. The Li plasma is then pre-produced by the laser pulse only where the laser intensity is sufficiently high (and in the case of interest, with a radius not nearly as large as the blow-out radius). This allows the very front of the beam, where the beam's E_r is too weak to ionize the neutral Li gas, to be more correctly guided, thereby greatly reducing the rate of ionization-induced head erosion. Such narrow but long plasma columns can be produced using axicon (a conically formed refractor element forming an extended line focus) optics to focus the laser pulse. Figure 3.21 shows density plots from a simulation depicting the propagation of the drive beam in a narrow pre-formed plasma column.

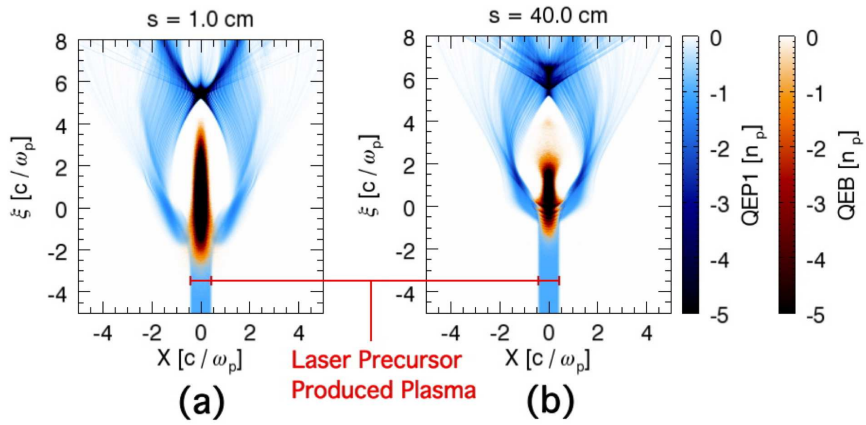

Figure 3.21: Density snapshot of the plasma wake with a small preformed plasma column. The plasma electron density has the blue color and the beam density is in brown.

In this simulation, we use Lithium for the gas and the pre-formed plasma column has a radius of $10\,\mu$m, which is equal to the spot size of the electron beam. Although the plasma filament is not wide enough to include the whole bubble of the wake, it can provide a fully ionized plasma region for the head of the beam. The Coulomb field of the main part of the electron beam subsequently ionizes the neutral gas around the narrow plasma filament allowing a wake to be formed.The two plots correspond to when the electron beam enters the plasma (Fig 3.21 a) and after it has propagated 40 cm into the plasma (Fig 3.21 b).

Returning now to Fig. 3.20 we compare the result (in Fig. 3.20(b)) of axial Li pre-ionization with that of full volume Li pre-ionization (Fig. 3.20(a)), where we see that the performance in terms of beam persistence is nearly as good, with excellent propagation beyond 100 cm. This is because head of the beam can now begin to expel plasma electrons in the filament thereby providing a focusing force on the front slices of the electron beam as in the preformed case keeping it from expanding or reducing the rate of expansion and thus reducing the head erosion rate. In comparison, the result with no Li pre-ionization (Fig. 3.20(c)) is disastrous (rapid erosion and ionization front movement resulting in a much shorter penetration of about 30 cm). The method of axial Li pre-ionization can drastically reduce the energy required in the laser pulse by a factor of $(R_b/\sigma_r)^2$, thereby making the laser infrastructure needed more manageable. We have also used Cesium for the gas. For these beam parameters the head erosion looks similar while the wake looks better for Cesium because the gas is ionized out to a radius closer to the blowout radius.

3.5.3 Simulation results for two-bunch FACET experiments

We next investigate the use of a laser precursor and the choice of either Lithium or Cesium for the oven gas with parameters of relevance to the upcoming two-bunch experiments at FACET. As discussed earlier, by employing lower ionization

energy atoms and/or a laser precursor to form a thin plasma filament ahead of the drive beam it is possible to mitigate the head erosion rate. We now show that it is possible to propagate the drive beam until it is efficiently depleted of its energy while forming a high gradient wake by combining both the precursor and Cesium gas for the FACET parameters. We also show that by beam loading such a wake with a trailing beam it is possible to transfer much of the energy in the wake to this trailing beam while obtaining a narrow energy spread. We simulated such a two-bunch PWFA scenario in the field-ionized Li plasma and then, in view of the behavior seen in Li, again in a Cs plasma, with results for both shown in Figs. 3.22 and 3.23. In Fig. 3.22(a) we show the plasma and beam densities for the Li case as the beams enter the gas.

In the simulation, the beams parameters are the same as the case II in the section 3.4.2. The plasma density is $5 \times 10^{16}\,\mathrm{cm}^{-3}$, which is properly chosen so that the plasma wake contains the trailing beam in the accelerating phase of the wake. The beams' energy spectra after propagation through the Li plasma are shown in Fig. 3.23(a). As a comparison, we also show the beams' spectra after 200 cm acceleration in a fully pre-formed Li plasma in the same plot. We explored the use of different gas densities. The tradeoff is that for higher densities the blow out radius is less so a narrow ionization column is needed (allowing Lithium to be used) while on the other hand at high densities the wake wavelength is shorter and the spacing between the drive and trailing beams will be too short. The plasma density used represents a starting choice for the FACET parameters where the beam parameters including the spacing and charge are fixed. Note that the drive beam parameters are identical to the case shown in Fig. 3.21(a) but that the beam appears longer in Fig. 3.21(a) because the beam has been pinched.

We can see that in the fully pre-formed plasma (brown curve in Fig. 3.23(a)) the trailing beam obtains an energy gain of around 30 GeV (at an average rate of 15 GeV/m) while more importantly the FWHM (Full Width at Half Maximum)

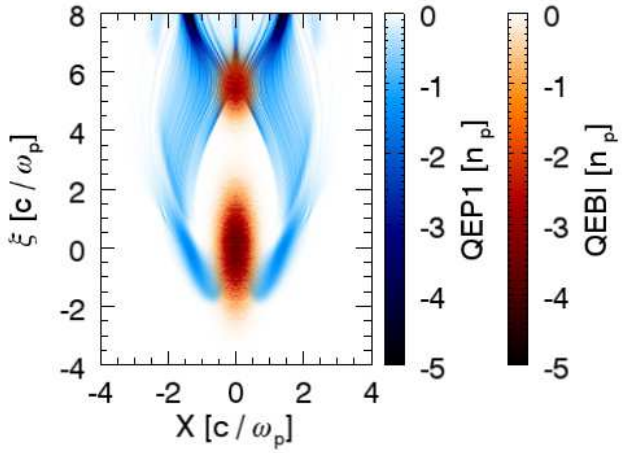

(a) Li

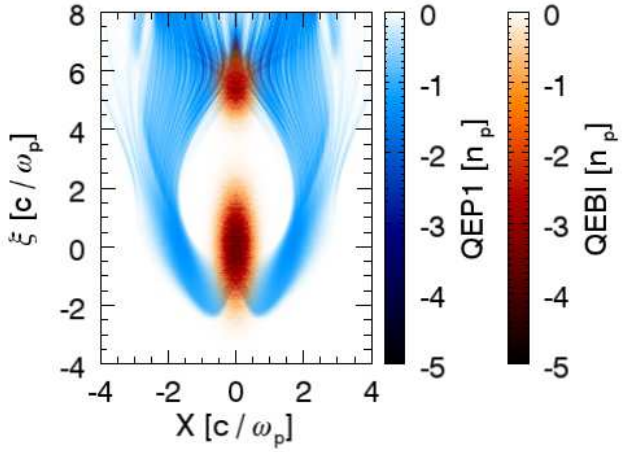

(b) Cs

Figure 3.22: Snapshot of a two-bunche PWFA in (a) a field ionized Li plasma (b) a field ionized Cs plasma. The plasma electron density has the blue color and the beam density is in brown.

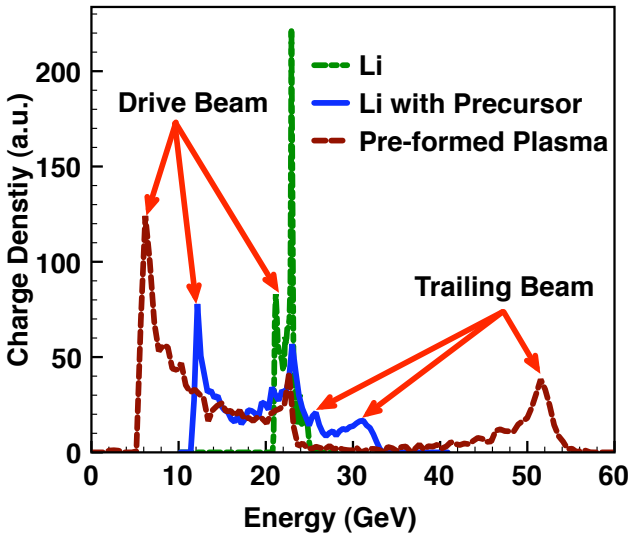

(a)

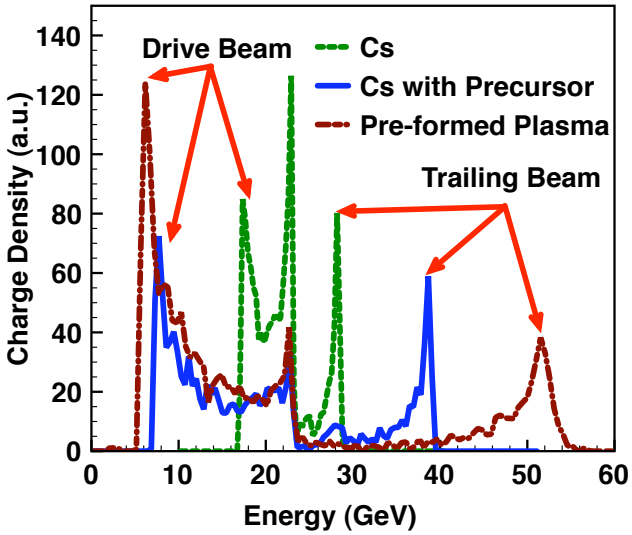

(b)

Figure 3.23: Energy spectra of the drive beam and the trailing beam at the end of the acceleration: (a) In a field ionized Li plasma; (b)In a field ionized Cs plasma.

energy spread is around 5% (note that this energy spread can be reduced further by optimizing the pre-formed plasma density for a given drive-trailing beam combination). The energy transfer efficiency from the drive to the trailing beam is 69.3%.

However if we use the beam's self-field to ionize the Li vapor the acceleration length is only 16.7 cm (as compared to 200 cm) and the energy gain of the trailing beam is only 2 GeV (the green line in Fig. 3.23(a)). The large spike in the middle of the spectrum shows that a considerable fraction of the electrons in the drive beam do not lose energy due to head erosion. The maximum energy loss of the drive beam electrons is around 2 GeV.

If however the head erosion is mitigated by using a plasma filament that has a radius of 10 μm, which is equal to the drive beam spot size then there is some additional energy gain as the drive beam now propagates further. The blue line in Fig. 3.23(a) shows the energy spectrum of two beams at s = 171.3 cm where the acceleration terminates. The energy gain of the trailing beam increases to around 10 GeV due to the reduced the beam head erosion rate. This is a factor of 5 improvement in energy gain compared with the case of no pre-plasma, but still only one third of the energy gain with full pre-plasma.

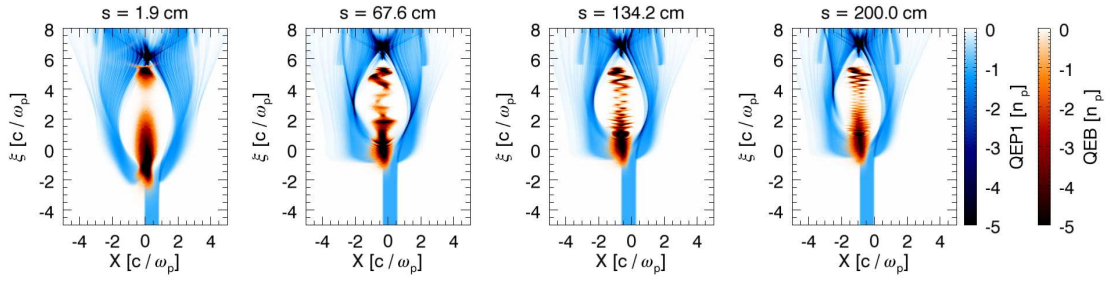

Figure 3.24: Snapshots of beam and plasma densities from a simulation where the laser precursor drifts to the left in the rest frame of the beam.

Although the energy gain on the trailing beam has indeed been increased over the case with no pre-plasma by employing the plasma filament in Li, the energy

spread is no better and is much worse than when a fully pre-formed plasma is used. This is because the drive beam is simply not intense enough to ionize the plasma to the distance of one R_b (as shown in Fig. 3.22(a)), which is necessary to form a nice ion cavity as it does in the completely pre-ionized case discussed above. However if one now uses Rb or Cs instead of the Li the same drive beam can ionize a plasma column out to a larger radius for the same beam parameters and form a wake that resembles the wake formed in a completely pre-ionizd plasma. Figure 3.22b shows the density plot of the same two-bunch PWFA case but in a field ionized Cs plasma. Compared with Fig. 3.22(a), the plasma wake shows an ion cavity clearly enclosed by the electron sheath in Cs than that in Li. Most of the trailing bunch is now inside the bubble.

Fig. 3.23(b) shows the energy spectra of the same beams using field ionized Cs plasma (the green line). Now, the acceleration length has increased to 76.2 cm, which is longer than the 16.7 cm observed in Li. The energy gain of the trailing beam is consequently increased to 5 GeV (from 2 GeV value for Li) and the energy spread is narrower. Now when one uses a 10 μm radius plasma filament in front of the Cs plasma the acceleration length reaches 200 cm. From the energy spectrum (the blue line in Fig. 3.23(b)), one can see that the energy gain of the trailing beam is around 20 GeV and the FWHM energy spread of the trailing beam is around 3%.

When using the laser precursor to ionize the plasma filament in front of the beam, the alignment accuracy between the laser precursor and the drive beam will affect the acceleration. We have explored the effect of an alignment error via a simulation that has a 10 μrad angle between the propagation directions of the laser precursor and the drive beam. At the entrance of the plasma, the center of the laser precursor pulse is offset by 10 μm (which is equal to the electron beam spot size) from the center of the drive beam. Since the laser precursor propagates with an angle to the drive beam, the plasma filament ionized by the laser will

drift at a small speed (which is 10 μm for every meter the laser propagates when the angle is equal to 10 μrad) along the transverse direction in the rest frame of the beam. The density snapshots from the simulation are shown in the Fig. 3.24.

Although there is a misalignment between the laser precursor and the drive electron beam, the acceleration still lasts for 200 cm. The final energy gain on the trailing beam is almost the same as that with the aligned laser precursor. But as the laser pulse and therefore the plasma filament drift to the left in the simulation box, the drive beam as well as the trailing beam also drift to the left together with the plasma filament. This appears to strongly seed the hosing instability on the beams, especially on the trailing beam. In the experiments, the hosing motion of the trailing beam will cause particle loss as the beam propagates between the plasma exit and the spectrometer. The hosing motion of the beam will also generate more betatron radiation. In fact alignment accuracy of the laser pulse and the electron beams can be optimized in the experiments by monitoring the betatron x-ray radiation coming out of the plasma. When the laser and the drive beam are aligned, the radiation will reach its smallest value.

It should also be pointed out that when we use a neutral gas with lower ionization threshold such as Cs or Rb, the second ionization threshold becomes smaller as well. In section 2, we have showed that the second ionization threshold for Cs is 51.8 GV/m, which is close to the electric field magnitude of the plasma wake. Therefore, it is possible that the second ionization of Cs occurs under some situations. If this happens inside the plasma bubble, the plasma wake field may trap the ionized electrons and accelerate them into a high energy. But the number of the electrons produced from the second ionization is much less than that of the trailing beam. So the acceleration of the trailing beam should not be affected in this case. In other cases with more dense and shorter drive beams propagating in a higher density plasma, this additional ionization of the second electron inside the wake can act as a source of dark current that depletes the energy from the

wake [74].

3.6 Summary

In this chapter, we reviewed the theory for the nonlinear plasma wake fields driven by an intense electron beam. The bubble-like plasma wake is perfect for focusing and accelerating the electron beam. The electron beam inside the plasma wake will lose or gain energy in the longitudinal electric field of the plasma wake. The decelerating field of the plasma wake driven by different electron beams (with Gaussian profiles) were obtained through QuickPIC simulation. It was found that the decelerating field is approximately equal to $\Lambda/\sqrt{e}k_p\sigma_z$ for $k_p\sigma_z$ in a range centered near 3. We also analyzed the optimum plasma density for achieving the largest accelerating field in an electron-beam-driven PWFA. It was found that the peak beam current I_p (charge per unit time) plays an important role in determining the optimum density. For the relativistic blowout regime ($\Lambda \geq 1$), the optimum plasma density is $n_o = n_{b0}$, where n_{b0} is the peak beam density, as long as $1 \geq \sigma_r/\sigma_z \geq 1$. We also showed the two-bunch PWFA simulation results using QuickPIC. We studied what was feasible at FACET and found that 30 GeV energy gain over two meter with a 3% energy spread was psossible in a preformed plasma. However, for FACET parameters, the ionization-induced beam head erosion affects the drive beam's ability to ionize the neutral gas and therefore form the wake and thus terminates the acceleration process even though the drive beam still contains much energy. We devised effective strategies for mitigating the drive beam head erosion in a PWFA that employ a low energy laser to pre-ionize a narrow column plasma as to guide the head of the beam and relies on beam self-fields to produce the bulk of the plasma. We found that head erosion can indeed be mitigated by employing a combination of lower ionization threshold gas and a laser-produced plasma filament in front of the drive beam. These strategies

will be employed in the upcoming two-bunch PWFA experiments on the FACET facility.

CHAPTER 4

Simulations of PWFA Linear Collider Stages

As discussed in chapter 3, the two-bunch PWFA is a promising scheme for building a future linear collider (LC) while experiments at FACET are aimed at studying key aspects of PWFA. The parameters of the FACET experiments differ from those required in a future LC in several important aspects. Most importantly, the normalized emittance of the trailing beam needs to be much smaller. In order for the emittance growth to be minimized, the beam's spot size needs to be "matched" to the focusing force of plasma wake. For a "matched" beam, the vacuum diffraction length, β^*, equals the beam's betatron wave length [75]. For the small emittances needed in a LC, the matched spot sizes are sub 100 nm. As a result, the self-fields of the beam are very intense. In fact, it has been shown [76] that they are intense enough to pull the massive plasma ions inward during the transit time of the short bunch, and this modifies the wake fields felt by the bunch. Therefore, ion motion needs to be included in the simulations.

In this chapter, we will present QuickPIC simulations of a two-bunch PWFA design including the plasma ion motion. We use the beam parameters similar to the PWFA-LC design [77]. The QuickPIC simulations are performed with a resolution that resolves the matched beam spot size for the first time. In section 4.1, we will introduce the PWFA-LC concept and the related plasma ion motion issue. In section 4.2, we will discuss the computing requirements and the work we have done on QuickPIC to enable it to perform the PWFA-LC simulations. In section 4.3, we present the simulation results of a PWFA-LC case including the

plasma ion motion. The evolution of the trailing beam's emittance is discussed in section 4.4. In section sec4-5, we summarize the results and discuss areas for future work.

4.1 The concept of PWFA-LC

The PWFA-LC uses the PWFA as the main accelerator to obtain electron (or positron) beam(s) for collision experiments. In a future linear collider design, the final goal for the main accelerator is to deliver electron or positron beams with enough energy (500 GeV or greater) as well as enough luminosity (on the order of $10^{34}\,\mathrm{cm}^{-2}\cdot\mathrm{s}^{-1}$) in order to meet the requirements for studying the desired physics. In addition, the accelerator must be able to operate at a high power transfer efficiency from the power source to the main beams which collide. Table 4.1 (which is taken from reference [77]) shows the key parameters of a conceptual PWFA-LC.

In Table 4.1, we can see that the loaded acceleration gradient is 25 GeV/m in each plasma cell. And the plasma cell is 1 meter long. Therefore, the final energy (500 GeV or up) of the main beam can be achieved by staging multiple two-bunch PWFA stages (i.e., plasma cells). Reference [78] provides another conceptual design of a PWFA-LC. Although the basic concept is the same in references [77] and [78], the drive beam and plasma parameters are different. Figure 4.1 (taken from reference [78]) shows an schematic plot of modified PWFA-LC design. The collision energy in both PWFA-LC designs is 1 TeV (each of the electron and positron beams has 500 GeV). In the new design [78], the entire accelerator is roughly 4.5 km in length, which is dominated by the beam final focusing and delivery system (3.5 km long as shown in Fig. 4.1). The designed accelerating gradient in the PWFA stage is 1 GeV/m (which is less than that in reference [77]), the main accelerators (for accelerating the main electron and positron beams) are

Main beam: bunch population, bunches per train, rate	1×10^{10}, 125, 100 Hz
Total power of two main beams	20 MW
Drive beam's energy	25 GeV
Drive beam's peak current	2.3 A
Drive beam's active pulse length	10 μs
Main beam emittances, x, y	2, 0.05 mm $\cdot$ mrad
Main beam sizes at Interaction Point, x, y, z	0.14, 0.0032, 10 μm
Luminosity	$3.5 \times 10^{34}\,\mathrm{cm}^{-2} \cdot \mathrm{s}^{-1}$
Luminosity in 1% of energy	$1.3 \times 10^{34}\,\mathrm{cm}^{-2} \cdot \mathrm{s}^{-1}$
Average power of the drive beam	58 MW
Plasma density	$1 \times 10^{17}\,\mathrm{cm}^{-3}$
Accelerating gradient	25 GeV/m
Plasma cell length	1 m
Power transfer efficiency drive beam⇒main beam	35%
Efficiency: Wall plug⇒RF⇒drive beam	$50\% \times 90\% = 45\%$
Overall efficiency and wall plug power for acceleration	15.7%, 127 MW
Site power estimate	170 MW

Table 4.1: The key parameters of a conceptual PWFA-LC design [77].

both 0.5 km long. In reference [77], the acceleration gradient in each cell is $\sim 25\,\mathrm{GeV/m}$ and each cell is 1 meter long. In both cases, the main beam will obtain 25 GeV energy from each PWFA stage and each main accelerator consists of 20 PWFA stages. All the PWFA stages for accelerating the main electron and positron beams use an electron beam as the drive beam. Note that in our opinion there has not been an established method for accelerating a positron beam using plasma-based acceleration. Several methods have been proposed [79, 80], and further investigation is ongoing. The drive beams are delivered by a continuous wave (CW) superconducting radio frequency (RF) recirculating linac, which can provide an excellent power efficiency together with a high flexibility in the number of bunches[78]. The main electron and positron beams are generated separately through additional linacs.

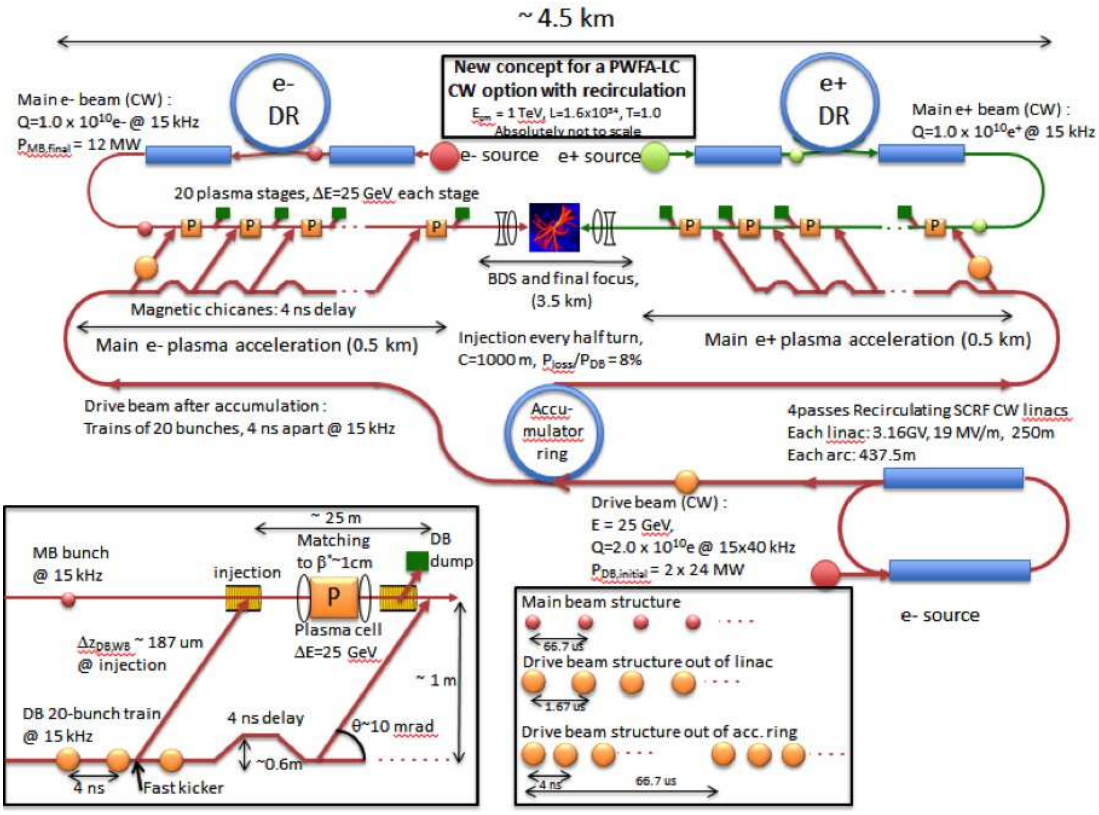

Figure 4.1: Conceptual design of a 1 TeV PWFA-LC[78].

Besides the high accelerating field, a high power transfer efficiency should also be achieved within each PWFA stage. In the two-bunch PWFA, the drive beam will lose its energy because of the decelerating field in the plasma wake. As shown in the chapter 3, the deceleration is not uniform along the longitudinal direction. It will reach a maximum value around the beam center (the beam has a Gaussian density profile). The drive beam energy depletion length is $k_p L_d = \gamma / E_{z,dec}$, where γ is the Lorentz factor of each particle in the drive beam and $E_{z,dec}$ is the maximum decelerating field (in normalized units). Therefore, only the beam particles feeling the maximum decelerating field will lose all their energy at the depletion length, while many other particles still have energy. This leads to a lower efficiency. In order to maximize the efficiency, the ideal situation is that every drive beam particle loses energy at the same rate. Therefore, a locally uniform decelerating field in the plasma wake is desirable to enhance the efficiency of the drive beam's energy depletion. This can be achieved by modifying the longitudinal density profile of the drive beam into a linearly rising ramp, which has been discussed in chapter 3, section 3.2. Such a drive beam profile can lead to a uniform decelerating field equal to Λ_0 / L_0, where Λ_0 is the peak normalized charge per unit length and L_0 is the beam length. Shaping the trailing beam can also enhance the efficiency for the trailing beam to extract energy from the plasma wake (i.e., the beam loading efficiency). In reference [67], it was found that in the relativistic blowout regime (where the beam has $\Lambda \geq 2$), the beam loading efficiency can be maximized by using a trailing beam with a trapezoidal density profile. Note that this is obtained under the condition of minimizing the energy spread of the trailing beam (i.e., flattening the accelerating field E_z through the beam loading effect). More interestingly, the maximum beam loading efficiency was found to be a constant no matter where you load the trailing beam in the acceleration phase of the plasma wake field, which implies that for larger loaded accelerating fields felt by the trailing beam, less total charge can be accelerated, i.e., $E_{acc} Q_{beam}$ is

constant. In reference [81], a high efficiency two-bunch PWFA case was shown. In that case, both the drive electron beam and the trailing electron beam have shaped longitudinal density profiles. The trailing beam has a trapezoidal profile as [67] suggested while the drive beam has a linearly rising ramp (with the head of the beam cut off) combined with a density spike at the beam front. Figure 4.2 (taken from reference [81]) illustrates this scenario. In this case, the efficiency of the energy transfer from the drive beam to the trailing beam reaches 51%, which satisfies the requirement in Table 4.1. At the same time, the FWHM energy spread of the trailing beam is limited to less than 0.5%.

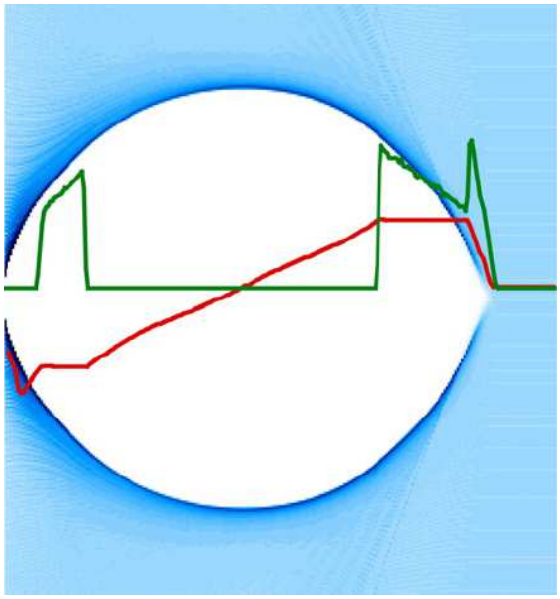

Figure 4.2: The on-axis line-out of the drive and trailing beam's density profiles (green curve) and the longitudinal accelerating field (red curve) produced by these beams. The plasma electron density is on the background in blue [81].

A future LC also requires high beam luminosity. This is achieved by focusing a low emittance beam to a transverse size on the order of 1 nm at the final interaction point. Based on existing final focus designs, this requires that at the final focus the beam should have small emittance. For example, as shown in Table 4.1, the trailing beam's (i.e., the main beam) emittance in the conceptual design is

$2\,\mathrm{mm}\cdot\mathrm{mrad}$ and $0.05\,\mathrm{mm}\cdot\mathrm{mrad}$ in the two different transverse directions. In a two-bunch PWFA stage, a trailing beam with a small transverse emittance, e.g. $0.1\,\mathrm{mm}\cdot\mathrm{mrad}$, will have a matched spot size on the order of 100 nm in the nonlinear plasma wake. The matched spot size is the spot size of the beam at the equilibrium state when propagating in the plasma wake. The transverse equilibrium state of the beam occurs when the focusing force balances the expansion of the beam due to the emittance. As described in Chapter 3, the focusing force $E_r - B_\theta$ (in normalized units) from the nonlinear plasma wake driven by an intense electron beam is exactly $r/2$ within the bubble. By looking at the Vlasov equation of the equilibrium transverse distribution function of the beam, we can easily obtain the matched spot size of a Gaussian beam [75],

$$\sigma_{r,matched} = \left(\frac{2m\epsilon_N^2}{\gamma}\right)^{\frac{1}{4}},$$

where m is the mass of the beam particle, ϵ_N is the normalized beam emittance and γ is the Lorentz factor of the beam particle. Note that all the quantities in the above equation are in normalized units. A useful engineering formula for the electron beam is

$$\sigma_{r,matched}[\mu\mathrm{m}] = 7.33\left(\frac{\epsilon_N^2[\mathrm{mm}\cdot\mathrm{mrad}]}{E[\mathrm{GeV}]n_p[10^{16}\mathrm{cm}^{-3}]}\right)^{\frac{1}{4}},$$

where n_p is the plasma density and E is the beam energy. Therefore, the matched spot size is proportional to the square root of ϵ_N and inversely proportional to the fourth square root of the energy. For a beam with a normalized emittance of $0.1\,\mathrm{mm}\cdot\mathrm{mrad}$ and an energy of 25 GeV, the matched spot size of the beam is around $0.1\,\mu$m in a $1.0\times10^{17}\,\mathrm{cm}^{-3}$ plasma. For an energy of 500 GeV, the matched spot size is $\sim 50\,$nm.

In reference [76], a simple method for estimating the severity of the ion motion was given by calculating the plasma ion motion in the Coulomb field close to the beam. Assuming the beam has a transverse flat-top density profile with a spot

size σ_r, the Coulomb field E_r close to beam (say $r < \sigma_r$) is

$$E_r = \frac{n_b r}{2},$$

where n_b is the beam density. Note that we still use the normalized units. Then assuming beam fields dominate over the plasma fields, the equation of a plasma ion is

$$m_{ion}\frac{d^2 r}{d\xi^2} + \frac{Z n_b}{2} r = 0,$$

where Z is the ion charge state and we assume the plasma ion motion is non-relativistic and the ions have $v_\phi = 0$. This equation implies that the ions close to the beam will oscillate around the axis and the oscillation wave number with respect to ξ is $k_{ion} = \sqrt{\frac{Z n_b}{2 m_{ion}}}$. Therefore, the total phase advance of the ion within the duration of the beam pulse length (which is equal to the transit time of the beam passing by an ion) is

$$\Delta\phi \approx k_{ion}\sigma_z.$$

For most of the cases we interested, the beam pulse length is on the order of the plasma skin depth $k_p\sigma_z \sim 1$. Thus,

$$\Delta\phi \approx \frac{k_{ion}}{k_p} k_p\sigma_z \approx \frac{k_{ion}}{k_p} = \sqrt{\frac{Z n_b}{2 m_{ion}}},$$

since $k_p\sigma_z \sim 1$. Because the beam density is normalized by the plasma density and the mass of the plasma ion is normalized by the rest mess of the electron, the phase advance of the ion becomes

$$\Delta\phi \approx \sqrt{\frac{Z n_b m_e}{2 n_p m_{ion}}}. \tag{4.1}$$

Although the self-field of the plasma electrons and ions are not included in the above derivation, we can still expect significant ion motion when $\Delta\phi \gg 1$. According to the equation (4.1), $\Delta\phi \gg 1$ will occur when the beam-plasma density ratio is much larger than the plasma ion-electron mass ratio.

In linear collider designs, the beams have elliptical spots. For simplicity we consider round beams with the same r.m.s. spot size in both transverse directions. With a spot size of $0.1\,\mu$m (which is the matched spot size for a beam emittance equal to $0.1\,\text{mm}\cdot\text{mrad}$ in a $1.0\times10^{17}\,\text{cm}^{-3}$ plasma), the trailing beam's peak density will be 6.35×10^{4} times larger than the plasma density (which is $1.0\times10^{17}\,\text{cm}^{-3}$), if the trailing beam contains 1×10^{10} electrons and the pulse length is $10\,\mu$m (the same parameters as shown in Table 4.1). This ratio is much larger than the plasma ion-electron mass ratio 1.27×10^{4} for a Li plasma. Therefore, we must consider the plasma ion motion for the existing PWFA-LC designs.

In previous work [76, 82, 83], the plasma ion motion in PWFA was analyzed using reduced theoretical models and methods for mitigation of the ion-motion-induced emittance growth were also proposed. However, to date no fully self-consistent simulations have been performed, which study the actual emittance growth due to ion motion inside a wake for PWFA-LC parameters.

4.2 Code preparation for the full scale PWFA-LC simulation

For the PWFA-LC design in reference [77], there are a few big differences from the two-bunch PWFA in FACET experiments discussed in the last chapter. The main difference is that the main electron beam (i.e., the trailing beam) has a very small emittance, which is on the order of $0.1\,\text{mm}\cdot\text{mrad}$. This will result in a matched beam spot size on the order of 100 nm in a $1.0\times10^{17}\,\text{cm}^{-3}$ plasma (for a 25 GeV trailing beam). Therefore, in order to include the ion motion that results for such a tightly focused beam, we must at a minimum resolve the 100 nm beam spot size in the PIC simulation. The simulation box usually has a much larger transverse scale so as to contain the entire bubble-like plasma wake. Normally, the maximum bubble radius of the plasma wake driven by an intense electron beam is several

times the plasma skin depth ($\sim 100\,\mu$m). A simulation box with a transverse size of $400 \times 400\,\mu\text{m}^2$ is therefore needed for the PWFA-LC case. Thus, we need at least $8000 \times 8000 \times 1000$ cells for the PWFA-LC simulations to have at least 2 cells per σ_r. Such a simulation cannot be done by using a full PIC code like OSIRIS since the resulting number of time steps is around 2×10^7 and around 1 billion cpu-hours are needed for a single simulation (for 1 meter long plasma).

The quasi-static PIC code QuickPIC is currently the only 3D code that can simulate the PWFA case with such a fine resolution. With the new algorithm described in Chapter 2, QuickPIC 2.0 will only need around 1 million cpu-hours to simulate a PWFA-LC case for 1 meter long acceleration using a proper resolution. In addition, we can decrease the computing time by making further assumptions.

In a two-bunch PWFA with PWFA-LC beam parameters, only the trailing beam has the extreme parameters that will cause significant plasma ion motion. The drive beam can therefore have a larger emittance and larger matched spot size. Although the drive beam will evolve as it propagates inside the plasma, until the drive beam has nearly stopped, the plasma wake driven by the drive beam will hardly change. As we will show, the trailing beam's emittance evolves only during a short initial time. Therefore, we can make a further assumption that the drive beam does not evolve while studying the emittance growth. The evolution of the trailing beam and how the plasma wake (including the ion motion) is affected by the trailing beam are what we are really interested in.

In QuickPIC, the plasma particles (electrons and ions) all stay in a 2D slice (with the same coordinate of ξ). They are advanced step by step along ξ. At each ξ step, the plasma particle information and the electromagnetic fields within the slice can be considered as the initial value for the next ξ step. After this plasma slice sweeps over all the ξ steps in the simulation box, the particle beams will be pushed one step forward in s according to the fields obtained from the plasma response. Then all the procedures will start over with a re-initialized plasma slice

at the "origin" ξ (largest value for ξ). For example, Figure 4.3(a) shows results from the same simulation of a two-bunch PWFA as was shown in Figure 3.2(a). In this simulation, the 2D plasma slice is swept from $\xi = 7.5$ to $\xi = -10$ (the center of the drive beam is at $\xi = 0$). In a normal simulation, both the beams are pushed forward in s using the calculated plasma wake field and the 2D plasma slice is then swept over the two beams again. If we assume the drive beam does not evolve, then in every 3D step when the plasma slice reaches $\xi = -5$ (which is the end of the drive beam and the starting point of the trailing beam), all results should be the same. Therefore, we do not need to calculate the plasma response from $\xi = 7.5$ to $\xi = -5$, if we assume the drive beam is a non-evolving beam. We need to calculate the wake fields for $-5 < \xi < 7.5$ only once (as shown in Figure 4.3(b)), and then store all the information in the slice at $\xi = -5$, including the plasma particles positions and velocities as well as the electromagnetic fields. We then start to simulate the region $\xi < -5$ including the evolution of the trailing beam for the desired number of 3D time steps. The trailing beam will be updated at a proper 3D time step as usual. The only difference is that the plasma particles and the electromagnetic field at the first slice (where $\xi = -5$ in the example shown in Figure 4.3(c)) will be initialized using the stored data. As a result, the amount of calculation can be reduced by a factor of ~ 4 since we do not need to include the drive beam in the simulation. The stored plasma and field data in the 2D slice can be used for simulating any trailing beam evolution. It is a time-saving method for the trailing beam parameter scanning. In the following sections, all the simulations were performed using this method.

4.3 The plasma ion motion in a PWFA-LC case

In this section, we will present the simulation results of a two-bunch PWFA in a Li plasma using the PWFA-LC main beam parameters of reference [77]. The

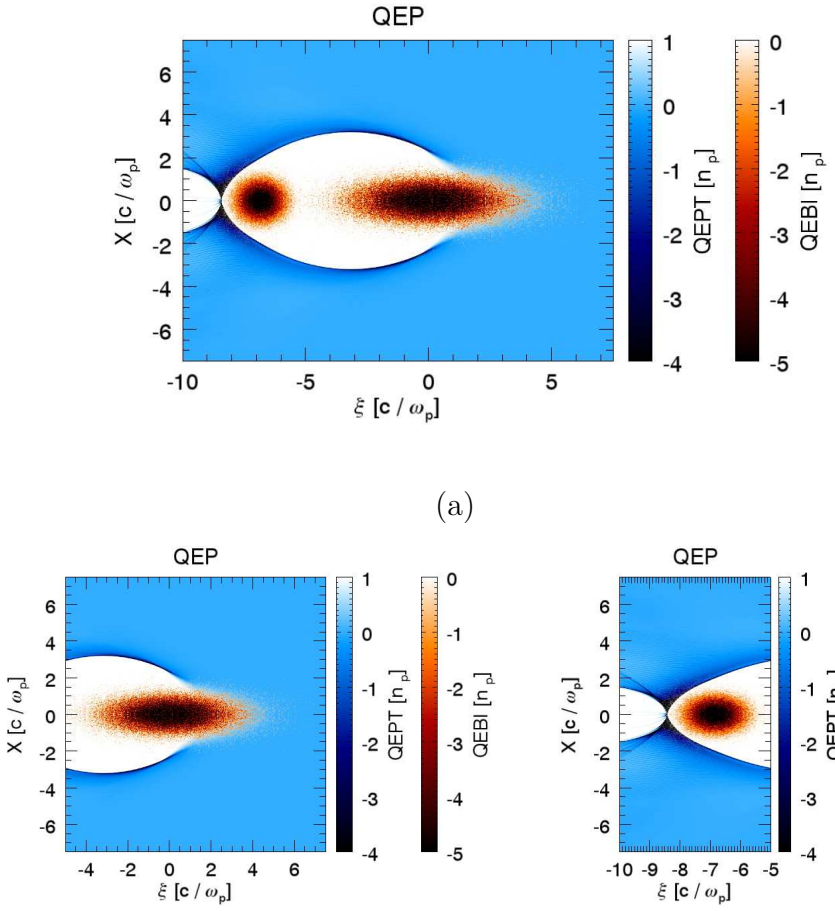

Figure 4.3: Illustration of plasma response from the middle of the simulation box: (a) for the whole simulation box;(b) for a non-evolving drive beam;(c) for a simulation with only a trailing beam using the stored information of the plasma slice.

Li ion has a mass equal to $12852m_e$ (for simplicity we assume singly ionized Li and in the future we will include the additional ionization from the self-fields of the trailing beam). We assume the drive beam does not evolve in the simulation. The drive beam contains $N = 3.0 \times 10^{10}$ electrons and has an initial energy of 25 GeV. For simplicity we use a Gaussian profile (not the optimized profile for high efficiency) and the r.m.s. spot size of the beam is $\sigma_r = 1\,\mu$m. The r.m.s. pulse length of the beam is $\sigma_z = 30.0\,\mu$m. The transverse normalized r.m.s. emittance of the beam is $\epsilon_N = 10\,\text{mm}\cdot\text{mrad}$. We calculate the plasma response untill the slice located at $85\,\mu$m after the drive beam's center. The stored information at that slice is used for the simulation that only includes the trailing beam. The trailing beam contains $N = 1.0 \times 10^{10}$ electrons and has an initial energy of 25 GeV. It also has a Gaussian profile (not an optimized profile) and the r.m.s. spot size of the beam is $\sigma_r = 100\,nm$. The r.m.s. pulse length of the beam is $\sigma_z = 10.0\,\mu$m. The transverse normalized r.m.s. emittance of the beam is $\epsilon_N = 0.093\,\text{mm}\cdot\text{mrad}$. The distance between two beams centers is $115\,\mu$m (i.e., the trailing beam's center is $30\,\mu$m away from the simulation box boundary at the front). The initial plasma density is $1.0 \times 10^{17}\,\text{cm}^{-3}$, so $k_p\sigma_r = 5.94 \times 10^{-3}$. The simulation box is $400\,\mu\text{m} \times 400\,\mu\text{m} \times 59\,\mu$m in size. There are $8192 \times 8192 \times 512$ cells in the simulation box. Therefore the size of each cell is $48.83\,nm \times 48.83\,nm \times 115.23\,nm$. The time step for pushing the trailing beam particles is $5\,\omega_p^{-1}$. We use 4 ions per cell, which corresponds to only ten times fewer ions than the number of the real plasma ions within the cell volume.

Figure 4.4(a) shows a 3D surface plot of the plasma ion density (in the 2D $x-\xi$ plane) after the trailing beam propagated 9.33 cm inside the plasma. The plasma ion density has a large perturbation within the region $|k_p x| < 0.1$. Outside this region, the plasma ion density remains almost unchanged. This is because only the plasma ions close to the trailing beam can feel the strong Coulomb field, and in the region of $|k_p x| > 0.1$ the Coulomb field of the beam is not strong enough

to move the plasma ions. At different transverse positions (x), the Coulomb field around the trailing beam has a maximum value at the beam center (in these simulations $\xi = 0$ is now defined to be the center of the trailing beam). From the longitudinal line-outs of the plasma ion density (shown in Fig. 4.4(c)), we can see that the on-axis line-out (at $x = 0$) rises quickly around the beam center (where $\xi = 0$) and reaches its maximum value after the beam center at around $\xi = 0.5$. The line-outs in the transverse direction (Fig. 4.6(b)) show the plasma ions are attracted by the tightly focused trailing beam and form a density peak around the axis. After reaching the maximum density, the plasma ions spread out, and the maximum density decreases.

The ion motion will affect the plasma wake. Figure 4.5(a) shows a 3D surface plot of the focusing force (which is $E_x - B_y$ in the $x - \xi$ plane) in the plasma wake at $s = 9.33\,\mathrm{cm}$ (the same time as Fig. 4.4). From this plot, we can see that in the region of $|k_p x| > 0.3$ the focusing force is not affected very much by the ion motion as compared with the plasma wake when no ion motion is considered (recall that the focusing force within the bubble is equal to $r/2$ without any plasma ion motion). But the focusing force has large modulation within the region $|k_p x| < 0.3$ (recall that $k_p \sigma_r \sim 0.01$). The transverse line-outs of the focusing force (Fig. 4.5(b)) shows that the slope of the focusing force in the transverse direction converges to $k_p x/2$ when $|k_p x| > 0.3$ and becomes much larger than $1/2$ on the axis. The on-axis slope also grows along the ξ direction and becomes steepened after the beam center. From the longitudinal line-outs (Fig. 4.5(c)), we can see that the focusing force cannot remain uniform along the ξ direction within the region close to the axis (say $|k_p x| < 0.3$). When $|k_p x|$ is larger, the focusing force becomes uniform along ξ, which is similar to that of the plasma wake without the ion motion. The focusing force within the beam is therefore no longer perfectly linear and constant in ξ. As a result, the matched beam will no longer have a Gaussian distribution in the transverse direction, and will have

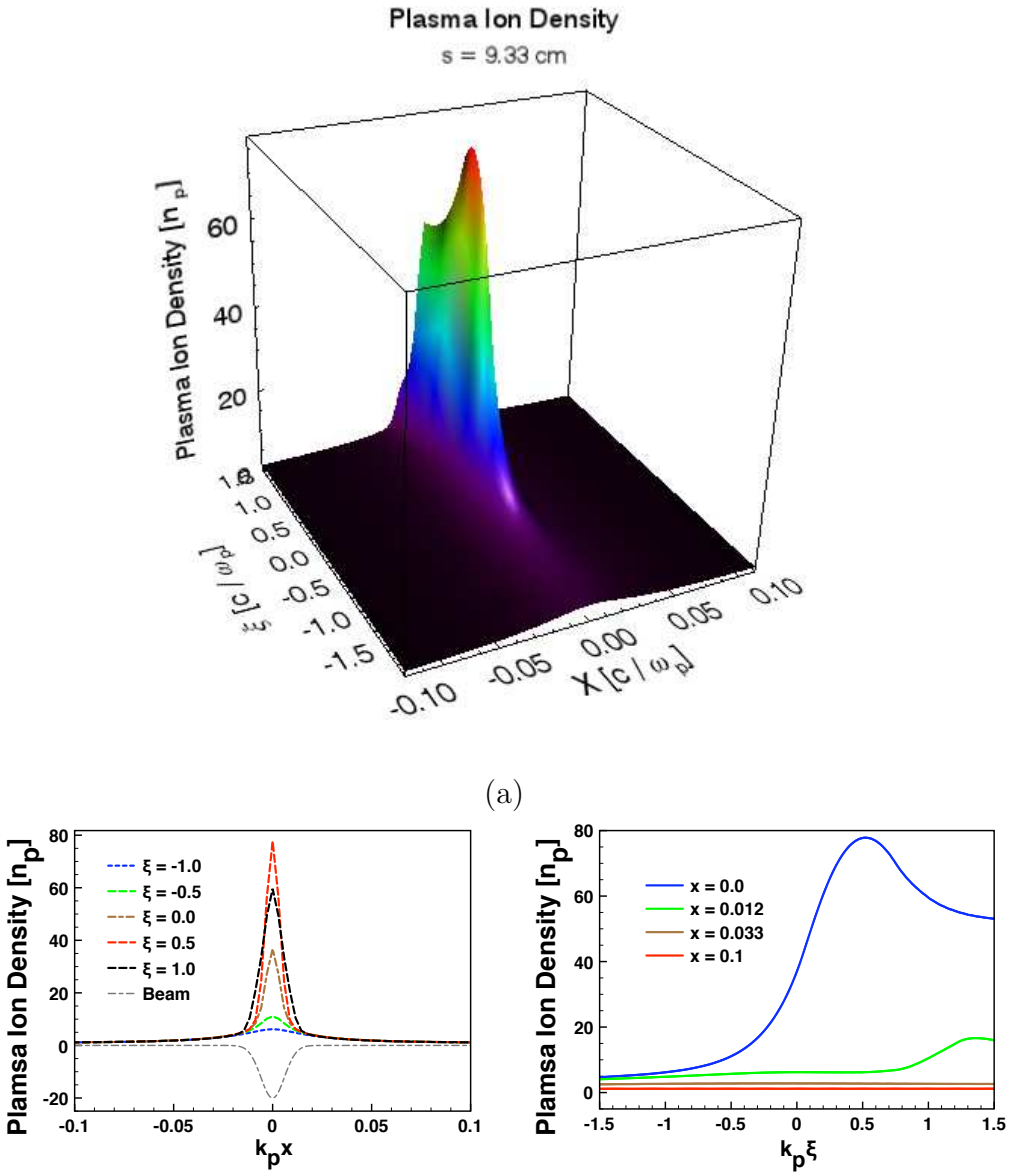

Figure 4.4: A snapshot of the plasma ion density in the $x-\xi$ plane at $s = 9.33\,\mathrm{cm}$: (a) A 3D surface plot;(b) Line-outs along the transverse (x) direction together with the trailing beam's transverse profile using arbitrary units for the beam density;(c) Line-outs along the longitudinal (ξ) direction.

a smaller "matched" spot size which will depend on ξ. As the beam evolves, its emittance will therefore increase and we will discuss this shortly.

In contrast to the significant modulation of the focusing force in the region close to the beam axis, the accelerating field E_z remains relatively unchanged. This can be seen from Figure 4.6. Figure 4.6(a) shows the 3D surface plot of E_z in the $x-\xi$ plane at $s = 9.33$ (the same time step as Figures 4.4 and 4.5). The E_z is flattened by the trailing beam because of the beam-loading effect. This is good for maintaining a small energy spread in the trailing beam. Although the plasma ions move drastically in the region close to the axis, the E_z field still remains uniform along the transverse direction within the bubble of the plasma wake. Only a very small perturbation can be seen in the transverse line-out at $k_p\xi = 0.5$ (as shown in Fig. 4.6(b)). This means that the acceleration of the trailing beam particles will not be affected much when ion motion occurs.

This can also be seen from equationg (3.1). The first term in equation (3.1) is from the plasma electrons in the sheath while the second term is due to the plasma ions. When the ions move, we can approximate the second term as $K(\xi)\frac{r^2}{4}$, where $K(\xi)$ is chosen such that the focusing force is $K(\xi)\frac{r}{2}$. The accelerating field is now

$$\left.\frac{\partial\psi}{\partial\xi}\right|_{r=0} \approx \frac{r_b}{2}\frac{dr_b}{d\xi} - \frac{dK}{d\xi}\frac{r}{2} \approx \frac{r_b}{2}\frac{dr_b}{d\xi},$$

which is the same result as for stationary ions.

4.4 The evolution of the trailing beam

The ion-motion-induced modulation of the plasma wake will affect the evolution of the trailing beam mainly in the transverse direction since the accelerating field of the plasma wake does not change very much. As described in section 4.1, the most important issue appears to be how the emittance of the trailing beam evolves in this situation. In this section, we will present QuickPIC simulation results of

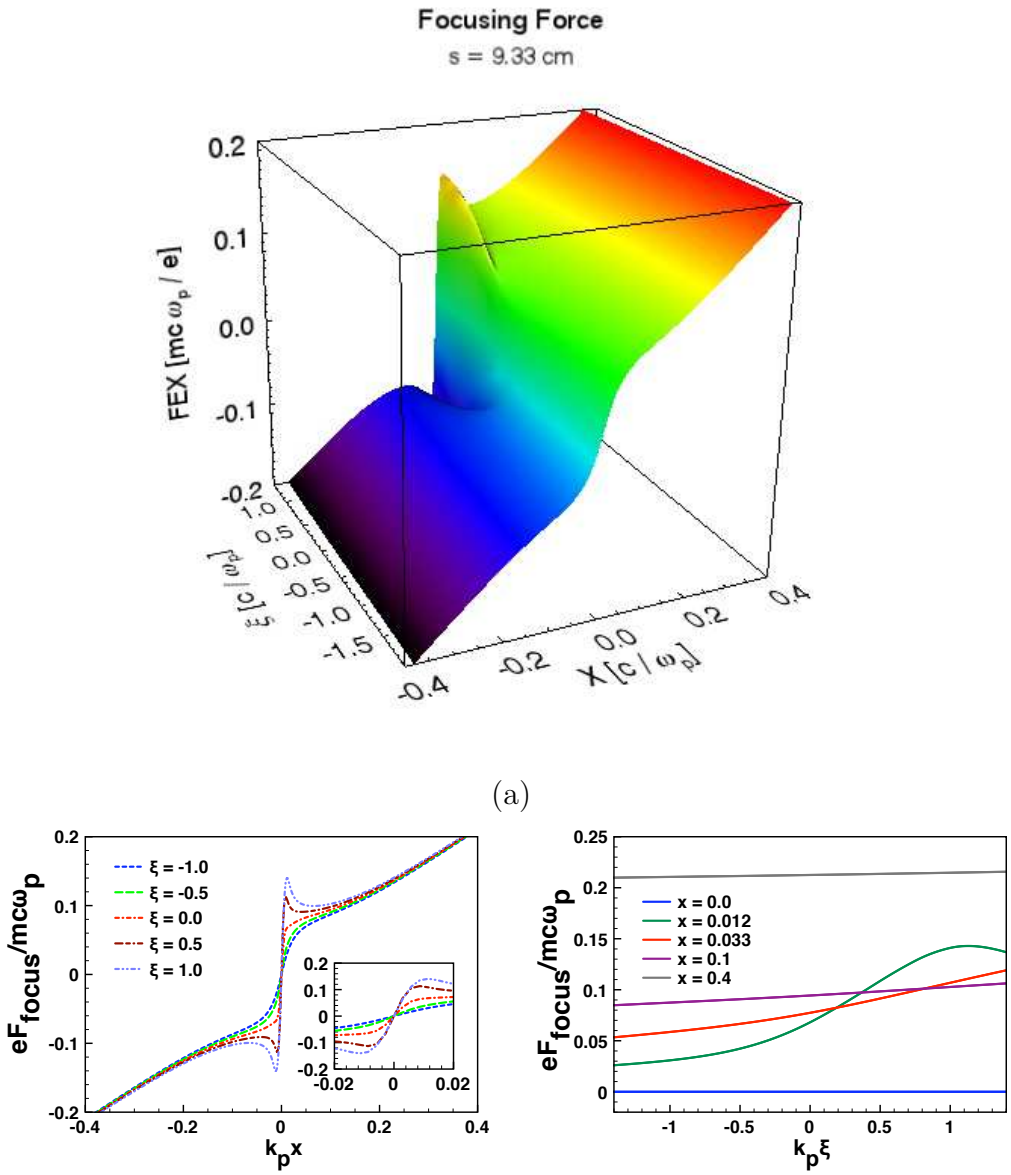

Figure 4.5: A snapshot of the focusing force in the $x-\xi$ plane at $s = 9.33\,\mathrm{cm}$: (a) A 3D surface plot;(b) Line-outs along the transverse (x) direction together with a zoom-in plot in the range $-0.02 < k_p x < 0.02$;(c) Line-outs along the longitudinal (ξ) direction.

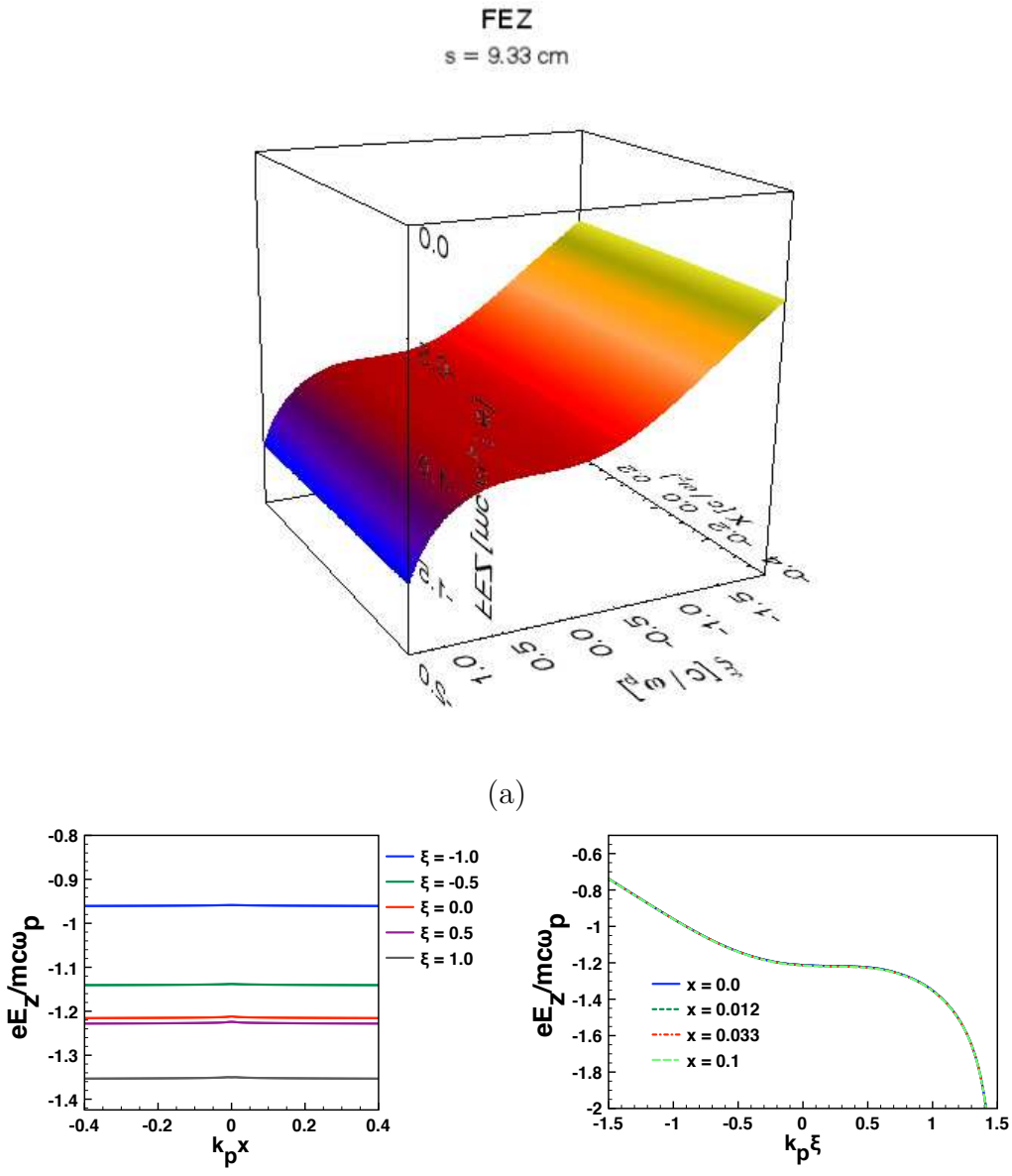

Figure 4.6: A snapshot of the plasma ion density in the $x-\xi$ plane at $s = 9.33\,\mathrm{cm}$: (a) A 3D surface plot;(b) Line-outs along the transverse (x) direction;(c) Line-outs along the longitudinal (ξ) direction.

the evolution of the trailing beam's emittance and spot size.

We will use the same drive beam parameters as in section 4.3 (Gaussian beams) and still assume the drive beam does not evolve in the plasma. The simulation resolution is also kept the same. We first simulate the same trailing beam as in secion 4.3 but do not include the plasma ion motion. In this case, the trailing beam should feel a focusing force equal to $r/2$, and its normalized emittance should be conserved. Figure 4.7(a) shows the trailing beam's emittance evolution in the first 20 cm of propagation inside the plasma, and the emittance is preserved at the initial value of $0.093\,\mathrm{mm}\cdot\mathrm{mrad}$. This also implies that QuickPIC is a high fidelity tool for studying the evolution of the beam emittance for highly relativistic beams. The spot size of beam oscillates around a central value with a small amplitude, and the central value gradually decreases as the beam is accelerated at a slow rate shown in Figure 4.7(b). This is because as the trailing beam gains energy from the plasma wake, the matched spot size decreases adiabatically. In addition, there is a small oscillation.

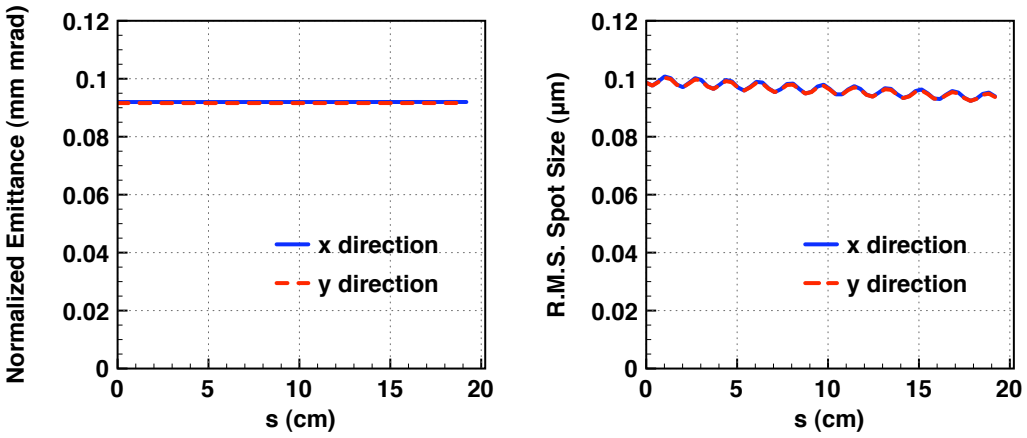

(a) (b)

Figure 4.7: The evolution of the trailing beam's (a) normalized emittance and (b) spot size. The ion motion is not included in the simulation.

When the plasma ion motion is turned on in the simulation, the trailing beam

evolves differently. As shown in Figure 4.8(a), the trailing beam's emittance increases rapidly in the first 2 cm of propagation, and reaches an equilibrium value of around $0.2\,\mathrm{mm}\cdot\mathrm{mrad}$, which is twice as large as the initial value. Although the emittance is increasing, the beam's spot size (shown in Fig. 4.8(b)) experiences a damped oscillation in the first 2 cm and finally reaches an equilibrium value of around $0.07\,\mu\mathrm{m}$, which is 70% of the initial value (Note that this is exactly the same simulation as in the section 4.3, other than the inclusion of ion motion). Therefore, the entire trailing beam is tightly focused within a small region, say $r < 0.2\,\mu\mathrm{m}$ (i.e., $k_p r < 0.012$). As shown in Fig. 4.5, this is the region with a steepened slope of the focusing force, and the on-axis slope changes along the ξ direction. Thus, it would be useful to check the emittance of the trailing beam's particles at different slices of ξ (note that the trailing beam's particles barely move in ξ (no phase slip) because they all move at a speed very close to c), instead of the emittance for the whole range of ξ (which is called the projected beam emittance). In order to do this, we divide the trailing beam into 10 slices with a length of $5\,\mu\mathrm{m}$ for each slice (recall that the beam's r.m.s. pulse length is $10\,\mu\mathrm{m}$). In Figure 4.9(a), we show the emittance evolution of each slice. Similarly to the projected emittance, each slice emittance grows rapidly in a short propagation distance (except for the first two slices whose emittance grows slowly) and reaches an equilibrium value larger than the initial value. The slices at front part of the beam have a smaller emittance growth than the projected emittance growth, and the slices at rear part of the beam have a larger growth than that of the projected emittance. The different growth of the emittance for each slice is caused by the different focusing forces (slopes) at different ξ. At the position of ξ which has the largest on-axis slope of the focusing force, the emittance growth is largest. The spot size of each beam slice has a damped oscillation which is similar to the projected beam spot size. Except for the first two slices (which feel the least increase in the focusing force), each slice quickly reaches an equilibrium

value. The equilibrium value of the spot size for each slice varies from each other because the equilibrium emittance of each slice is different.

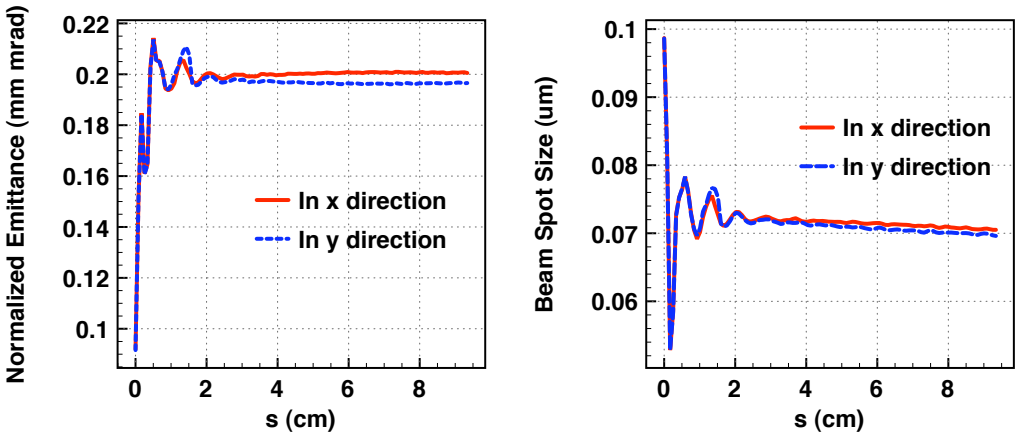

(a) (b)

Figure 4.8: The evolution of the trailing beam's (a) normalized emittance and (b) spot size when the plasma ion motion is included in the simulation.

The above simulation results indicate that when significant plasma ion motion exists the trailing beam (as well as the plasma ion density) will reach an equilibrium state after a period of time much less than the acceleration length. The beam's normalized emittance increases, but can then be preserved at a different equilibrium value. In the example shown above, the trailing beam with an initial emittance of $0.093\,\mathrm{mm}\cdot\mathrm{mrad}$ reaches an equilibrium emittance of $0.2\,\mathrm{mm}\cdot\mathrm{mrad}$, which is a growth of only a factor of 2. It would be useful to quantify the emittance growth with different trailing beam initial conditions. Figure 4.10 shows the simulation results from three cases with different initial emittances of the trailing beam (all other parameters are kept the same). In the case of Fig. 4.10(i), the emittance of the trailing beam increases from $0.5\,\mathrm{mm}\cdot\mathrm{mrad}$ to around $0.61\,\mathrm{mm}\cdot\mathrm{mrad}$, which is only a 20% growth. The spot size of the beam also grows by 50%, from $0.1\,\mu\mathrm{m}$ to $0.15\,\mu\mathrm{m}$. In the case of Fig. 4.10(ii), the emittance of the trailing beam increases from $0.2\,\mathrm{mm}\cdot\mathrm{mrad}$ to around $0.25\,\mathrm{mm}\cdot\mathrm{mrad}$, which is a 25% growth and the spot size of the beam decreases to $0.08\,\mu\mathrm{m}$ from an initial value of $0.1\,\mu\mathrm{m}$.

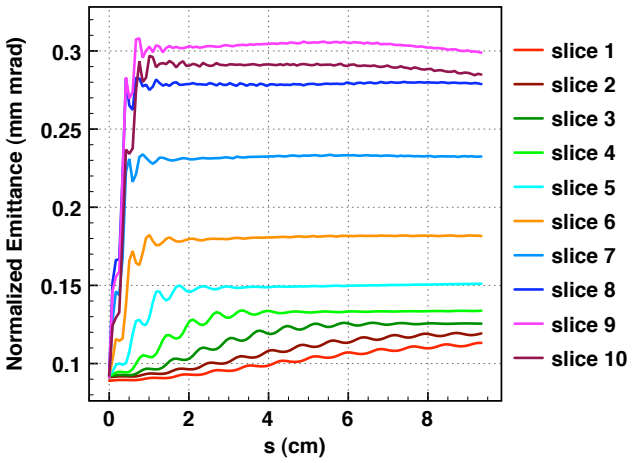

(a)

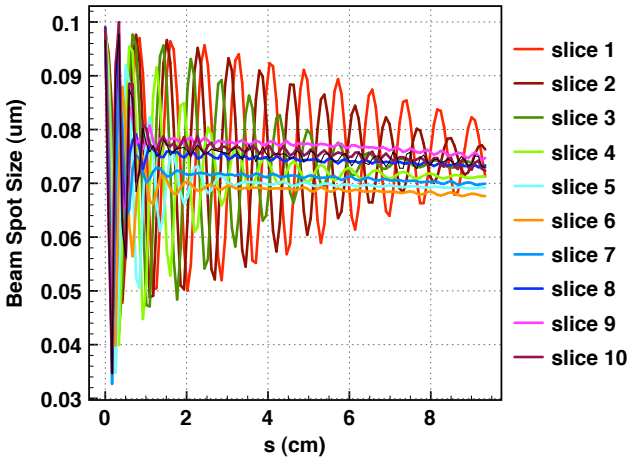

(b)

Figure 4.9: The evolution of the trailing beam's (a) slice normalized emittance and (b) slice spot size in the x direction, when the plasma ion motion is included in the simulation. The trailing beam is divided into 10 slices and each slice is around 5 μm long (recall that the r.m.s. pulse length of the trailing beam is 10 μm). Slice 1 is at the head of the beam and slice 10 is at the tail of the beam.

In the case of Fig. 4.10(iii), the emittance of the trailing beam increases from $0.05\,\mathrm{mm}\cdot\mathrm{mrad}$ to around $0.19\,\mathrm{mm}\cdot\mathrm{mrad}$, which is a growth of a factor of 4, and the spot size of the beam decreases to $0.07\,\mu\mathrm{m}$. Note that this is almost the same equilibrium state as the case shown in Fig. 4.8. Although the emittance still grows in these three cases, it does not grow as much as for the large initial emittance case. This implies that the emittance growth depends on the initial condition of the trailing beam and for certain situations, the growth of the emittance can be small. In these cases we did not start with a matched spot size, and in the later case the spot size was not adequately resolved.

Because the beam eventually reaches an equilibrium state, we also examined what happens if we initialize the trailing beam with those equilibrium parameters. Figure 4.11 shows the simulation results of three cases. In the case of Fig. 4.11(i), the initial emittance of the trailing beam is $0.2\,\mathrm{mm}\cdot\mathrm{mrad}$ and the initial spot size is $0.07\,\mu\mathrm{m}$. This is the equilibrium state for both cases shown in Fig. 4.8 and 4.10(iii). The simulation results show that both the emittance and spot size only increase by $\sim 10\%$. In the case of Fig. 4.11(ii), the initial emittance of the trailing beam is $0.61\,\mathrm{mm}\cdot\mathrm{mrad}$ and the initial spot size is $0.143\,\mu\mathrm{m}$. This is the equilibrium state of the case shown in Fig. 4.10(i). The simulation results also show $\sim 10\%$ growth for both the emittance and spot size. In the case of Fig. 4.11(iii), the initial emittance of the trailing beam is around $0.25\,\mathrm{mm}\cdot\mathrm{mrad}$ and the initial spot size is around $0.08\,\mu\mathrm{m}$. This is the equilibrium state of the case shown in Fig. 4.10(ii). There is also only a $\sim 10\%$ growth of the final emittance and spot size of the trailing beam. Therefore, these results indicate that we might be able to limit the emittance growth to only 10% when using the equilibrium beam parameters obtained from the simulations. Note that in the cases shown in Fig. 4.11, we initialized the trailing beam with the projected emittance and spot size of the equilibrium state and used bi-Gaussian density profiles.

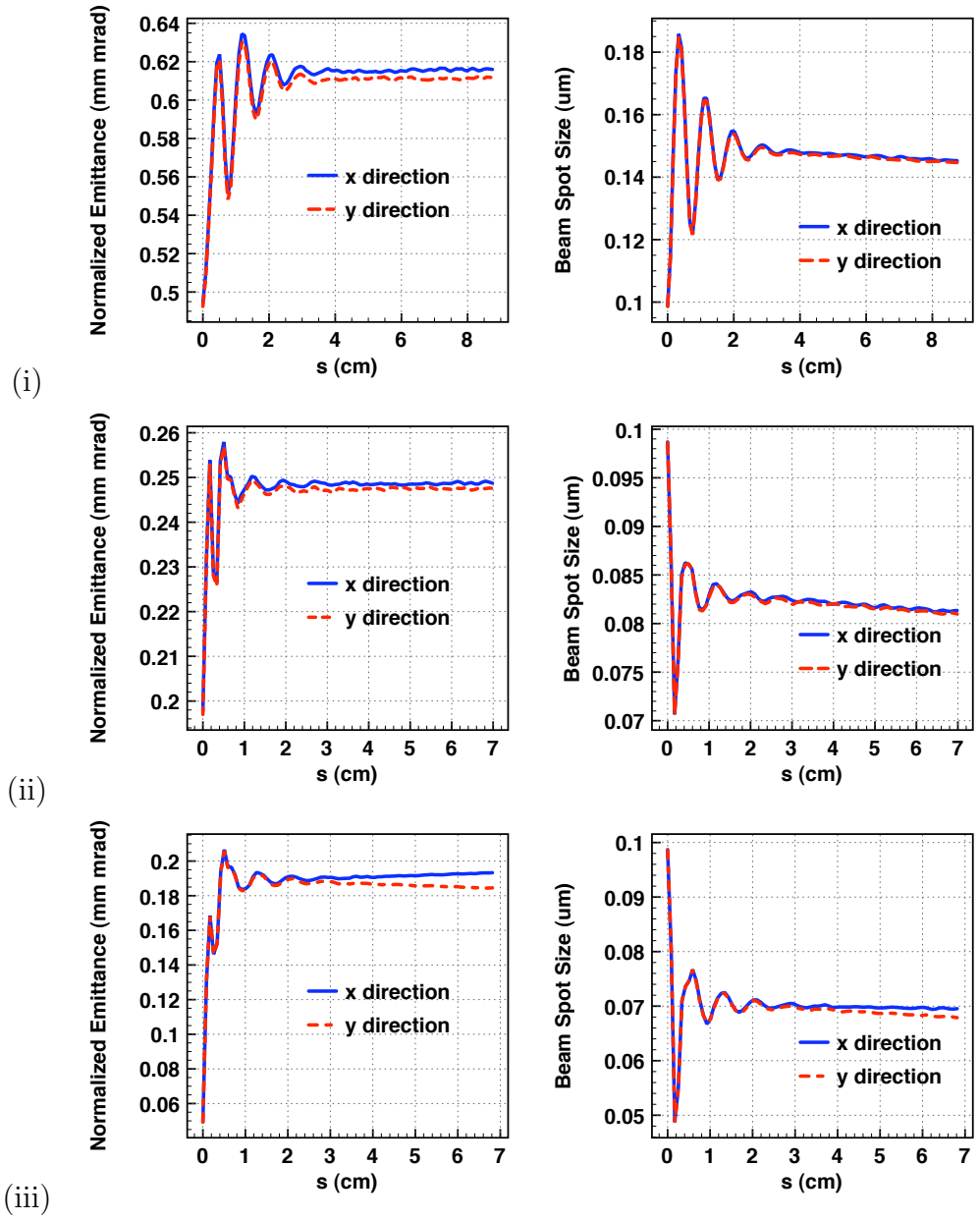

Figure 4.10: The evolution of three different trailing beams' normalized emittance (column (a)) and spot size (column (b)). The initial normalized emittance of the trailing beam is (i) $0.5\,\mathrm{mm}\cdot\mathrm{mrad}$; (ii) $0.2\,\mathrm{mm}\cdot\mathrm{mrad}$; (iii) $0.05\,\mathrm{mm}\cdot\mathrm{mrad}$

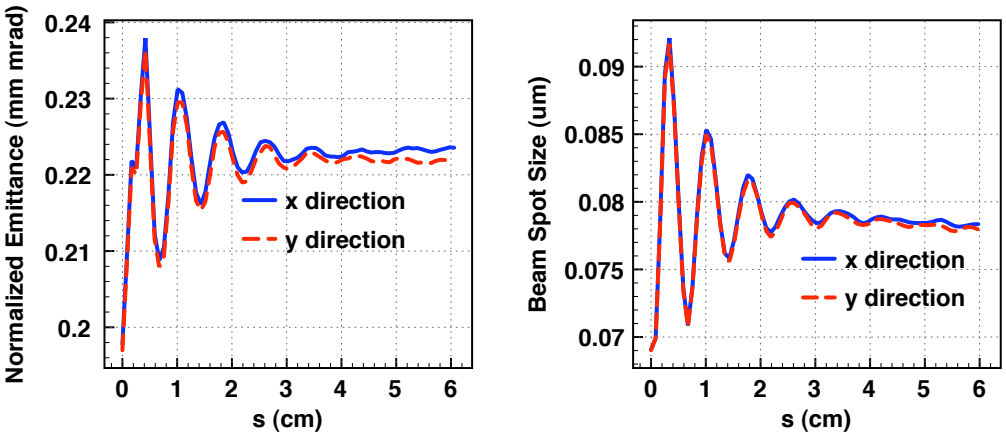

(i)

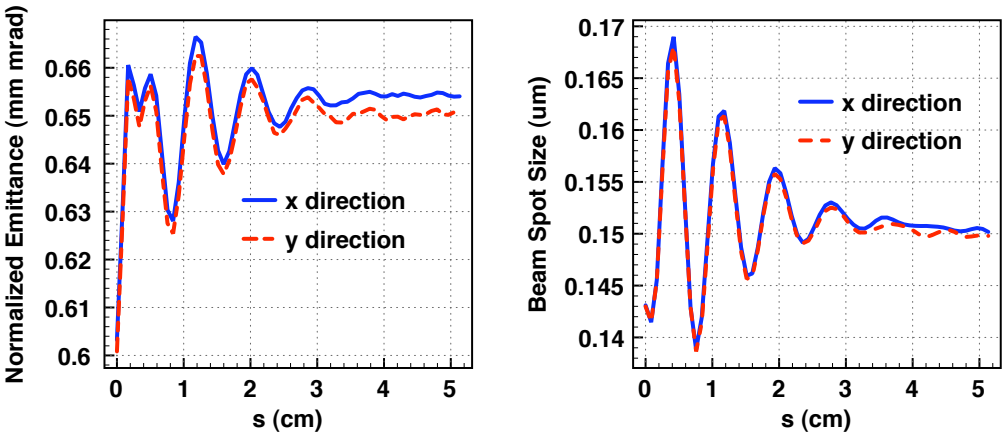

(ii)

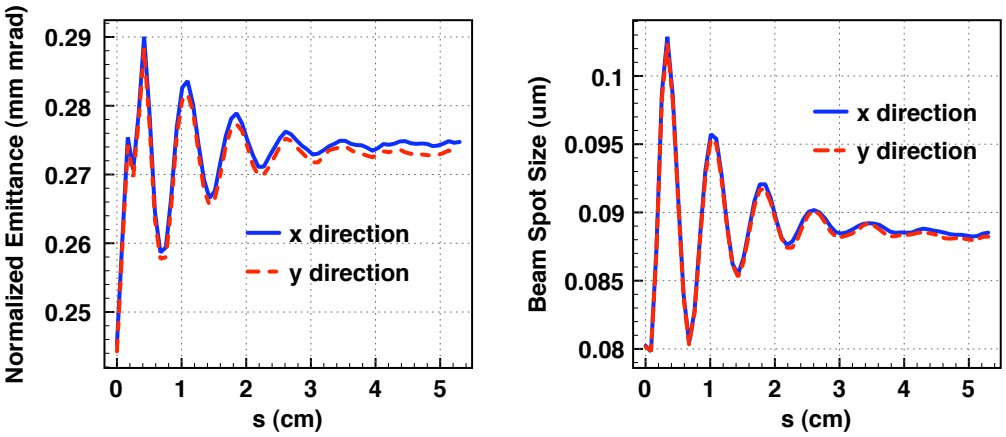

(iii)

(a) (b)

Figure 4.11: The evolution of the three different trailing beams' normalized emittance (column (a)) and spot size (column (b)). The initial normalized emittance of the trailing beam is (i) $0.5\,\mathrm{mm}\cdot\mathrm{mrad}$; (ii) $0.2\,\mathrm{mm}\cdot\mathrm{mrad}$; (iii) $0.05\,\mathrm{mm}\cdot\mathrm{mrad}$

4.5 Summary

In this Chapter, we discussed the role of plasma ion motion in an electron-beam-driven PWFA-LC stage. It is well accepted that when accelerating an electron beam in the blow-out regime with the beam parameter requirements of a future linear collider, the plasma ion motion must be considered because the peak beam density becomes very large compared with the plasma density. Such a high beam density is the result of the very small initial beam emittance and large focusing force in the ion channel, which results in an extremely small matched spot size of the beam. 3D full scale PIC simulations using parameters that resolve the matched spot size of the beam require prohibitive computing time. Furthermore, 2D PIC codes using standard methods have numerical dispersion issues for these parameters. Currently, only QuickPIC can perform the simulation with a proper resolution for this case. We present some preliminary QuickPIC results with different trailing beam parameters. The plasma ion density as well as the trailing beam profile reach an equilibrium state after a relatively short propagation distance in the plasma. For an initially matched beam condition with the normalized emittance of $0.093\,\mathrm{mm}\cdot\mathrm{mrad}$ and the spot size of $0.1\,\mu$m, the plasma ions move drastically within a region $k_p r < 0.1$ (inside the trailing beam). The focusing force of the plasma wake close to the axis is therefore modulated due to the ion motion. The transverse slope of the focusing force becomes steepened near the axis, and the slope varies along the ξ direction. The accelerating field E_z is not affected very much by the ion motion. With different trailing beam initial parameters, the emittance always grows but at different rates. However, the simulations indicate we can limit the emttance growth to a low level $\sim 10\%$, if we initialize the trailing beam with the previously obtained equilibrium beam parameters.

The results are very preliminary and point to areas for future work. The simulation used round beams and only marginally resolved the matched spot size.

We also used singly ionized Li plasma. Therefore, future work should use at least 8 cells across the $\sigma_{matched}$, non-round beams, non-Gaussian profiles (in both transverse and longitudinal directions), and include radiation reaction losses.

CHAPTER 5

Proton-Beam-Driven PWFA

Recently it has been shown that ultra-short and intense proton bunches can generate a nonlinear plasma wave wake field that can be used to accelerate electrons and perhaps positrons [34]. The motivation for considering so called proton-driven PWFA is the existence of very high energy proton beams (such as the 7 TeV LHC beams). The pump depletion length of a 7 TeV proton beam is $L_d = \mathcal{E}_p/eE_-$, where $\mathcal{E}_p$ is the energy of the proton and E_- is the decelerating field in the wake. The energy gain of an electron over this distance could potentially be

$$\mathcal{E}_e = eE_+\frac{\mathcal{E}_p}{eE_-} = \frac{E_+}{E_-}\mathcal{E}_p,$$

where $\mathcal{E}_e$ is the energy of the electron and $\dfrac{E_+}{E_-}$ is called the transformer ratio. Therefore, it could be possible to use a 7 TeV proton (Hadron) beam to generate 7 TeV electron (Lepton) beams in a single stage if the transformer ratio is 1. In the original afterburner concept [79], the idea was to use the output electron beam from the ILC and double its energy (transformer ratio of unity) in a short but single plasma stage. As the construction of the ILC has become doubtful, the idea of a staged PWFA-LC has emerged. The proton-driven PWFA is similar to the original afterburner except that even higher energy hadron beams exist. Note that the energy gain in proton-driven PWFA could be limited from dephasing (not an issue for lepton drivers) to ~ 1 TeV. The dephasing length of a wake field accelerator can be estimated to be

$$L_{dp} = \frac{\lambda_a}{1 - v_b},$$

where λ_a is the length of the acceleration phase of the wake and v_b is the velocity of the drive beam (all quantities are in normalized units and henceforth). In the blowout regime, $\lambda_a \sim R_b$, where R_b is the maximum blowout radius of the wake. This leads to

$$L_{dp} = 2\gamma_b^2 R_b,$$

where $\gamma_b = 1/\sqrt{1 - v_b^2}$. The pump depletion distance can be obtained from

$$E_- L_{pd} = \mathcal{E}_b = m_b \gamma_b.$$

In the relativistic blowout regime [17], the maximum accelerating field is $E_+ = R_b/2$. If we assume the transformer ratio equals to 1, the decelerating field is $E_- = E_+ = R_b/2$ [16, 17]. Therefore

$$L_{pd} = \frac{2 m_b \gamma_b}{R_b}.$$

Comparing L_{dp} and L_{pd}, we can see that

$$\frac{L_{dp}}{L_{pd}} = \frac{R_b^2 \gamma_b}{m_b} \sim \frac{\gamma_b}{m_b},$$

where we assume the maximum blowout radius $R_b \approx 1$. The above equation shows that dephasing is an issue unless $\gamma_b \gg m_b$ or $\mathcal{E}_b \gg 2\,\mathrm{TeV}$ for proton drive beams.

In order to make a clean wakefield, the required pulse length of the proton drive beam should be less than a plasma skin depth [34]. Unfortunately the pulse lengths of the existing high energy proton beams (e.g. at LHC) are around 10 cm, which is much longer than the required pulse length (less than 50 μm) in PWFA. It is unlikely that existing proton beams will be compressed in the foreseeable future. However, such long proton beams self-modulate during the interaction with the plasma. The beam self-modulation in a plasma is almost completely analogous to the laser self-modulation in a plasma, which was widely investigated in the 1990s [5, 7].

Like the laser micro-bunching, the beam self-modulation due to the beam transverse self-focusing will result in a string of micro bunches and drive large

amplitude plasma wake fields. Self-modulation of lasers was studied because sufficiently short pulse lasers did not exist. Importantly, the significant experimental, computational, and theoretical work in the self-modulated LWFA set the stage for the great progress in the 2000s on true LWFA. In this chapter, we will first introduce the short proton beam drive PWFA in section 5.1. In section 5.2, we will describe a theoretical model for the long beam self-modulation in the plasma. In section 5.3, we will show QuickPIC simulation results for proton beam self-modulation in a plasma. Lastly, we will make a summary of the chapter in section 5.4.

5.1 The short proton-beam-driven PWFA

Unlike a negatively charged particle drive beam that can expel the plasma electrons away from it, a positively charged particle drive beam will attract the plasma electrons towards it when the beam propagates in a plasma. When the beam density is much less than the plasma density, the linear fluid model can describe the plasma wake driven by either positively or negatively charged particle beams, and these wakes have no difference in structure. When the beam density becomes larger than the plasma density, the plasma wakes driven by positively and negatively charged beams can be very different. However, a short drive beam of positively charged particles (e.g. positrons and protons) can drive a plasma wake similar to the bubble-like nonlinear plasma wake driven by an intense electron beam (but in a different way). Figure 5.1 shows a nonlinear plasma wake excited by a proton beam together with an electron beam loaded in it. The initial plasma density is $1.0 \times 10^{15}\,\mathrm{cm}^{-3}$. The drive beam contains 1×10^{11} protons and has a Gaussian density profile with a spot size $\sigma_r = 130\,\mu\mathrm{m}$ and a pulse length $\sigma_z = 50\,\mu\mathrm{m}$. The initial energy of the proton beam is 120 GeV. The trailing beam contains 8×10^9 electrons and has a Gaussian density profile with a spot

size $\sigma_r = 30\,\mu$m and a pulse length $\sigma_z = 30\,\mu$m. The initial energy of the trailing beam is 30 MeV. In the Figure 5.1(a), we can see that there is a bubble-like plasma wake excited by the proton drive beam. This is because the proton drive beam is so intense that the Coulomb field around the beam will rapidly pull the plasma electrons towards the axis. This occurs inside the proton beam. After they cross the axis, they expand outward similarly to how an electron beam blows them outwards. This results in a bubble-like plasma wake formed right after the drive beam. The pulse length of the drive beam must therefore be short enough to avoid further interaction with the "blown-out" plasma electrons. Otherwise, the plasma electrons crossing the axis would be attracted back to the drive beam and return to the axis again. This would result in plasma electrons oscillating at a frequency $\omega_{pbeam} = \sqrt{4\pi e^2 n_b/m}$. An electron beam can be properly loaded in the wake so as to flatten the acceleration field (as shown in Fig. 5.1(b)). Figure 5.1(c) shows the energy gain of the trailing electron beam. A 1 GeV/m averaged acceleration gradient is reached in this case. The electrons eventually dephase as discussed earlier. We note that proton-driven wakes differ from electron-driven wakes in that there is a residual density of electrons inside the bubble.

5.2 The linear theory of the long beam self-modulation in a plasmas

Although an intense proton beam with a short pulse length can be used as a drive beam in a two-bunch PWFA, such a proton beam does not exist in current high energy proton accelerators. For example, the proton beam at LHC has a $\sim 10\,$cm long pulse length. Such a high energy beam is very difficult to compress. Recently, driving large amplitude wake fields using the long proton beam self-modulation in the plasma was proposed [84, 85, 86]. As noted earlier, it is a very similar idea to the SM-LWFA (which we introduced in chapter 1). The long

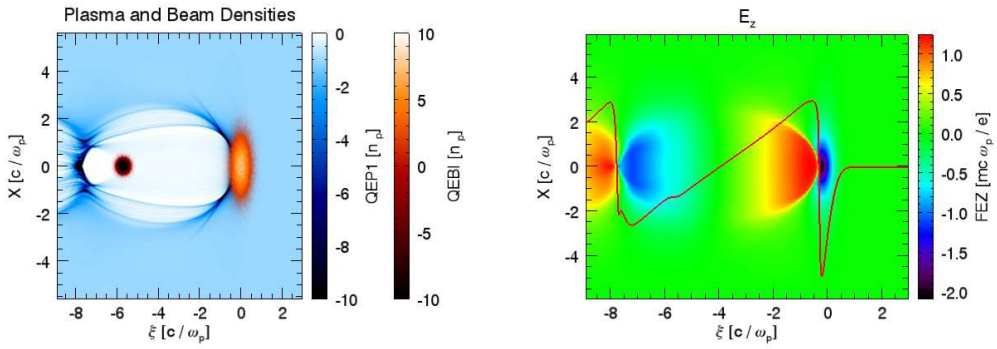

(a) (b)

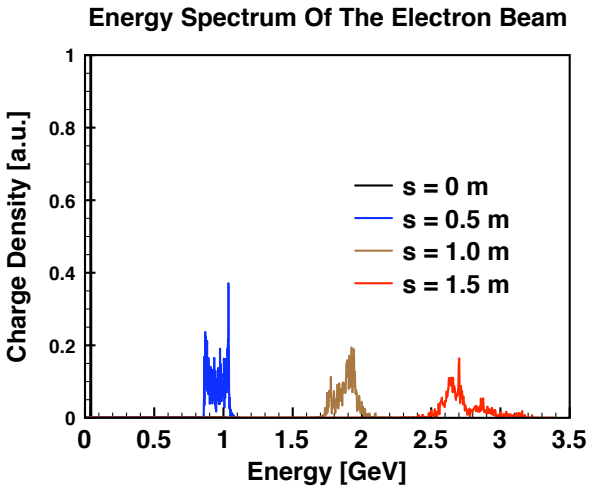

(c)

Figure 5.1: Simulation results for a two-bunch PWFA with an intense short proton drive beam. (a) Plasma density (in blue) and beam densities (in brown); (b) E_z slice plot across the center of the simulation box. The red line is the on-axis line-out of E_z; (c) The energy spectrum of the electron trailing beam at different propagation distance.

beam self-modulation behaves like a convective instability in the lab frame and an absolute instability in the Galilean frame of the coordinate $\xi = ct - z$. For long bunches, $n_b/n_p \ll 1$, so the linear theory of the beam driven plasma wake field can be used to analyze the process. In previous work, either a narrow spot size of the beam[84, 86] or a transverse flat top profile of the beam [85] was assumed to obtain the solution of the plasma wake field driven by the long pulse drive beam. In this section, we present an alternative theoretical description for analyzing the long beam self-modulation under the wide beam limit with a Gaussian transverse beam profile. The wide beam has a normalized beam spot size $k_p\sigma_r > 1$. This is the usual situation when beams propagate in a high density plasma, which has a small plasma skin depth k_p^{-1}.

5.2.1 The linear theory of the plasma wake driven by a particle beam

To obtain the linear theory of the plasma response to a charged particle beam, we start from the continuity equation of the plasma electrons (note that all the quantities are in normalized units),

$$\frac{\partial \rho_e}{\partial t} + \nabla \cdot \vec{J}_e = 0, \tag{5.1}$$

where ρ_e is the electron charge density and J_e is the electron current density. By assuming the plasma response is a small perturbation compared with the initial state, we can linearize this equation and get

$$\frac{\partial \tilde{\rho}_e}{\partial t} - \nabla \cdot \tilde{\vec{v}}_e = 0, \tag{5.2}$$

where $\tilde{\rho}_e = \rho_e - \rho_{e0}$ is the perturbation of the electron charge density (with an uniform initial value of $\rho_{e0} = -1$) and $\tilde{\vec{v}}_e$ is the perturbation of the electron velocity. Both $\tilde{\rho}_e$ and $\tilde{\vec{v}}_e$ are much less than 1. From the linearized equation of motion for the plasma electrons, we have

$$\frac{\partial \tilde{\vec{v}}_e}{\partial t} = -\tilde{\vec{E}}. \tag{5.3}$$

We then take the time derivative of equation (5.2) and substitute equation (5.3) into it to get

$$\frac{\partial^2 \tilde{\rho}_e}{\partial t^2} + \nabla \cdot \tilde{\vec{E}} = 0. \tag{5.4}$$

Gauss's Law gives,

$$\nabla \cdot \tilde{\vec{E}} = \tilde{\rho}_e + \rho_b,$$

where ρ_b is the charge density of the particle beam. Plugging it into equation (5.4), we obtain the equation for the plasma electron density perturbation

$$\frac{\partial^2 \tilde{\rho}_e}{\partial t^2} + \tilde{\rho}_e = -\rho_b. \tag{5.5}$$

Upon applying the quasi-static approximation (as described in chapter 2), equation (5.5) becomes,

$$\frac{\partial^2 \tilde{\rho}_e}{\partial \xi^2} + \tilde{\rho}_e = -\rho_b, \tag{5.6}$$

where $\xi = t - z$. Equation (5.6) is the plasma response to a charged particle beam. The solution to this equation is

$$\tilde{\rho}_e(\xi) = \int_{\xi}^{\infty} d\xi' \rho_b(\xi') \sin(\xi - \xi'). \tag{5.7}$$

Note that $\tilde{\rho}_e$ is also dependent on $\vec{x}_\perp$ and s. We henceforth omit these dependent variables in the above equation for convenience. As described in chapter 3, section 3.1, both the transverse and longitudinal fields of the wake that act on the relativistic beam particles can be calculated from the pseudo potential ψ. The longitudinal field is $F_\parallel = E_z = \partial\psi/\partial\xi$ and the transverse field is $F_\perp = \vec{E}_\perp + \hat{z} \times \vec{B}_\perp = -\nabla_\perp \psi$. Under the quasi-static approximation, the equation for ψ is (which is equation (2.1)) ,

$$\nabla_\perp^2 \psi = -\rho + J_z.$$

Assuming the plasma ions are fixed, the linearized equation for ψ is

$$\nabla_\perp^2 \psi = -\tilde{\rho}_e - \tilde{v}_{ez}. \tag{5.8}$$

Under the quasi-static approximation, the plasma electrons satisfy the conservation law [42],

$$\gamma - p_z = 1 + \psi.$$

By assuming the plasma electron velocity (normalized by the speed of light c) is much less than 1, this equation can also be linearized to $1 - \tilde{v}_{ez} = 1 + \psi$, therefore $\tilde{v}_{ez} = -\psi$. Upon substituting this into the equation (5.8), we get

$$\nabla_\perp^2 \psi - \psi = -\tilde{\rho}_e. \tag{5.9}$$

We can easily write the solution to equation (5.9) using the Green's function,

$$\psi = \frac{1}{2\pi} \int_0^{2\pi} d\theta' \int_0^{\infty} r' dr' \tilde{\rho}_e(\vec{r}') K_0(|\vec{r} - \vec{r}'|), \tag{5.10}$$

where K_0 is the zeroth-order modified Bessel function of the second kind. We can substitute the solution of $\tilde{\rho}_e$ (equation (5.7)) into equation (5.10) to get the solution for ψ directly from the particle beam density,

$$\psi = \frac{1}{2\pi} \int_\xi^{\infty} d\xi' \int_0^{2\pi} d\theta' \int_0^{\infty} r' dr' \rho_b(\vec{r}', \xi') \sin(\xi - \xi') K_0(|\vec{r} - \vec{r}'|). \tag{5.11}$$

The solutions for $F_\parallel$ and $F_\perp$ can then be easily obtained from the solution for ψ. In previous work [84, 85, 86], these solutions are directly used for analyzing the particle beam evolution. However, as shown later, it is not necessary to directly use these solutions. Instead, we keep the following set of equations,

$$\begin{cases} \dfrac{\partial^2 \tilde{\rho}_e}{\partial \xi^2} + \tilde{\rho}_e = -\rho_b \\ \\ \nabla_\perp^2 \psi - \psi = -\tilde{\rho}_e \\ \\ F_\perp = -\nabla_\perp \psi \\ \\ F_\parallel = \dfrac{\partial \psi}{\partial \xi} \end{cases} \tag{5.12}$$

The above set of equations can describe the plasma response and the wake fields acting on the particle beam.

5.2.2 The envelop equation of the particle beam

To describe the evolution of the particle beam, we can use the transverse envelope equation [87, 88]. Here we also assume that the beam particles barely move in the direction of $\xi = t - z$ due to their high energy. Therefore, the beam is mainly evolving laterally under the transverse plasma wake field force. The envelope of the particle beam can be represented by the r.m.s. spot size of the beam,

$$R_x = \sqrt{< x^2 >},$$

where the bracket means taking the average value of the quantity over all of the beam particles and x stands for the transverse coordinate of the beam particle. Note that we assume $< x >= 0$ (ignore the beam hosing). The normalized r.m.s. emittance of beam is defined as

$$\epsilon_{Nx} = \gamma\sqrt{< x^2 >< x'^2 > - < xx' >^2},$$

where $x' = dx/ds = dx/dt \cdot dt/ds \approx v_x$ is the transverse velocity of the beam particle (note that $dt/ds = dt/dz = 1/v_z \approx 1$ for the high energy particle beam), and we assume $< x' >= 0$ (no beam hosing or drift) and all the beam particles have the same energy (γ). This definition for the emittance follows naturally from the following derivation of the spot size equation.

We then look at the second derivative of the beam spot size [88],

$$\begin{aligned} R_x'' &= \sqrt{< x^2 >}'' \\ &= (\frac{< x^2 >'}{2\sqrt{< x^2 >}})' = (\frac{< xx' >}{\sqrt{< x^2 >}})' \\ &= \frac{< xx' >' \sqrt{< x^2 >} - < xx' > \frac{<xx'>}{\sqrt{<x^2>}}}{< x^2 >} \\ &= \frac{< xx'' >}{\sqrt{< x^2 >}} + \frac{< x^2 >< x'^2 > - < xx' >^2}{< x^2 >^{3/2}}, \end{aligned} \tag{5.13}$$

where x'' is the acceleration of the beam particle. The acceleration would be equal to $\frac{q_b F_x}{m_b \gamma}$, where F_x is the transverse focusing field felt by the particle, q_b and m_b are beam particle's charge and rest mass and γ is the Lorentz factor of the beam particle (which is the normalized particle energy). Substituting the expression for the acceleration and normalized emittance into the above equation, we can obtain the envelope equation of the beam,

$$\frac{\partial^2 R_x}{\partial s^2} - \frac{q_b < x F_x >}{m_b \gamma R_x} - \frac{\epsilon_{Nx}^2}{\gamma^2 R_x^3} = 0. \tag{5.14}$$

According to the beam envelope equation, the changing of the beam spot size (the first term in equation (5.14)) is determined by two terms. One term is the force felt by the particle (the second term in equation (5.14)), the other term is the intrinsic expansion from the beam emittance (the third term in equation (5.14)).

5.2.3 Transverse beam self-modulation in PWFA

To look at the beam evolution in PWFA, we should apply the force $F_\perp$ from the plasma wake field in the beam envelop equation. We assume the particle beam has an axisymmetric (round) Gaussian density profile,

$$\rho_b = \frac{q_b \Lambda_b}{R^2} \exp(-\frac{x^2 + y^2}{2R^2}), \tag{5.15}$$

where $R = \sqrt{< x^2 >} = \sqrt{< y^2 >}$ is the transverse spot size of the beam and Λ_b is the beam charge per unit length (which is a constant because the beam particles do not move in the ξ direction). With the axisymmetric assumption, the envelope equation (equation (5.14)) of the beam becomes [87]

$$\frac{\partial^2 R}{\partial s^2} - \frac{q_b < x F_x >}{m_b \gamma R} - \frac{\epsilon_N^2}{\gamma^2 R^3} = 0, \tag{5.16}$$

where $\epsilon_N = \epsilon_{Nx} = \epsilon_{Ny}$ for an axisymmetric beam. Therefore, by adding equations (5.15) and (5.16) into the set of equations (5.12), we obtain a complete set of

equations, which describes the beam envelope evolution in a linear plasma wake,

$$\begin{cases} \rho_b = \dfrac{q_b \Lambda_b}{R^2} \exp(-\dfrac{x^2+y^2}{2R^2}) \\ \dfrac{\partial^2 \tilde{\rho}_e}{\partial \xi^2} + \tilde{\rho}_e = -\rho_b \\ \nabla_\perp^2 \psi - \psi = -\tilde{\rho}_e \\ F_\perp = -\nabla_\perp \psi \\ \dfrac{\partial^2 R}{\partial s^2} - \dfrac{q_b < x F_x >}{m_b \gamma R} - \dfrac{\epsilon_N^2}{\gamma^2 R^3} = 0 \end{cases} \tag{5.17}$$

Note that the equation of the longitudinal wake field is omitted because the beam particle motion in the ξ direction is trivial.

5.2.4 Transverse beam self-modulation for the wide beam limit

The set of equations (5.17) can be simplified if we make further assumptions. We first assume the beam has a spot size much larger than the plasma skin depth (the wide beam limit), i.e., $R >> 1$ (note that it is normalized by the plasma skin depth k_p^{-1}). The wide beam limit is valid if we let the beam propagate in a dense plasma, which has a small skin depth. With the wide beam limit, $\nabla_\perp^2 << 1$, we can drop the first term in the equation for ψ in (5.17) and get

$$\psi = \tilde{\rho}_e.$$

Plugging this into the equation for $\tilde{\rho}_e$ in (5.17), we can obtain

$$\frac{\partial^2 \psi}{\partial \xi^2} + \psi = -\rho_b. \tag{5.18}$$

Note that in general the equation for ψ is,

$$(\frac{\partial^2}{\partial \xi^2} + 1)(\nabla_\perp^2 - 1)\psi = \rho_b$$

Assuming the pulse length of the beam is much larger than 1 (the long beam limit), then ψ will evolve adiabatically along ξ and $\partial_\xi^2 << 1$. We can then drop that term in equation (5.18) and get a simple solution for ψ

$$\psi = -\rho_b.$$

Then we can calculate the term $< xF_x >$ by using $\psi = -\rho_b$ and substituting a Gaussian profile for ρ_b to find,

$$< xF_x >= \frac{\int_{-\infty}^{\infty}\int_{-\infty}^{\infty}\rho_b x\frac{\partial \rho_b}{\partial x}dxdy}{\int_{-\infty}^{\infty}\int_{-\infty}^{\infty}\rho_b dxdy} = -\frac{q_b\Lambda_b}{4R^2}. \tag{5.19}$$

Substituting this into the envelope equation in (5.17), we have

$$\frac{\partial^2 R}{\partial s^2} + \frac{q_b^2\Lambda_b}{4m_b\gamma R^3} - \frac{\epsilon_N^2}{\gamma^2 R^3} = 0. \tag{5.20}$$

We can now define an equilibrium state to perturb about, in which $\partial_s^2 R = 0$,

$$\frac{\partial^2 R}{\partial s^2} = 0 = (\frac{\epsilon_N^2}{\gamma^2} - \frac{q_b^2\Lambda_b}{4m_b\gamma})\frac{1}{R^3}.$$

It implies that $\Lambda_b = \frac{4m_b\epsilon_N^2}{q_b^2\gamma}$ (note that ϵ_N is normalized by k_p^{-1}) is the equilibrium condition for this wide and long particle beam propagating in the linear plasma wake. When $\Lambda_b > \frac{4m_b\epsilon_N^2}{q_b^2\gamma}$, the beam will feel a stronger focusing force from the plasma wake, which will overcome the intrinsic expansion due to the beam emittance, and the beam will be focused to a smaller spot size (i.e., there is self-focusing). When $\Lambda_b < \frac{4m_b\epsilon_N^2}{q_b^2\gamma}$, the beam cannot create a strong plasma response, and a radial expansion due to the beam emittance will dominate, which will result in the beam expanding in the plasma. Note that for the wide beam limit, the equilibrium condition does not depend on the beam spot size, and only Λ_b matters. This is analogous to the critical power of a laser pulse to self-focus in a plasma, which is also a condition unrelated to the spot size (both Λ and laser power are conserved as the beam or laser focuses in the absence of longitudinal slippage [89]).

To study the beam self-modulation, we perturb a beam about the equilibrium state, in which $\Lambda_b = \dfrac{4m_b\epsilon_N^2}{q_b^2\gamma}$. Then we express the beam spot size as $R = R_0 + R_1$, where R_0 is the initial (equilibrium) beam spot size, R_1 is the perturbation and $|R_1/R_0| \ll 1$. Therefore, the beam density can be written as $\rho_b = \rho_{b0} + \rho_{b1}$, where to the lowest order

$$\rho_{b0} = \frac{q_b\Lambda_b}{R_0^2}\exp(-\frac{x^2+y^2}{2R_0^2}) \quad \text{and} \quad \rho_{b1} = \rho_{b0}(\frac{x^2+y^2}{R_0^2} - 2)\frac{R_1}{R_0}. \tag{5.21}$$

The pseudo potential can be written as $\psi = \psi_0 + \psi_1$ and the zeroth order and perturbed parts satisfy

$$\psi_0 = -\rho_{b0} \quad \text{and} \quad \frac{\partial^2\psi_1}{\partial\xi^2} + \psi_1 = -\rho_{b1}. \tag{5.22}$$

Substituting these expressions into the envelope equation (5.17), we find the equation for R_1,

$$\frac{\partial^2 R_1}{\partial s^2} - \frac{q_b < x\partial_x\psi_0 >}{m_b\gamma R_0}\frac{R_1}{R_0} + \frac{q_b < x\partial_x\psi_1 >}{m_b\gamma R_0} + \frac{3\epsilon_N^2}{\gamma^2 R_0^3}\frac{R_1}{R_0} = 0. \tag{5.23}$$

When $\Lambda_b = \dfrac{4m_b\epsilon_N^2}{q_b^2\gamma}$ (the equilibrium condition), then $\dfrac{q_b < x\partial_x\psi_0 >}{m_b\gamma R_0} = \dfrac{\epsilon_N^2}{\gamma^2 R_0^3}$. Therefore,

$$\frac{\partial^2 R_1}{\partial s^2} + \frac{2\epsilon_N^2}{\gamma^2 R_0^3}\frac{R_1}{R_0} = -\frac{q_b < x\partial_x\psi_1 >}{m_b\gamma R_0}. \tag{5.24}$$

We next need an equation for $< x\partial_x\psi_1 >$. We can apply the same operator on this term as is in the equation for ψ_1 in (5.22). This leads to the equation for $< x\partial_x\psi_1 >$, which is

$$\frac{\partial^2 < x\partial_x\psi_1 >}{\partial\xi^2} + < x\partial_x\psi_1 > = - < x\partial_x\rho_{b1} > \tag{5.25}$$

Substituting ρ_{b1} (equation (5.21)) into the above equation and calculating the right hand side gives

$$\frac{\partial^2 < x\partial_x\psi_1 >}{\partial\xi^2} + < x\partial_x\psi_1 > = -\frac{q_b\Lambda_b}{2R_0^2}\frac{R_1}{R_0} = -\frac{2m_b\epsilon_N^2}{q_b\gamma}\frac{R_1}{R_0^3}. \tag{5.26}$$

We define $M_1 = \dfrac{q_b \gamma R_0^3 < x\partial_x \psi_1 >}{2 m_b \epsilon_N^2}$, so that equations (5.24) and (5.26) become two coupled equations

$$\begin{cases} \dfrac{\partial^2 M_1}{\partial \xi^2} + M_1 = -R_1 \\ \\ \dfrac{\partial^2 R_1}{\partial s^2} + \dfrac{2R_1}{\beta^{*2}} = -\dfrac{2M_1}{\beta^{*2}} \end{cases},$$

where $\beta^* = \dfrac{\gamma R_0^2}{\epsilon_N}$. We define $k_s^2 = 2/\beta^{*2}$, and the evolution of the beam spot size can be described by the following two coupled equations

$$\begin{cases} \dfrac{\partial^2 M_1}{\partial \xi^2} + M_1 = -R_1 \\ \\ \dfrac{\partial^2 R_1}{\partial s^2} + k_s^2 R_1 = -k_s^2 M_1 \end{cases} \tag{5.27}$$

The equations in (5.27) essentially describe streaming instabilities in plasmas. They will lead to absolute instabilities in the ξ frame with R_1 increasing in s at each ξ (they are convective in the lab frame). Asymptotic solutions to these equations can be obtained in various limits. In the long pulse limit where $\xi \gg k_s s$, we consider a solution to the equation (5.27) that has the form $M_1 = \tilde{M}_1 e^{-i\xi} + c.c.$ and $R_1 = \tilde{R}_1 e^{-i\xi} + c.c.$, where the amplitude $\tilde{M}_1$ and $\tilde{R}_1$ vary slowly in ξ, i.e., $\partial_\xi \ll 1$. We also assume $\partial_s \gg k_s$ to derive an equation for $\tilde{R}_1$ (and $\tilde{M}_1$)

$$\partial_\xi \partial_s^2 \tilde{R}_1 = \frac{i}{2} k_s^2 \tilde{R}_1. \tag{5.28}$$

We can obtain an asymptotic solution to equation (5.28) for large ξ and s, which is [89]

$$R_1 = \tilde{R}_1 e^{-i\xi} = C \exp\left[\frac{3\sqrt{3}}{4}(k_s s)^{2/3} \xi^{1/3}\right] \cdot \exp\left[-i(\xi - \frac{3}{4}(k_s s)^{2/3} \xi^{1/3})\right], \tag{5.29}$$

where C is the initial value of R_1. We can verify our assumptions $\partial_\xi \ll 1$ and $\partial_s \gg k_s$ by taking the derivatives on $\tilde{R}_1$. It is easy to find that both the assumptions

require $\left(\frac{k_s s}{\xi}\right)^{2/3} \ll 1$, which is satisfied when we use the long pulse limit where $\xi \gg k_s s$.

The solution (5.29) tells that R_1 increases with an e-folding number of

$$N_{\mathrm{e-folding}} = \frac{3\sqrt{3}}{4}\left(\frac{2\epsilon_N^2}{\gamma^2 R_0^4} s^2 \xi\right)^{1/3}$$

, which is also equal to $\frac{3\sqrt{3}}{4}\left(\frac{q_b^2 \Lambda_b}{2 m_b \gamma R_0^4} s^2 \xi\right)^{1/3}$ due to the equilibrium condition $\Lambda_b = \frac{4 m_b \epsilon_N^2}{q_b^2 \gamma}$. To have a large growth rate, we can increase Λ_b or decrease the initial beam spot size. Note that this solution is based on the wide beam limit, which means it is not valid when $R_0 < 1$.

5.3 Simulation result of the long proton beam self-modulation in a plasma

In this section, we present sample QuickPIC simulation results of the self-modulation of a long proton beam in a plasma. The proton beam has a peak density $n_b/n_p = 0.008$, where $n_p = 1.0 \times 10^{16}$ is the initial plasma density. The beam has a transverse Gaussian density profile with a normalized spot size of $k_p \sigma_r = 2.0$. The beam's normalized emittance is $\epsilon_N = 1.78\,\mathrm{mm \cdot mrad}$. In the longitudinal direction, the beam has a flat-top profile with a length of $k_p L_z = 300$ (note that the rapid rise provides a large seed for the instability growth). The initial energy of the proton beam is 120 GeV. These parameters are similar to proton beams at CERN and FNAL.

Figure 5.2 shows snapshots of the proton beam density at different propagation distances. Note that we only show the beam density in the range $-100 < k_p \xi < 0$ in order to make the details of the plots look clear. From Figure 5.2, we can see that the beam self-modulation increases as ξ increases for each s and that the self modulation increases in s for each ξ. At the beginning, the beam density has

a small perturbation (as shown in Figure 5.2(a)). And the envelope of proton beam density oscillates with a wavelength close to the plasma wavelength. After further propagation in the plasma, the transverse density profile of the rear part of the beam becomes more complicated, which means the beam density modulation cannot be considered as a small perturbation on the initial density at this time. When the instability evolves the wavelength of the perturbation also increases as ξ increases (tail of the beam). This can be seen in equation (5.29). As the beam continues to evolve, the part of the beam at large ξ (i.e. the tail of the beam) breaks up completely into separate micro bunches. The beam particles between each micro bunch have been dispersed laterally (completely defocused). When this occurs the bunches evolve into inverse D shapes and then into C shapes.

Figure 5.3 shows the E_z field of the plasma wake in this case. We can clearly see that the beam self-modulation leads to a growth in E_z. At the same slice of ξ, the amplitude of E_z increases when the beam propagates further inside the plasma. The amplitude of E_z also increases along the ξ direction for each value of s. We have also simulated beams with Gaussian profiles along ξ. Such beams also self-modulate but need to propagate longer distances. We are carrying out a detailed simulation study and comparison to theory for future work.

5.4 Summary

In this chapter, we reviewed the proton-beam-driven PWFA concept. A short and intense proton beam can drive a nonlinear plasma wake similar to that driven by an intense electron beam in the blowout regime. It can also accelerate an electron beam to a high energy when it is properly loaded in the plasma wake. When a long proton beam propagates in a plasma, the beam self-modulation instability may occur. A theory was developed for the wide beam limit, which is relevant to possible experiments at CERN or FNAL. The beam spot size evolution can be

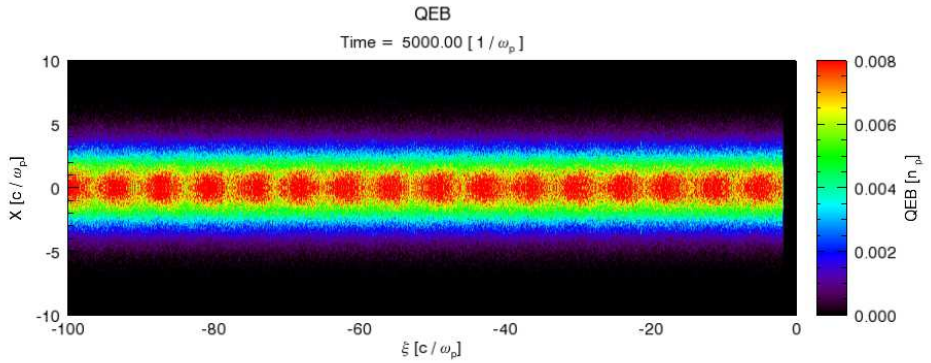

(a) s = 26.6 cm

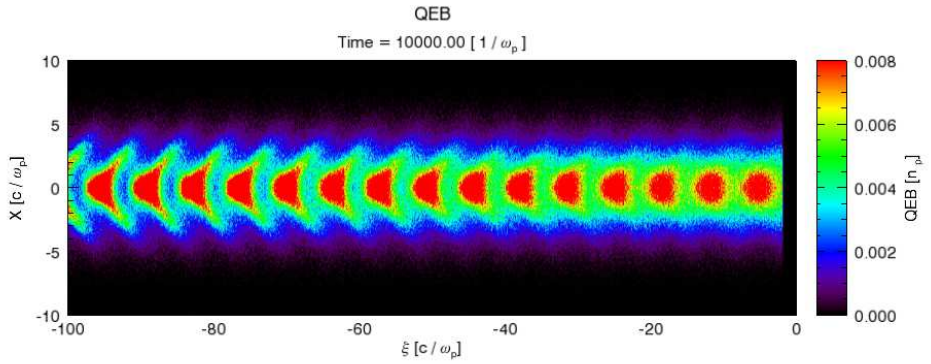

(b) s= 53.22 cm

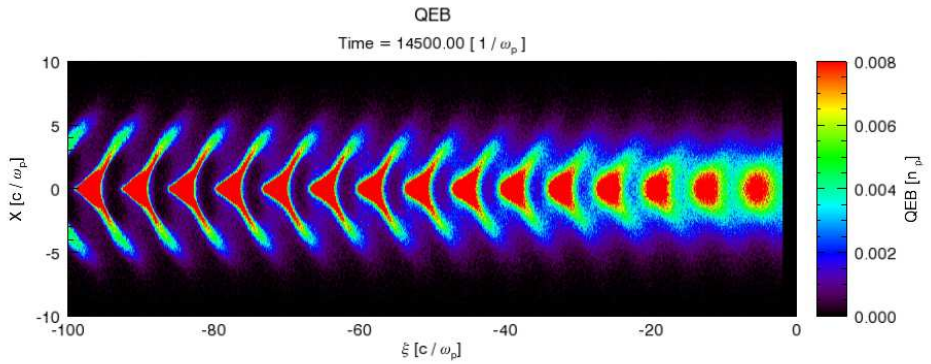

(c) s = 77.16 cm

Figure 5.2: Snapshots of the proton beam self-modulation in a plasma at different propagation distances. The plots are the cross-sections of the beam density in the center of simulation box (where $Y = 0.$). The beam travels to the right of the simulation box.

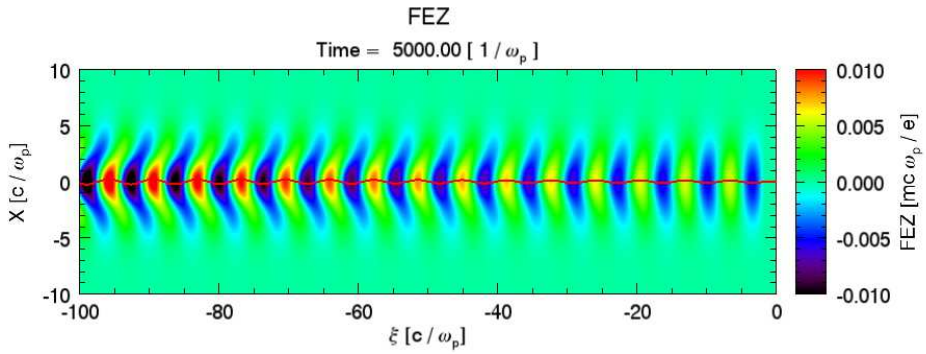

(a) s = 26.6 cm

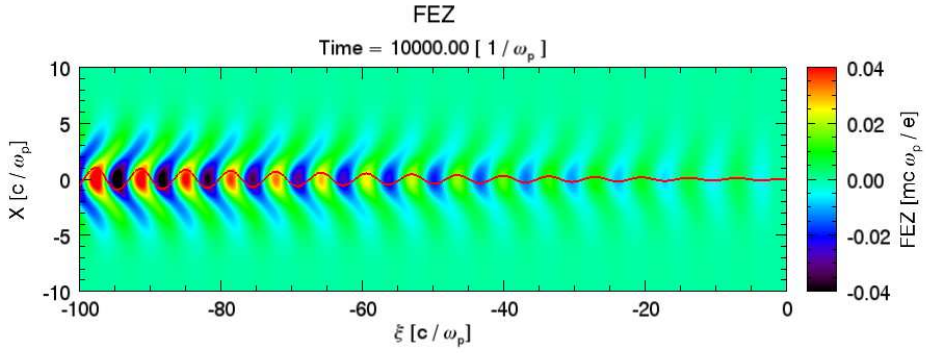

(b) s= 53.22 cm

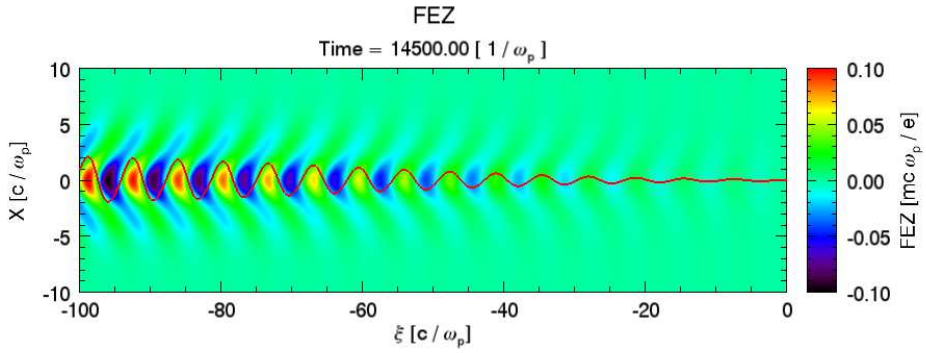

(c) s = 77.16 cm

Figure 5.3: Snapshots of the longitudinal electric field E_z in the proton-beam–driven plasma wake through beam self-modulation. The plots are the cross-sections of E_z in the center of simulation box (where $Y = 0$.)The red line in each plot is the on-axis line-out of E_z.

obtained by solving two coupled equations and the analysis is valid for Gaussian beams. These equations are analogous to the streaming instabilities and the laser self-modulations in a plasma. Asymptotic expressions for growth in ξ and s are given for the long bunch limit. Preliminary QuickPIC simulation results of a long proton beam self-modulation are also presented. Eventually a nonlinear state is reached in which the beam completely breaks apart into micro bunches. This results in a large amplitude plasma wake at the rear part of the beam. The simulation work was preliminary. Areas for future work include checking the validity of the linear theory when the beam is initialized with a non-equilibrium state, comparing OSIRIS (full PIC) simulation result with the QuickPIC results for the self-modulation of the long proton beam, and simulation studies using different proton beam parameters and density profiles.

CHAPTER 6

Conclusion

In this dissertation we have investigated issues related to plasma wakefield acceleration (PWFA) using quasi-static particle-in-cell simulations. We have studied parameters of relevance to existing experiments at the new FACET facility at SLAC. These include experiments on how to optimize the absolute value of the accelerating field and on how to demonstrate that a second bunch can be loaded into and accelerated in the wakefield from a first bunch. We also investigated parameters of relevance to future experiments, including those of relevance to a future linear collider based on PWFA and on using proton beams at LHC or FANL to drive wakefields.

The simulations were carried out using the code QuickPIC which is the only fully three-dimensional quasi-static PIC code in existence. However, improvements were needed in QuickPIC to enable some of the simulations. In Chapter 2 we described a new algorithm for solving the electromagnetic fields in QuickPIC, and we call the new code QuickPIC 2.0. The new algorithm uses equations for the electromagnetic fields that are gauge invariant, instead of the equations for the scalar and vector potentials for the Lorentz gauge (which are used in QuickPIC 1.0). We also introduced a new deposition scheme for calculating the time (ξ) derivative of the plasma current density, which can reduce the communication in the parallel computation. By comparing the simulation results for different beam driven PWFA cases, we found that QuickPIC 2.0 was in excellent agreement with the full PIC code OSIRIS after only 1 iteration for the most cases, while Quick-

PIC 1.0 typically needs at least 4 iterations (and in some cases 8 iterations) to reach the same accuracy. For a typical nonlinear PWFA simulation, QuickPIC 2.0 is 5 to 8.5 times faster than QuickPIC 1.0. The speedup depends on the number of particles per cell used in the simulation. New modules were implemented in QuickPIC 2.0, including the multiple field ionization, an improved beam and plasma initialization, and diagnostics.

In the future, we will continue to put effort in developing QuickPIC 2.0. One area of the work is to compare different algorithms which use conservation laws differently for the motion of plasma particles and see how well the constant of the motion is well maintained for each case. We will also merge the laser solver into QuickPIC 2.0. In addition, developing a plasma particle trapping module, implementing adaptive 2D and 3D time steps, experimenting with load balancing in the 2D part of the code, porting the code to a hybrid one (MPI + OpenMP) together with GPU acceleration and experimenting a $\vec{k}_\perp$ dependent coefficient in the iterative equation (2.20) will all be the areas for the future work.

For the electron beam driven PWFA in the blow-out regime, we studied the decelerating field in the plasma wake through QuickPIC simulations. With Gaussian density profiles, the electron drive beam will feel the maximum decelerating field approximately equal to $\Lambda/\sqrt{e}k_p\sigma_z$ in a range of $k_p\sigma_z$ centered near 3. The optimum plasma density for achieving the largest accelerating field was also analyzed. For the relativistic blowout regime ($\Lambda \geq 1$), the optimum plasma density is $n_o = n_{b0}$, where n_{b0} is the peak beam density, as long as $1 \geq \sigma_r/\sigma_z \geq 1$.

We performed QuickPIC simulations for two-bunch PWFA with possible parameters at FACET. With a pre-formed plasma, a trailing beam with 30 GeV energy gain as well as a 3% energy spread was observed through a long plasma cell that is over two meters long. However, when using the field-ionized plasma, the ionization-induce beam head erosion was found to significantly affect the drive beam's ability to ionize the neutral gas and excite the plasma wake and there-

fore limit the trailing beam's energy gain. We found that the head erosion can be mitigated by applying a combination of lower ionization threshold gas and a laser-produced plasma filament in front of the drive beam, which provides important guidance for the upcoming two-bunch PWFA experiments on the FACET facility.

In the PWFA-LC conceptual design, the two-bunch PWFA is well accepted for accelerating an electron beam. However, the plasma ion motion must be included because the peak beam density is so high that the self-field of the beam will pull the massive plasma ions inward during beam's transit time. QuickPIC 2.0 is currently the only 3D PIC code that can perform the simulation for a PWFA-LC stage with proper resolution. Preliminary simulation results were presented using different trailing beam parameters but the same drive beam (which is assumed not to evolve). From the simulation results, we found that the trailing beam profile reached an equilibrium state after a short propagation distance in the plasma. The same was true for the plasma ion density. Although the accelerating field of the plasma wake does not change very much by the plasma ion motion, the focusing force is significantly modulated by the plasma ions. The trailing beam's emittance always increases due to the nonlinear focusing force. However, with different initial parameters, the trailing beam's emittance grows at different rates. The simulation results indicated that the emittance growth rate could be limited to $\sim 10\%$ when the trailing beam was initialized with the previously obtained equilibrium beam parameters.

In the future, we will use a finer resolution (at least 8 cells across the $\sigma_{matched}$) and check the convergence of the results in the future. The emittance growth with different trailing beam initial conditions, including non-round profiles (i.e. asymmetric profiles) and non-Gaussian profiles (in both transverse and longitudinal directions) will be investigated. We will also consider the radiation reaction losses of the trailing beam in the future.

Besides the electron beam driven PWFA, we showed that a short and intense

proton beam could also drive a bubble-like nonlinear plasma wake for accelerating an electron beam. However, the existing high energy proton beams all have a very long pulse length. Therefore, the long beam driven PWFA was studied. We provided a theory to analyze the long beam self-modulation in the plasma by assuming the beam spot size is much larger than the plasma skin depth. Two coupled equations were obtained, which indicated that a small perturbation of the beam envelope would grow as a convective instability. The asymptotic growth rate was given under the strong coupling (or long pulse) assumption. We presented QuickPIC simulation results for a long proton beam self-modulation in a plasma. The proton beam breaks up into micro bunches and drives a large amplitude wake in the plasma.

Checking the validity of the linear perturbation theory of the beam self-modulation under non-equilibrium initial conditions will be an area for future work. Other work will include the comparison between OSIRIS and QuickPIC simulation results for the long beam case and simulation study using different proton beam parameters. The coupling between self-modulation and hosing instability will be investigated as well as an investigation on how the proton beam's energy will be modulated and on how self-injected and externally injected electrons will be accelerated. We will also examine how to optimize the energy of a trailing electron beam in the plasma wake driven by a ultra-short proton beam.

References

[1] http://home.web.cern.ch/about/accelerators/large-hadron-collider.

[2] http://www.linearcollider.org/.

[3] T. Tajima and J. M. Dawson. Laser electron accelerator. *Phys. Rev. Lett.*, 43(4):267, 1979.

[4] P. Chen et al. Acceleration of electrons by the interaction of a bunched electron beam with a plasma. *Phys. Rev. Lett.*, 54:693, 1985.

[5] A. Modena et al. *Nature*, 337:606, 1995.

[6] M. Everett et al. *Nature*, 368:527, 1994.

[7] K. Nakajima et al. *Phys. Rev. Lett.*, 74:4428, 1995.

[8] H. Nakanishi et al. *Nucl. Instrum. Meth.*, A328:596, 1993.

[9] D. Strickland and G. Mourou. Compression of amplified chirped optical pulses. *Opt. Commun.*, 56:219, 1985.

[10] M. Ferray, L. A. Lompre, 0. Gobert, A. L. Huillier, G. Mainfray, C. Manus, and A. Sanchez. Multiterawatt picosecond nd:glass laser system at 1053 nm. *Opt. Commun.*, 75:278, 1990.

[11] F .G. Patterson, R. Gonzales, and M. D. Perry. Compact 10-tw, 800-fs. nd:glass laser. *Opt. Lett.*, 16:1107, 1991.

[12] C. G. R. Geddes et al. High-quality electron beams from a laser wakefield accelerator using plasma-channel guiding. *Nature*, 431:538, 2004.

[13] J. Faure et al. A laser-plasma accelerator producing monoenergetic eletron beams. *Nature*, 431:541, 2004.

[14] S. P. D. Mangles et al. Monoenergetic beams of relativistic electrons from intense lasercplasma interactions. *Nature*, 431:535, 2006.

[15] C. B. Schroeder et al. *AIP Conf. Proc.*, 1086:637, 2009.

[16] W. Lu et al. *Phys. Rev. Lett.*, 96:165002, 2006.

[17] W. Lu et al. *Phys. Plasmas*, 13:056709, 2006.

[18] A. Pak et al. *Phys. Rev. Lett.*, 104:025003, 2010.

[19] C. McGuffey et al. *Phys. Rev. Lett.*, 104:025004, 2010.

[20] C. E. Clayton et al. *Phys. Rev. Lett.*, 105:105003, 2010.

[21] M. J. Hogan et al. *Phys. Plasmas*, 7:2241, 2000.

[22] P. Muggli et al. *Phys. Rev. Spec. Top. Acc. & Beam*, 4:091301, 2001.

[23] C. E. Clayton et al. *Phys. Rev. Lett.*, 88:154801, 2002.

[24] M. Hogan et al. *Phys. Rev. Lett.*, 90:205002, 2003.

[25] B. E. Blue et al. *Phys. Rev. Lett.*, 90:214801, 2003.

[26] P. Muggli et al. *Phys. Rev. Lett.*, 93:014802, 2004.

[27] M. Hogan et al. *Phys. Rev. Lett.*, 95:054802, 2005.

[28] I. Blumenfeld et al. *Nature*, 445:741, 2007.

[29] http://www.lbl.gov/community/bella/.

[30] http://www.extreme-light-infrastructure.eu/.

[31] M. J. Hogan et al. *New J. Phys.*, 12:055030, 2010.

[32] G. Xia et al. *AIP Conf. Proc.*, 1299:510, 2010.

[33] J. C. T. Thangaraj et al. *AIP Conf. Proc.*, 1507:644, 2012.

[34] A. Caldwell et al. Proton-driven plasma-wakeeld acceleration. *Nature Phys.*, 5:363, 2010.

[35] J. M. Dawson. Particle simulation of plasmas. *Rev. Mod. Phys*, 55:403, 1983.

[36] Charles K. Birdsall and A. Bruce Langdon. *Plasma Physics Via Computer Simulation*. McGraw-Hill, New York, 1985.

[37] P.C. Liewer and V.K. Decyk. *J. Comp. Phys.*, 85:302, 1989.

[38] V. K. Decyk. Upic: A framework for massively parallel particle-in-cell codes. *Comput. Phys. Commun.*, 177:95, 2007.

[39] R. A. Fonseca et al. Osiris: A three-dimensional, fully relativistic particle in cell code for modeling plasma based accelerators. *Lect. Notes Comput. Sci.*, 2331:342, 2002.

[40] W. B. Mori. Full-scale numerical experiment to test a future plasma-based accelerator. Proposal submitted to NSF, 1992.

[41] S. F. Martins et al. *Nature Phys.*, 6:311, 2010.

[42] P. Mora and T. M. Antonsen. Kinetic modeling of intense, short laser pulses propagating in tenuous plasmas. *Phys. Plasmas*, 4:217, 1997.

[43] C. Huang et al. *J. Comp. Phys.*, 217:658, 2006.

[44] D. E. Gordon, W. B. Mori, and T. M. Antonsen Jr. *IEEE Trans. Plasma Sci.*, 28:1135, 2000.

[45] B. Feng et al. Enhancing parallel quasi-static particle-in-cell simulations with a pipelining algorithm. *J. Comp. Phys.*, 228:5340, 2009.

[46] K. V. Lotov. Fine wakefield structure in the blowout regime of plasma wakefield accelerators. *Phys. Rev. ST Accel. Beams*, 6:061301, 2003.

[47] D. H. Whittum. Transverse two-stream instability of a beam with a bennet profile. *Phys. Plasmas*, 4:1154, 1997.

[48] C. Huang et al. Quickpic: A highly efficient particle-in-cell code for modeling wakeeld acceleration in plasmas. *J. Comp. Phys.*, 217:658, 2006.

[49] W. Lu et al. Nonlinear theory for relativistic plasma wakeelds in the blowout regime. *Phys. Rev. Lett.*, 96:165002, 2006.

[50] C. Huang et al. Hosing instability in the blow-out regime for plasma-wakeeld acceleration. *Phys. Rev. Lett.*, 99:255001, 2007.

[51] I. Blumenfeld et al. Energy doubling of 42 gev electrons in a metre-scale plasma wakefield accelerator. *Nature*, 445:741, 2007.

[52] M. J. Hogan et al. Plasma wakefield acceleration experiments at facet. *New J. Phys.*, 12:055030, 2010.

[53] W. An et al. Simulations of two-bunch plasma wakeeld accelerator experiments at facet. In *Advanced Accelerator Concepts, 14th Workshop, AIP Conf. Proc.*, page 472, AIP, NY, 2010.

[54] V. K. Decyk. Darwin particle-in-cell models. *The 18th Intl. School Symposium for Space Simulations, Kauai, Hawaii, USA*, 2007.

[55] D. Schriver et al. Generation of whistler mode emissions in the inner magnetosphere: An event study. *J. of Geophysical Res.*, 115:A00F17, 2010.

[56] M. Zhou et al. Modeling self-ionized plasma wakefield acceleration for afterburner parameters using quickpic. In *Proceedings of the 2005 PAC Conference, Knoxville, TN*, page 2905, AIP, NY, 2005.

[57] Ian Blumenfeld et al. Energy doubling of 42 gev electrons in a metre-scale plasma wakefield accelerator. *Nature*, 445:741, 2007.

[58] M. V. Ammosov et al. Tunnel ionization of complex atoms and of atomic ionis in an alternating electromagnetic eld. *Sov. Phys. JETP*, 64:1191, 1986.

[59] D. L. Bruhwiler et al. Particle-in-cell simulations of tunneling ionization effects in plasma-based accelerators. *Phys. Plasmas*, 10:2022, 2003.

[60] D. Bauer and P. Mulser. Exact eld ionization rates in the barrier- suppression regime from numerical time-dependent schrodinger-equation calculations. *Phys. Rev. A*, 59:569, 1999.

[61] M. Borland. Elegant: A flexible sdds-compliant code for accelerator simulation.

[62] M. Zhou. *Accelerating Ultra-Short Electron Positron Bunches in Field Ionization Produced Plasmas*. Ph.D. thesis, University of California Los Angeles, 2008.

[63] The HDF Group. Hierarchical data format version 5. 2000-2010.

[64] J. B. Rosenzweig et al. *Phys. Rev. A*, 44:R6189, 1991.

[65] P. Muggli et al. *IEEE Trans. Plasma Sci.*, 27:791799, 1999.

[66] C. Joshi et al. *Phys. Plasmas*, 9:1845, 2002.

[67] M. Tzoufras et al. *Phys. Rev. Lett.*, 101:145002, 2008.

[68] W. K. H. Panofsky and W. A. Wenzel. *RSI*, 27:967, 1956.

[69] W. Lu et al. High transformer ratio plasma wakefield acceleration in the blowout regime. (in preparation), 2013.

[70] W. Lu et al. *Phys. Plasmas*, 12:063101, 2005.

[71] W. An et al. *J. Comp. Phys.*, 250:165, 2013.

[72] D. L. Bruhwiler et al. *Phys. Plasmas*, 10:2022, 2003.

[73] C. O'Connell et al. *Phys. Rev. ST Accel. Beams*, 9:101301, 2006.

[74] N. Vafaei-Najafabadi et al. Evidence for beam loading by distributed injection of electrons in a plasma wakefield accelerator. (submitted), 2013.

[75] C. Joshi et al. *Phys. Plasmas*, 9:1845, 2002.

[76] J. B. Rosenzweig et al. *Phys. Rev. Lett.*, 95:195002, 2005.

[77] A. Seryi et al. A concept of plasma wake field acceleration linear collider (pwfa-lc). In *Proceedings of the 2009 PAC Conference, Vancouver, BC, Canada*, AIP, NY, 2009.

[78] E. Adli et al. *arXiv:1308.1145*, 2013.

[79] S. Lee et al. *Phys. Rev. ST Accel. Beams*, 5:011001, 2002.

[80] X. Wang et al. *Phys. Rev. Lett.*, 101:124801, 2008.

[81] C. Huang et al. Simulations of 25 gev pwfa sections: Path towards a pwfa linear collider. In *Proceedings of the 2009 PAC Conference, Vancouver, BC, Canada*, AIP, NY, 2009.

[82] R. Gholizadeh et al. *Phys. Rev. Lett.*, 104:155001, 2010.

[83] R. Gholizadeh et al. *AIP Conf. Proc.*, 877:504, 2006.

[84] N. Kumar and A. Pukhov. *Phys. Rev. Lett.*, 104:255003, 2010.

[85] C. B. Schroeder et al. *Phys. Rev. Lett.*, 107:145002, 2011.

[86] A. Pukhov et al. *Phys. Rev. Lett.*, 107:145003, 2011.

[87] M. Reiser. *Theory and Design of Charged Particle Beams*. Wiley-VCH, Weinheim, 2nd edition, 2008.

[88] Private communication with Xinlu Xu.

[89] W. Mori. *IEEE J. Quantum Electron.*, 33:1942, 1997.